Borehole Wave Propagation in Isotropic and Anisotropic Media: Three-Dimensional Finite Difference Approach

by

Ningya Cheng

M.S., Beijing University (1985)
B.S., Beijing University (1983)

Submitted to the Department of Earth, Atmospheric, and Planetary Sciences
in partial fulfillment of the requirements for the degree of

Doctor of Philosophy

at the

MASSACHUSETTS INSTITUTE OF TECHNOLOGY

February 1994

Signature of Author .....
Department of Earth, Atmospheric, and Planetary Sciences
February, 1994

Certified by .....
M. Nafi Toksöz
Professor of Geophysics
Thesis Advisor

Certified by .....
Chuen H. Cheng
Principal Research Scientist
Thesis Co-advisor

Accepted by .....
Thomas H. Jordan
Chairman
Department of Earth, Atmospheric, and Planetary Sciences

Borehole Wave Propagation in Isotropic and Anisotropic Media: Three-Dimensional Finite Difference Approach

by

Ningya Cheng

Submitted to the Department of Earth, Atmospheric, and Planetary Sciences
on February, 1994, in partial fulfillment of the
requirements for the degree of
Doctor of Philosophy

Abstract

In this thesis we develop a three-dimensional finite difference method to simulate wave propagation in an isotropic as well as an anisotropic medium. The wave equation is formulated into the first-order hyperbolic equations by using velocity and stress. They are discretized on a staggered grid. The three-dimensional finite difference time domain scheme is second-order accurate in time and fourth-order accurate in space. The grid dispersion and anisotropy are analyzed and the stable condition of the scheme is obtained. Higdon's absorbing boundary condition is discussed and generalized to the anisotropic medium. The scheme provides realistic 3-D wave propagation simulation by the use of a parallel computer.

The finite difference method is first tested in homogeneous media. The finite difference results agree excellently with the analytic solutions of a point explosion source in the acoustic medium and a point force source in elastic and transversely isotropic media. The finite difference method accurately models not only the far field P and S waves, but also the near field term. The method is then tested in a fluid-filled borehole surrounded by a homogeneous elastic formation. The finite difference results are in good agreement with the discrete wavenumber solutions for both monopole and dipole sources in the hard as well as the soft formations. These tests also show the good performance of Higdon's absorbing boundary condition in isotropic and anisotropic media. It not only works for the body waves but also for the guided waves.

The 3-D finite difference time domain method is applied to fluid-filled borehole wave propagation problems in isotropic and anisotropic formations. The effects of the off-centered sources, the elliptic borehole, and the tilted layer on acoustic logs are investigated for the isotropic formation. The finite difference synthetics are compared

with ultrasonic laboratory measurements in a scaled borehole in an orthorhombic phenolite solid. Both monopole and dipole logs agree well. In the anisotropic formation the different borehole orientations are considered for monopole and dipole logs. Due to shear wave anisotropy, there are shear-pseudo-Rayleigh wave arrivals on the monopole log between the P and Stoneley waves in the phenolite formation. Anisotropy can also cause shear wave splitting on the dipole log.

Field data sets collected by an array monopole acoustic logging tool and a shear wave logging tool were processed and interpreted. The P- and S-wave velocities of the formation are determined by threshold detection with cross-correlation correction from the full waveform and the shear wave log, respectively. The extended Prony's method is used to estimate the borehole Stoneley wave phase velocity and attenuation as a function of frequency. The formation between the depths of 2950 and 3150 ft can be described as an isotropic elastic medium. The inverted V_s from the Stoneley wave phase velocity is in excellent agreement with the shear wave log results. The formation between the depths of 3715 and and 3780 ft is a porous, permeable and anisotropic medium. The shear wave velocity anisotropy is about 10% to 20%, and the symmetry axis is perpendicular to the borehole axis. The disagreement between estimated permeabilities from low frequency Stoneley wave velocity and attenuation data are in good agreement with the core measurements. Also, it is shown that the formation permeability is not the primary cause of the discrepancy between the shear wave velocity inverted from the Stoneley wave and measured by the shear wave logs. The 3-D finite difference synthetics in the anisotropic formation confirm that the discrepancy can be explained as shear wave anisotropy.

Thesis Advisor: M. Nafi Toksöz
Title: Professor of Geophysics

Thesis Co-advisor: Chuen H. Cheng
Title: Principal Research Scientist

Acknowledgments

First I would like to thank my advisor Nafi Toksöz for his guidance during my MIT years. I benefited greatly from his insight into a wide range of problems and his philosophy of approaching and solving the geophysical problems. I would also like to thank my thesis co-advisor Arthur Cheng for his advice, help, and for sharing his knowledge of acoustic logging and wave propagation.

I would like to thank the staff, past and present students who create a very stimulating research environment at ERL. They are Roger Turpening, Bata Mandal, Anton Dainty, Bill Rodi, Jung-Mo Lee, Matthijs Haartsen, Matthias Imhof, Joe Matarese, Delaine Thompson, Rick Bennett, Karl Ellefsen, Jeff Meredith, Rick Gibson, Bob Cicerone, Ed Reiter, Arcangelo Sena and many others. I would like to single out Ted Charrette to thank for his help to parallel my code on nCUBE. It would not have been possible to complete this thesis without the nCUBE. This thesis is benefited from the discussions with Ralph Stephen from Woods Hole Oceanographic Institution about finite difference method to simulate wave propagation. I also would like to thank Ken Tubman of ARCO Oil and Gas Co. for the use of the acoustic logging data. I appreciate the help of Sara Brydges, Liz Henderson, Sue Turbak, Naida Buckingham, Jane Maloof and Al Taylor for letting ERL running smoothly, specially thanks Naida for her help to improve English writing of this thesis.

Many thanks go to the fellow Chinese at ERL, Zhenya Zhu, Xiaoming Tang, Xiaomin Zhou, Chengbin Peng, Wenjie Dong, Yinping Li and Jie Zhang, for their friendship and help. I really enjoyed the Chinese lunch table: food, China news, politics, sports, jokes...

Finally, I would like to thank my Mom and Dad for their endless support and encouragement, especially at the final stage of this thesis when they moved their support from China to America.

This research was supported by the Borehole Acoustics and Logging Consortium at M.I.T. and by the ERL/nCUBE Geophysical Center for Parallel Processing.

Contents

Chapter 1

Introduction

1.1 Background

Elastic wave propagation provides one of the important means to probe the Earth's structure. Data collected from different frequency ranges are used to investigate structures on different scales. For example, free oscillations is for studying the global structures, and seismic body and surface waves for studying regional structures. The acoustic downhole logging data are collected from wells drilled in the Earth's crust. The purposes of the log are to evaluate the properties of the rocks around the borehole at a resolution of the order of a half meter. The compressional and the shear wave velocities measured from the acoustic log are used for the modeling and the interpretation of seismic reflections and for vertical seismic profiling (VSP) data. Understanding the wave propagation around a fluid-filled borehole is essential to acoustic log data processing and interpretation.

Early investigations of fluid-filled borehole wave propagation determined the borehole guided wave dispersion curves, which gives physical insight into the behavior of the borehole guided waves (Biot, 1952; Peterson, 1974). A number of papers have been published on the numerical modeling of full waveform acoustic logging (White and Zechman, 1968; Tsang and Rader, 1979; Cheng and Toksöz, 1981; Schoenberg

et al., 1981; Paillet and White, 1982; Baker, 1984; Tubman et al., 1984; Schmitt and Bouchon, 1985). These researches are focused on the monopole borehole wave propagations, where the model is azimuthally symmetric, vertically homogeneous and isotropic. The numerical method also extended into the shear wave (or dipole) logging modeling (Kurkjian and Chang, 1986; Winbow, 1988; Schmitt, 1988), logging in porous formation (Rosenbaum, 1974; Cheng et al., 1987; Schmitt, 1989) and in a transversely isotropic formation with the symmetry axis aligned with the borehole axis (White and Tongtaow, 1981; Chan and Tsang, 1983). Some sophisticated methods were also developed to tackle the complicated borehole models, for example, the vertically irregular borehole (Stephen et at., 1985; Bouchon and Schmitt, 1989), the elliptic borehole (Liu and Randall, 1991; Ellefsen, 1990), the borehole in horizontal layered formation (Stephen et at., 1985; Bouchon, 1993), normal modes and waveforms in a general anisotropic formation (Leveille and Seriff, 1989; Nicoletis et al., 1990; Ellefsen, 1990; Sinha et al., 1991; Norris and Sinha, 1993). These numerical methods, mainly the discrete wavenumber method, or a closely related one, in one way or an other depend on some kind of symmetry in the model to use known Green's functions for general solutions. These methods sacrifice the model complexity to gain accuracy and require less computer power. They become impractical for models with a general geometry.

The finite difference method is widely used in wave propagation simulations. It is one of the powerful numerical techniques to provide full wave solutions of the problems. The finite difference method has been applied to seismology since the digital computer became available (Alterman and Karal, 1968; Boore, 1972; Alford et al., 1974; Kelly et al., 1976). Progress in the ability to eliminate artificial reflections (Lindman, 1975; Clayton and Engquist, 1977; Reynolds, 1978; Liao et al., 1984; Randall, 1989; Higdon, 1990) and in the discretization schemes (Madariagea, 1976; Virieux, 1984, 1986; Levander, 1988) make the finite difference method popular. Naturally, the method finds its applications in the borehole wave propagation (Bhashvanija, 1983;

Stephen et at., 1985; Kostek, 1991; Randall, 1991; Leslie and Randall, 1992; Yoon and McMechan, 1992). Most of these borehole applications are for models either of a 2-D in cylindrical coordinate or a 2-D in Cartesian coordinate.

The conventional acoustic logging tool was an analog device to detect the first compressional arrivals. The new digital array monopole and dipole tools provide large amounts of high quality logging data. The hardware advances demand to extract formation properties from the waveforms beyond P and S wave velocities. The development of digital acoustic logging tools also challenges the capability of borehole wave propagation modeling in complex environments. At the same time the emergence of parallel computers provide enough power to make the simulations possible for realistic 3-D borehole models. The goal of this thesis is to develop a three-dimensional finite difference time domain simulation of borehole wave propagation in isotropic and anisotropic formations on the parallel computer and to study the effects of the 3-D structure on monopole and dipole logging.

1.2 Outline

The topics will be covered in the following chapters of the thesis as follows:

Chapter 2 introduces the finite difference method in three dimensional space. Wave propagation in isotropic elastic medium is formulated in a set of first order hyperbolic equations by using velocity and stress. These first-order equations are discretized on a staggered grid. The grid dispersion and anisotropy are analyzed and a stability condition of the scheme is derived. The absorbing boundary condition proposed by Higdon is presented. How to parallel the 3-D finite difference method on the nCUBE computer is also discussed. The last part of this chapter is devoted to the test of the finite difference method in a homogeneous acoustic and elastic media.

In Chapter 3 the application of the 3-D finite difference method to borehole wave propagation in isotropic formations is discussed. Before the application of the 3-D

finite difference method, it is tested again in a fluid filled borehole in a homogeneous and isotropic environment. The monopole and dipole waveforms from the finite difference method are compared with the well-known discrete wavenumber solutions. Then the off-centered source and an elliptic borehole are considered. In the final section of this chapter monopole and dipole logs in a fluid-filled borehole near a horizontal bed and a 45 degree tilted layer are investigated.

In Chapter 4 the 3-D finite difference method is extended into wave propagation in an anisotropic medium. This anisotropic scheme is performed once again on a staggered grid and can be executed on a nCUBE parallel machine. In the homogeneous transversely isotropic solid the finite difference solution is compared with the analytic point force result. The nine elastic constants of an orthorhombic phenolite solid are determined from lab measurements. Then this phenolite solid is used as borehole formation. Due to the anisotropic formation monopole and dipole logs are investigated for the borehole drilled along the X, Y and Z directions. In the borehole drilled in the X direction of phenolite formation the finite difference synthetics are compared with ultrasonic lab measurements done on the scaled borehole model in phenolite solid.

Chapter 5 deals with field data from two sections of a borehole. Both the array full waveform monopole log and the shear wave log are processed and interpreted. The formation P and S wave velocity are determined by threshold detection with cross-correlation correction. The array data are also processed by Prony's method to estimate the borehole Stoneley wave phase velocity and attenuation. The Stoneley wave data are then inverted by using the damped least-square method with amplitude as a weighting function. Inverted shear wave velocities and permeabilities are compared with the shear wave log and the core permeability measurements. The 3-D finite difference method is used to calculate synthetics for interpretation of the field data. Chapter 6 summarizes the important results obtained in this thesis.

Chapter 2

Finite Difference Method

2.1 Introduction

Finite difference method is widely used in wave propagation simulations. It is one of the pure numerical techniques to provide the full wave solutions for problems with a complex geometry. The applications of the finite difference method to seismology can be dated back more than two decades since the digital computer became available. These early applications of the finite difference method were based on the displacement formulation of the wave equations (Alterman and Karal, 1968; Boore, 1972; Alford et al., 1974; Kelly et al., 1976). The second order wave equations are directly discretized on grid. The sharp interior boundaries are treated explicitly to match the displacement and stress boundary conditions. This approach makes the program difficult to write, and limits the flexibility of the method. It also lacks the ability to eliminate the artificial boundary reflections.

The next wave of applications of the finite difference method came with the progress in absorbing boundary condition research and a new staggered grid scheme. First the absorbing boundary condition: Lindman (1975) derived an absorbing boundary condition for the acoustic wave equation by using a one way equation and rational expansion. The formula involves high order derivatives which is a drawback, but with

only three correction terms it can achieve less than 1 percent reflections for the incident angle range from 0 to 89 degrees. A similar absorbing boundary condition can also be obtained for the evanescent waves. Randall (1988, 1989) extended Lindman's idea to the elastic wave case and the staggered grid scheme. It is not very easy to implement Lindman's absorbing boundary condition on a computer. Also it is not very clear how to treat the grid corners and the behavior of the condition when it encounters the lateral inhomogeneity. A very popular absorbing boundary condition was discussed by Clayton and Engquist (1977). It is based on paraxial approximation for the wave equations. There are some improvements to this approach (e.g. Fuyuki and Matsumoto, 1980; Emerman and Stephen, 1983; Stacey, 1988; Renaut and Petersen, 1989). This condition needs special treatment at the corner of the grid. The high order Clayton's absorbing boundary condition also doesn't work well when it encounters lateral discontinuity. Another class of absorbing boundary conditions only involves the derivatives perpendicular to the boundary (Reynolds, 1978; Liao et al., 1984; Higdon, 1986, 1987, 1990; Peng, 1994). The conditions are directly derived in the discretized form. These schemes work well at the boundary with the lateral inhomogeneity. There is no special treatment at the corner of the grid. Another advantage is that it is very easy to implement.

There are a lot of other ideas to eliminate the artificial boundary reflections. Viscous damping can be added near the boundaries of the grid to attenuate incoming waves (Lysmer and Kuhlemeyer, 1969; Kosloff and Kosloff, 1986). The damping can absorb different wave types effectively. It is the easiest absorbing boundary condition to program. The disadvantage is that the damping layer thickness is frequency dependent. It wastes a lot of grids to absorb low frequency waves. Another idea is to combine the one way wave equation with the damping layer to transport the wave energy out of the grid (Israeli and Orszag, 1981). Smith (1974) proposed an interesting way to get rid of the boundary reflections. He solves the problem twice: once with the Dirichlet boundary condition and once with the Newman boundary condition, then

adds the two solutions together to cancel the reflections. But for n artificial boundaries the problem needs to be solved 2^n times. The absorbing boundary conditions can also be constructed from variational principles (Daalen et al., 1992; Broeze and Daalen, 1992). This is a general method and it works with any wave equations, linear or non-linear.

The staggered grid scheme was developed by Madariaga (1976) to model an expanding circle crack in an elastic medium. Virieux (1984,1986) applied the scheme to model SH and P-SV wave propagation problems in the 2-D case. The second order wave equation is reformulated to first order hyperbolic equations using velocity and stress. Levander (1988) extended the staggered grid scheme to the fourth-order finite difference for the P-SV problem. There are two advantages to the staggered-grid scheme over the conventional schemes. First the staggered grid scheme is stable for any Poisson's ratio. Second, the grid dispersion and anisotropy are small and insensitive to Poisson's ratio. Lou and Schuster (1990) presented a staggered grid scheme which requires less computer memory. Peng (1994) applied a staggered grid finite difference method to VSP problems.

From a programming point of view, the finite difference method is very straight forward to implement. But it suffers not only from the grid dispersion and anisotropy, but also from the reflections from the artificial boundaries, which contaminate the solution. These artifacts have to be well controlled to make the finite difference solution meaningful. The benchmark test is used to check the 2-D finite difference method for the elastic wave propagation problem (Virieux, 1986; Levander, 1988). This test compares the finite difference results with the analytic solution of Lamb's problem. It checks the body waves as well as the surface waves. But for the 3-D finite difference method it is not rigorously tested. Igel et al. (1991) showed the seismograms and the snapshots from a 3-D finite difference simulation without any comparisons with the known solutions. Later they did some analysis of finite difference solutions but only for the homogeneous medium (Igel et al., 1992; Rodrigues and Mora, 1992). Frankel

and Vidale (1992) used a 3-D finite difference to simulate seismic wave propagations in a valley. They adopted old fashioned displacement schemes (Kelly et al., 1976). The comparison with the synthetics from the reflectivity method is not very convincing. Yoon and McMechan (1992) displayed a lot of seismograms and snapshots of the 3-D finite difference simulations of wave propagation in the borehole environments. But, again, they didn't show any tests of the method. The 3-D staggered grid scheme was also applied to model the acoustic scattering from seafloor topography (Burns and Stephen, 1990; Burns, 1992).

Even with all the progress made in absorbing the reflection and discretization scheme, most applications of the finite difference method are still for the 2-D problems because of limited computer power. Parallel computing opens the door to realistic 3-D wave propagation simulations. In this chapter we formulate a three-dimensional finite difference time domain method for wave propagation in an isotropic elastic medium. The first order hyperbolic equations are discretized on a staggered grid. The grid dispersion, the grid anisotropy, and the stability condition are analyzed. Then Higdon's absorbing boundary condition is discussed. The implementation of this scheme on the parallel computer is described. Finally, the finite difference method is tested in a homogeneous acoustic and elastic media.

2.2 Formulation

Wave propagation in an elastic medium can be described by the equation of motion as:

$$\rho \frac{\partial^2}{\partial t^2} u_i = \tau_{ij,j} \tag{2.1}$$

where ρ is the density, u_i is the displacement vector, and τ_{ij} is the stress tensor. A comma between subscripts is used for spatial derivatives. The summation convention for repeated subscripts is also used. The generalized Hooke's law links the stress

tensor τ_{ij} to the strain tensor ε_{ij} in the linear fashion

$$\tau_{ij} = c_{ijkl}\varepsilon_{kl} \tag{2.2}$$

where c_{ijkl} are the fourth-order elastic constant tensor, and the strain tensor is defined as:

$$\varepsilon_{ij} = \frac{1}{2}(u_{i,j} + u_{j,i}) \tag{2.3}$$

In the case of an isotropic medium, the elastic constant tensor can be written as

$$c_{ijkl} = \lambda\delta_{ij}\delta_{kl} + \mu(\delta_{ik}\delta_{jl} + \delta_{il}\delta_{jk}) \tag{2.4}$$

where δ_{ij} is the Kronecker delta, that equals 1 as $i = j$; otherwise it equals zero. The isotropic elastic medium has only two independent constants λ and μ, which is called Lamé constants. The P wave velocity α is given by $\sqrt{\frac{\lambda + 2\mu}{\rho}}$ and the S wave velocity β is given by $\sqrt{\frac{\mu}{\rho}}$.

The equations given above are coordinate independent. Here, a Cartesian (x,y,z) coordinate is chosen. Equation (2.1) and (2.2) can be transformed into first-order hyperbolic equations. Equation (2.1) is rewritten using the velocity instead of the displacement. Then one takes the first-order time derivative on both sides of Equation (2.2). Written out in their component form , we have

$$\begin{aligned}
\rho\frac{\partial v_x}{\partial t} &= \frac{\partial \tau_{xx}}{\partial x} + \frac{\partial \tau_{xy}}{\partial y} + \frac{\partial \tau_{xz}}{\partial z} \\
\rho\frac{\partial v_y}{\partial t} &= \frac{\partial \tau_{xy}}{\partial x} + \frac{\partial \tau_{yy}}{\partial y} + \frac{\partial \tau_{yz}}{\partial z} \\
\rho\frac{\partial v_z}{\partial t} &= \frac{\partial \tau_{xz}}{\partial x} + \frac{\partial \tau_{yz}}{\partial y} + \frac{\partial \tau_{zz}}{\partial z}
\end{aligned} \tag{2.5}$$

and

$$
\begin{aligned}
\frac{\partial \tau_{xx}}{\partial t} &= (\lambda + 2\mu)\frac{\partial v_x}{\partial x} + \lambda\frac{\partial v_y}{\partial y} + \lambda\frac{\partial v_z}{\partial z} \\
\frac{\partial \tau_{yy}}{\partial t} &= \lambda\frac{\partial v_x}{\partial x} + (\lambda + 2\mu)\frac{\partial v_y}{\partial y} + \lambda\frac{\partial v_z}{\partial z} \\
\frac{\partial \tau_{zz}}{\partial t} &= \lambda\frac{\partial v_x}{\partial x} + \lambda\frac{\partial v_y}{\partial y} + (\lambda + 2\mu)\frac{\partial v_z}{\partial z} \\
\frac{\partial \tau_{xy}}{\partial t} &= \mu(\frac{\partial v_x}{\partial y} + \frac{\partial v_y}{\partial x}) \\
\frac{\partial \tau_{xz}}{\partial t} &= \mu(\frac{\partial v_x}{\partial z} + \frac{\partial v_z}{\partial x}) \\
\frac{\partial \tau_{yz}}{\partial t} &= \mu(\frac{\partial v_y}{\partial z} + \frac{\partial v_z}{\partial y})
\end{aligned}
\tag{2.6}
$$

where (v_x, v_y, v_z) is the velocity vector. The reason for formulating the second-order wave equations into the first-order hyperbolic system of equations is that once this system is discretized on a staggered grid, it is valid for any Poisson's ratio (Virieux, 1986). The fluid-solid boundary can be treated simply by setting shear modulus to zero. Equations (2.5) and (2.6) are the wave equations in a different form. This velocity and stress formulation is the starting point of the finite difference method.

2.3 Finite Difference Approximation

The first-order hyperbolic equations (2.5) and (2.6) are discretized on a staggered grid, which is shown in Figure 2-1. The velocities and stresses are arranged differently from the usual scheme. The velocity v_x is shifted a half grid in the Y direction, the velocity v_y is shifted a half grid in the X direction, and the velocity v_z is shifted a half grid in all three directions. But the arrangement still centers all the finite difference operators. In the later applications of the finite difference method to borehole wave propagations, the borehole wall will align on the grid with the shear stress. For a 3-D grid in Cartesian coordinates $(m\Delta x, n\Delta y, k\Delta z)$ at time $i\Delta t$, where $\Delta x, \Delta y$ and Δz are the grid size in X, Y, Z directions and Δt is the time step, we define the second order forward finite difference operator in the time D_t as

$$D_t f^i_{m,n,k} = \frac{f^{i+1}_{m,n,k} - f^i_{m,n,k}}{\Delta t} \tag{2.7}$$

and the fourth-order forward finite difference operator in space D_x, D_y and D_z as

$$\begin{aligned}
D_x f^i_{m,n,k} &= \eta_1 \frac{f^i_{m+1,n,k} - f^i_{m,n,k}}{\Delta x} + \eta_2 \frac{f^i_{m+2,n,k} - f^i_{m-1,n,k}}{\Delta x} \\
D_y f^i_{m,n,k} &= \eta_1 \frac{f^i_{m,n+1,k} - f^i_{m,n,k}}{\Delta y} + \eta_2 \frac{f^i_{m,n+2,k} - f^i_{m,n-1,k}}{\Delta y} \\
D_z f^i_{m,n,k} &= \eta_1 \frac{f^i_{m,n,k+1} - f^i_{m,n,k}}{\Delta z} + \eta_2 \frac{f^i_{m,n,k+2} - f^i_{m,n,k-1}}{\Delta z}
\end{aligned} \tag{2.8}$$

where $\eta_1 = \frac{9}{8}$ and $\eta_2 = -\frac{1}{24}$ are the coefficients of the fourth-order finite difference approximation to the first-order derivative. The finite difference approximation to the equations (2.5) and (2.6) with the second-order accuracy in time and the fourth-order accuracy in space can be written as

$$\begin{aligned}
\rho_{m,n+1/2,k} D_t v^{i-1/2}_{x_{m,n+1/2,k}} &= D_x \tau^i_{xx_{m+1/2,n+1/2,k}} + D_y \tau^i_{xy_{m,n+1,k}} \\
&\quad + D_z \tau^i_{xz_{m,n+1/2,k+1/2}} \\
\rho_{m+1/2,n,k} D_t v^{i-1/2}_{y_{m+1/2,n,k}} &= D_x \tau^i_{xy_{m+1,n,k}} + D_y \tau^i_{yy_{m+1/2,n+1/2,k}} \\
&\quad + D_z \tau^i_{yz_{m+1/2,n,k+1/2}} \\
\rho_{m+1/2,n+1/2,k+1/2} D_t v^{i-1/2}_{z_{m+1/2,n+1/2,k+1/2}} &= D_x \tau^i_{xz_{m+1,n+1/2,k+1/2}} \\
&\quad + D_y \tau^i_{yz_{m+1/2,n+1,k+1/2}} + D_z \tau^i_{zz_{m+1/2,n+1/2,k+1}}
\end{aligned} \tag{2.9}$$

and

$$\begin{aligned}
D_t \tau^i_{xx_{m+1/2,n+1/2,k}} &= (\lambda + 2\mu)_{m+1/2,n+1/2,k} D_x v^{i+1/2}_{x_{m+1,n+1/2,k}} \\
&\quad + \lambda_{m+1/2,n+1/2,k} D_y v^{i+1/2}_{y_{m+1/2,n+1,k}} \\
&\quad + \lambda_{m+1/2,n+1/2,k} D_z v^{i+1/2}_{z_{m+1/2,n+1/2,k+1/2}} \\
D_t \tau^i_{yy_{m+1/2,n+1/2,k}} &= \lambda_{m+1/2,n+1/2,k} D_x v^{i+1/2}_{x_{m+1,n+1/2,k}} \\
&\quad + (\lambda + 2\mu)_{m+1/2,n+1/2,k} D_y v^{i+1/2}_{y_{m+1/2,n+1,k}}
\end{aligned}$$

$$
\begin{aligned}
& & & +\lambda_{m+1/2,n+1/2,k} D_z v^{i+1/2}_{z_{m+1/2,n+1/2,k+1/2}} \\
D_t \tau^i_{zz_{m+1/2,n+1/2,k}} &= & & \lambda_{m+1/2,n+1/2,k} D_x v^{i+1/2}_{x_{m+1,n+1/2,k}} \\
& & & +\lambda_{m+1/2,n+1/2,k} D_y v^{i+1/2}_{y_{m+1/2,n+1,k}} \\
& & & +(\lambda+2\mu)_{m+1/2,n+1/2,k} D_z v^{i+1/2}_{z_{m+1/2,n+1/2,k+1/2}} \\
D_t \tau^i_{xz_{m,n+1/2,k+1/2}} &= & & \mu_{m,n+1/2,k+1/2}(D_z v^{i+1/2}_{x_{m,n+1/2,k+1}} + D_x v^{i+1/2}_{z_{m+1/2,n+1/2,k+1/2}}) \\
D_t \tau^i_{yz_{m+1/2,n,k+1/2}} &= & & \mu_{m+1/2,n,k+1/2}(D_z v^{i+1/2}_{y_{m+1/2,n,k+1}} + D_y v^{i+1/2}_{z_{m+1/2,n+1/2,k+1/2}}) \\
D_t \tau^i_{xy_{m,n,k}} &= & & \mu_{m,n,k}(D_y v^{i+1/2}_{x_{m,n+1/2,k}} D_x v^{i+1/2}_{y_{m+1/2,n,k}})
\end{aligned}
\tag{2.10}
$$

The medium parameters ρ, λ and μ are given at a grid point $(m+\frac{1}{2}, n+\frac{1}{2}, k)$, where the normal stresses $\tau_{xx}, \tau_{yy}, \tau_{zz}$ are assigned (see Figure 2-1). In the calculation to update velocities, the needed density values are obtained from the average of the two assigned densities nearby. This can be written as

$$
\begin{aligned}
\rho_{m,n+1/2,k} &= \frac{\rho_{m+1/2,n+1/2,k} + \rho_{m-1/2,n+1/2,k}}{2} \\
\rho_{m+1/2,n,k} &= \frac{\rho_{m+1/2,n+1/2,k} + \rho_{m+1/2,n-1/2,k}}{2} \\
\rho_{m+1/2,n+1/2,k+1/2} &= \frac{\rho_{m+1/2,n+1/2,k+1} + \rho_{m+1/2,n+1/2,k}}{2}
\end{aligned}
\tag{2.11}
$$

The shear moduli used to update the shear stress are determined by the harmonic average of the four shear moduli nearby instead of the arithmetic average (Kostek, 1991). The reason is that the propagated wavelength is much larger than the grid size.

$$
\begin{aligned}
\frac{4}{\mu_{m,n,k}} &= \frac{1}{\mu_{m+1/2,n+1/2,k}} + \frac{1}{\mu_{m-1/2,n+1/2,k}} \\
& \quad + \frac{1}{\mu_{m+1/2,n-1/2,k}} + \frac{1}{\mu_{m-1/2,n-1/2,k}} \\
\frac{4}{\mu_{m,n+1/2,k+1/2}} &= \frac{1}{\mu_{m+1/2,n+1/2,k}} + \frac{1}{\mu_{m+1/2,n+1/2,k+1}} \\
& \quad + \frac{1}{\mu_{m-1/2,n+1/2,k}} + \frac{1}{\mu_{m-1/2,n+1/2,k+1}} \\
\frac{4}{\mu_{m+1/2,n,k+1/2}} &= \frac{1}{\mu_{m+1/2,n+1/2,k}} + \frac{1}{\mu_{m+1/2,n+1/2,k+1}}
\end{aligned}
\tag{2.12}
$$

$$+\frac{1}{\mu_{m+1/2,n-1/2,k}}+\frac{1}{\mu_{m+1/2,n-1/2,k+1}}$$

This harmonic average method can automatically put the shear modulus zero at the fluid-solid boundary.

2.4 Dispersion Analysis and Stable Condition

In order to do dispersion analysis, we consider a plane wave $e^{i(\omega t-k_x x-k_y y-k_z z)}$, which makes an angle of $\gamma_1, \gamma_2, \gamma_3$ with the x, y, z axis, respectively. These angles can be determined by $cos\gamma_1 = \frac{k_x}{k}$, $cos\gamma_2 = \frac{k_y}{k}$ and $cos\gamma_3 = \frac{k_z}{k}$, where k is the wavenumber. It is obvious that these angles satisfy

$$cos^2\gamma_1 + cos^2\gamma_2 + cos^2\gamma_3 = 1 \tag{2.13}$$

The dispersion relation for the P wave is

$$(\frac{\omega}{\alpha})^2 = k_x^2 + k_y^2 + k_z^2 \tag{2.14}$$

where ω is the angular frequency. The dispersion relation for the S wave is

$$(\frac{\omega}{\beta})^2 = k_x^2 + k_y^2 + k_z^2 \tag{2.15}$$

The first order time derivative $\frac{\partial}{\partial t}$ is approximated with the second-order centered finite difference on the staggered grid and is equivalent to approximating ω as numerical ω_n . This numerical ω_n is given by

$$\omega_n = \frac{2}{\Delta t} sin(\frac{\Delta t}{2}\omega) \tag{2.16}$$

It is very easy to show that

$$\lim_{\Delta t \to 0} \omega_n = \omega \tag{2.17}$$

It says that the finite difference becomes derivative as Δt goes to zero. The first-order spatial derivatives are approximated by the fourth order centered finite difference on the staggered grid, which is equivalent to approximated k_x, k_y, k_z as numerical $k_{x_n}, k_{y_n}, k_{z_n}$. These numerical k_{x_n}, k_{y_n} and k_{z_n} are given by

$$\begin{aligned} k_{x_n} &= \eta_1 \frac{2}{\Delta x} sin(\frac{\Delta x}{2} k_x) + \eta_2 \frac{2}{\Delta x} sin(\frac{3\Delta x}{2} k_x) \\ k_{y_n} &= \eta_1 \frac{2}{\Delta y} sin(\frac{\Delta y}{2} k_y) + \eta_2 \frac{2}{\Delta y} sin(\frac{3\Delta y}{2} k_x) \\ k_{z_n} &= \eta_1 \frac{2}{\Delta z} sin(\frac{\Delta z}{2} k_x) + \eta_2 \frac{2}{\Delta z} sin(\frac{3\Delta z}{2} k_x) \end{aligned} \tag{2.18}$$

We can also show that:

$$\begin{aligned} \lim_{\Delta x \to 0} k_{x_n} &= \eta_1 + 3\eta_2 = 1 \\ \lim_{\Delta y \to 0} k_{y_n} &= \eta_1 + 3\eta_2 = 1 \\ \lim_{\Delta z \to 0} k_{z_n} &= \eta_1 + 3\eta_2 = 1 \end{aligned} \tag{2.19}$$

So the numerical dispersion relation of the P wave becomes

$$(\frac{\omega_n}{\alpha})^2 = k_{x_n}^2 + k_{y_n}^2 + k_{z_n}^2 \tag{2.20}$$

To simplify the analysis we assume that $\Delta x = \Delta y = \Delta z = \Delta$. This assumption is always used for the numerical simulations in the later part of this thesis. We introduce non-dimensional quantity ξ as

$$\xi = \alpha \frac{\Delta t}{\Delta} \tag{2.21}$$

and the non-dimensional quantity H as

$$H = \frac{\Delta}{\lambda_w} \tag{2.22}$$

where λ_w is the wavelength. The quantity ξ controls the numerical dispersion and H controls the sample rate per wavelength. q_p is defined as the ratio of the numerical P wave velocity to the true P wave velocity. Substituting ξ and H into equation (2.20) and with some algebra manipulations we obtain:

$$q_p = \frac{1}{\pi \xi H} sin^{-1}(\xi \sqrt{A_x^2 + A_y^2 + A_z^2}) \tag{2.23}$$

where A_x, A_y and A_z are defined as

$$\begin{aligned} A_x &= \eta_1 sin(\pi H cos\gamma_1) + \eta_2 sin(3\pi H cos\gamma_1) \\ A_y &= \eta_1 sin(\pi H cos\gamma_2) + \eta_2 sin(3\pi H cos\gamma_2) \\ A_z &= \eta_1 sin(\pi H cos\gamma_3) + \eta_2 sin(3\pi H cos\gamma_3) \end{aligned} \tag{2.24}$$

It is obvious that q_p is independent of Poisson's ratio ν. Similarly, q_s, defined as the ratio of the numerical S wave velocity to the true S wave velocity, can be obtained as

$$q_s = \frac{\alpha}{\beta \pi \xi H} sin^{-1}(\frac{\beta}{\alpha \xi} \sqrt{A_x^2 + A_y^2 + A_z^2}) \tag{2.25}$$

To check the simple case, we consider the second-order finite difference (set $\eta_1 = 1$ and $\eta_2 = 0$) in two dimensions ($A_z = 0$). Equation (2.23) and (2.25) are reduced to the dispersion formulas given by Virieux (1986). Notice the definition difference of the quantity ξ, which has a $\sqrt{2}$ factor.

Dispersions of P wave phase velocity caused by the discretization are shown in Figure 2-2. Three different wave propagation directions are considered: (1) along the X axis ($\gamma_1 = 0, \gamma_2 = 90, \gamma_3 = 90$). (2) along the diagonal of the X-Y plane and perpendicular to the Z axis ($\gamma_1 = 45, \gamma_2 = 45, \gamma_3 = 90$). (3) along the diagonal of a cube ($\gamma_1 = 54.7, \gamma_2 = 54.7, \gamma_3 = 54.7$). ξ is set at $\frac{0.8}{\sqrt{3}}$. The fourth-order finite difference and the second-order finite difference are shown in plot (A) and (B), respectively. For the second-order finite difference the numerical P wave velocity is slower than the true P wave velocity. For the fourth-order finite difference this is not

always the case. The numerical velocity is greater or smaller than the true velocity depending on the wave propagation direction and the grid size.

Dispersions of S wave phase velocity are shown in Figure 2-3 with the same propagation directions and ξ value as the P wave. In the shear wave case, the dispersion is dependent on the Poisson's ratio. Here ν equals 0.25. The numerical shear wave velocity is generally slower than the true shear wave velocity for both the fourth-order and the second-order finite difference. The q_s does not degrade as Poisson's ratio ν approaches 0.5, as shown in Figure 2-4, where ν is set at 0.4999. This is the reason why the staggered grid is good for modeling the fluid-solid boundary.

The grid anisotropy is caused by the wave traveling on the discrete grid in a different direction with a different velocity. This anisotropy is shown in Figure 2-5 for the P wave, and Figure 2-6 for the S wave. The fourth-order finite difference is used. In the plots the two axes of the angles are related to the propagation direction through

$$\begin{aligned} cos\gamma_1 &= cos(angle1) \\ cos\gamma_2 &= sin(angle1) * cos(angle2) \\ cos\gamma_3 &= sin(angle1) * cos(angle2) \end{aligned} \tag{2.26}$$

The following values are used in the calculations: $H = 0.2$, $\xi = \frac{0.8}{\sqrt{3}}$ and $\nu = 0.25$. There is about 1 percent P wave and S wave anisotropy from the discretization in the plot. For 10 samples per wavelength the grid anisotropy can be reduced to less than 0.1 percent.

For both P and S waves, the fourth-order finite difference has much less dispersion and grid anisotropy than the second-order one. The rule of thumb is that we need 10 samples per wavelength for the second-order finite difference, and 5 samples per wavelength for the fourth-order finite difference to control the dispersion and the anisotropy at less than 1%.

The dispersion analysis can also be used to derive the stability condition of the scheme. The stability condition from Equation (2.23) is obtained by setting the argument of sin^{-1} at less than 1 for any incident angle $\gamma_1, \gamma_2, \gamma_3$, that is:

$$\xi\sqrt{3(|\eta_1| + |\eta_2|)^2} < 1 \tag{2.27}$$

put into the usual stable condition form

$$\Delta t < \frac{\Delta}{\sqrt{3}\alpha(|\eta_1| + |\eta_2|)} \tag{2.28}$$

similarly the stable condition from Equation (2.25) is

$$\Delta t < \frac{\Delta}{\sqrt{3}\beta(|\eta_1| + |\eta_2|)} \tag{2.29}$$

Because Equation (2.28) is more restrictive than (2.29) ($\alpha > \beta$), the real stability condition is Equation (2.28). In the 2-D case ($A_z = 0$) the stable condition is

$$\Delta t < \frac{\Delta}{\sqrt{2}\alpha(|\eta_1| + |\eta_2|)} \tag{2.30}$$

This is the same as the one given by Levander (1988). In his paper the condition is misprinted. For the second-order finite difference ($\eta_1 = 1$ and $\eta_2 = 0$) the condition is

$$\Delta t < \frac{\Delta}{\sqrt{3}\alpha} \tag{2.31}$$

the same as the one given by Virieux (1986) for multi-dimension (n=3). The fourth-order stability condition is more restrictive than the second-order one. This is the price paid for less grid dispersion and grid anisotropy.

2.5 Absorbing Boundary Condition

The absorbing boundary condition is applied to the outside boundaries of the grid to minimize the reflections. Higdon's absorbing boundary condition is used (Hig-

don 1986, 1987, 1990). In his series of papers he worked directly with a discretized wave equation, rather than first finding the analytical boundary conditions and then discretizing them. These conditions turn out to be discretizations of some analytical boundary conditions that are perfectly absorbing for waves traveling at certain angles of incidence. These conditions are generalized for arbitrary angles of incidence and for the elastic wave problem.

For the purpose of application to elastic wave propagation problems, the absorbing boundary condition operator

$$B = \prod_{j=1}^{m} (c_j \frac{\partial}{\partial t} - \alpha \frac{\partial}{\partial x}) \tag{2.32}$$

is applied to each component of the displacement vector at $x = x_l$. m is the order of the absorbing boundary condition. x_l is the left boundary along the X axis. For the right boundary along the X axis at $x = x_r$ the minus sign in (2.32) should be replaced by a plus sign. The coefficients c_j are positive constants for all j. The similar operators can be used for the boundaries along the Y and Z axis by replacing $\frac{\partial}{\partial x}$ in Equation (2.32) with $\frac{\partial}{\partial y}$ or $\frac{\partial}{\partial z}$.

The jth operator in (2.32) is perfectly absorbing for the P wave traveling at angles of incidence $\pm cos^{-1} c_j$, and for the S wave traveling at angles of incidence $\pm cos^{-1}(c_j \frac{\beta}{\alpha})$. As an example, in case of $m = 2$, we can chose $c_1 = 1$ and $c_2 = \frac{\alpha}{\beta}$ to absorb both the P and the S wave at zero incident angle perfectly.

Define operators E_x and E_t as a forward shift in x and t

$$\begin{aligned} E_x f^i_{m,n,k} &= f^i_{m+1,n,k} \\ E_t f^i_{m,n,k} &= f^{i+1}_{m,n,k} \end{aligned} \tag{2.33}$$

The absorbing boundary condition operator in Equation (2.32) can be approximated by the finite difference operator as

$$D(E_x, E_t^{-1}) = \prod_{j=1}^{m} c_j(\frac{I - E_t^{-1}}{\Delta t})[(1-a)I + aE_x] - \alpha(\frac{E_x - I}{\Delta x})[(1-b)I + bE_t^{-1}] \quad (2.34)$$

parameters a and b give weighted space and time averages. Different a and b values result in different schemes. For example:

1. Forward Euler: $a = 0$, $b = 1$. The stencil has an "L" shape.

2. Backward Euler: $a = 0$, $b = 0$. The stencil has an inverted "L" shape.

3. Box scheme: $a = \frac{1}{2}$, $b = \frac{1}{2}$.

If the boundary value of the displacement u is needed at $x = x_0$, then the absorbing boundary condition is

$$D(E_x, E_t^{-1})u^{i+1}|_{x=x_0} = 0 \quad (2.35)$$

We solve this equation for u^{i+1} using the previous time step values. In our staggered grid scheme, this condition not only applied to the velocities but also to the stresses.

Higdon's absorbing boundary condition can be applied directly to the corner of the grid. It only involves the differences perpendicular to the boundary, so it works well at the boundary with lateral discontinuity. The implementation is straight forward. Incompatibility can be removed by adding small positive constants δ_j, at least one δ_j is non-zero, to the absorbing boundary condition operator. Thus it becomes

$$B = \prod_{j=1}^{m}(c_j\frac{\partial}{\partial t} - \alpha\frac{\partial}{\partial x} + \delta_j) \quad (2.36)$$

In the simple acoustic case the P wave reflection coefficient has magnitude

$$\prod_{j=1}^{m}|\frac{cos\theta_j - cos\theta}{cos\theta_j + cos\theta}| \quad (2.37)$$

where θ_j is the perfectly absorbing angle of incidence. For m = 2 , $\theta_1 = 0$ and $\theta_2 = 45$, the reflection coefficient is plotted in Figure 2-7 as an example.

2.6 Parallel Implementation

Applications of the finite difference method to 3-D problems are limited by the memory and speed of the computer. Parallel computing provides a new means to overcome these limitations. In the finite difference method all the calculations involve only local interactions of the velocities and stresses. For example, in the fourth-order finite difference scheme only two nearby grid points data are needed to update the current grid point. This can be efficiently executed on a multiple instruction and multiple data (MIMD) parallel computer. Each processor is assigned a subset of the whole grid. The finite difference is performed on this subset grid. When the calculations come to the grid near the subset boundary of the current processor, it requires velocity and stress values beyond the current processor. These required data are obtained from the nearby processor through communication. The communication time usually is short in comparison to the finite difference calculation time. There is a Grid Decomposition Package (GDP) on the nCUBE to do the job described above. The GDP can decompose a N dimension grid with given interactive lengths. The GDP assigns the subset of the grid to the processor in such a way that the subsets that are the neighbors in the grid will also be neighbors in the hypercube of processors. In the 3-D case these subsets are chosen to be as cubical as possible. This is because in the finite difference method the computation time is proportional to the volume of the subset and the communication time is proportional to the surface area. The best ratio of volume to surface that can be achieved is the cubical subgrid. The staggered-grid fourth-order finite difference scheme we discussed above is paralleled using the GDP on nCUBE 2. For example, a full elastic wave propagation in a $100 \times 100 \times 100$ grid is performed using the fourth-order finite difference scheme. The subgrid of $12 \times 12 \times 12$ is assigned to each processor when we use 512 of them. The subgrid is increased to $25 \times 25 \times 25$ when we use 64 processors. The CPU time of the 100 time step calculations versus the number of processors is plotted in Figure 2-8. The log scale is used for processor numbers in the plot. Due to the limitation of 4 Mb memory on each processor we

need at least 64 processors to run a $100 \times 100 \times 100$ problem. The plot shows roughly that CPU time decreases linearly with the log number of processors.

2.7 Test of Finite Difference Method

We developed the fourth-order 3-D finite difference time domain method on the staggered grid. The scheme is implemented on a nCUBE 2 parallel computer. We first test the finite difference method in a homogeneous acoustic medium with a point explosion as source. Then we test it in a homogeneous elastic medium with a point force as source.

2.7.1 Homogeneous Acoustic Medium

The test is started with the simplest model: the homogeneous acoustic medium. Although the finite difference method is developed for the elastic wave propagation problems, the implementation of the acoustic medium is simply by setting shear moduli at zero. The physical parameters of the acoustic medium are listed in Table 2.1 under the entry fluid. The source is a point explosion. The source time function is a Kelly wavelet at center frequency 2.5 kHz; see Appendix A for more details about the Kelly wavelet. A Kelly wavelet is plotted in Figure 2-9 for the center frequency 2.5 kHz. The Kelly source time function is used in all the finite difference calculations in this thesis. The wavelength in water at the center frequency is 0.6m. The grid size is taken as $\frac{1}{20}$ of this wavelength, which equals 0.03 m. The time step size is 0.008 ms, which is stable for maximum P-wave velocity of 1500 m/s. A grid of $50 \times 50 \times 120$ is used. The source is located at grid point (25, 25, 25) and the pressure receiver at (25, 25, 105). The source receiver distance is 2.4 m, which is 4 wavelengths. The second order Higdon's absorbing boundary condition is applied on all six boundary planes. The two preferred absorbing angles for the boundary along the Z axis are chosen as 5 degrees. The two preferred absorbing angles for the boundary along the

X and Y axis are chosen as 0 and 45 degrees, respectively.

The analytic solution is very simple in this case. It is the source time function at retarded time $t - \frac{r}{\alpha}$ and the amplitude reduced by factor $\frac{1}{r}$, where r is the source-receiver distance. The finite difference result and the analytic solution are plotted in Figure 2-10. The amplitudes are normalized. The two waveforms are identical. The snapshot of the pressure wavefield at time 1.2 ms is plotted in Figure 2-11. It shows the expansion of the P wavefront. The snapshot demonstrates that Higdon's absorbing boundary condition is very effective in the acoustic medium. Another way to check the comparison is in the frequency domain. The waveforms from the finite difference and analytic solutions are transformed to frequency domain by FFT. They are plotted in Figure 2-12 from 0 to 20 kHz. The log scale is used for the vertical axis. Within the source frequency range (0 to 8 kHz) the two solutions agree very well. For frequency higher than 8 kHz, we see the numerical noise from the finite difference solution. This numerical noise is about 5 order of magnitudes smaller than the signal.

To simulate a point explosion source in the finite difference scheme the source time function is fed into the normal stresses $\tau_{xx}, \tau_{yy}, \tau_{zz}$. In the homogeneous acoustic medium we know the P wave amplitude will decrease by factor of $\frac{1}{r}$ as it travels away from the point source. The amplitudes from the finite difference calculation from the point explosion source are plotted against $\frac{1}{r}$ in Figure 2-13. The distance is normalized by the center wavelength. The finite difference amplitudes follow $\frac{1}{r}$ excellently. The nearest data point from the finite difference calculation is just one grid away from the source. This demonstrates that the point source is implemented correctly in the scheme.

2.7.2 Homogeneous Elastic Medium

The next test is the homogeneous elastic medium. The homogeneous acoustic medium propagates only the compressional body wave. But the homogeneous elastic medium

can propagate compressional as well as shear body waves. The physical parameters of the medium are listed in Table 2.1 under the solid entry. All geometries are the same as in the acoustic test. The grid size is determined by $\frac{1}{20}$ of the wavelength of the shear wave at center frequency, which is 0.046 m. The time step size is 0.005 ms. The source-receiver distance is 4 wavelengths of the shear wave and 2.3 wavelengths of the P wave.

The point force solution in a homogeneous elastic medium is given in Appendix B. This solution includes the near field term, the far field P wave term, and the far field S wave term. The near field term includes both P and S wave motions. First the point vertical force (f_z) is used as the source. The receiver records the vertical velocity (v_z). The finite difference and analytic solutions are plotted in Figure 2-14. Due to the radiation pattern of the shear wave, the shear wave amplitude is zero at this position. The seismogram shows the far field P wave term at the front and the near field term at the back. The finite difference and the analytic solutions are almost identical.

Next, the point horizontal force (f_x) is used as the source. The receiver records the velocity v_x. The comparison of the finite difference synthetic with the analytic solution is shown in Figure 2-15. The radiation pattern of the P wave gives the zero amplitude at this receiver position. The seismogram shows a small near field term and a very large shear wave arrival. Once again the comparison is excellent.

The snapshot of the vertical velocity field due to a vertical force is shown in Figure 2-16. The field is dominated by the shear wave, which is symmetric about the vertical Z axis. A very small P wave can be observed at the lower part of the image. This test demonstrates that the finite difference method can model not only the far field P and S waves, but also the near field term. The seismograms and the wavefield image also show that Higdon's absorbing boundary condition works very well in the elastic medium.

2.8 Conclusion

In this chapter we developed the 3-D time domain staggered grid finite difference method, which is the fourth-order accuracy in space and the second-order accuracy in time. The scheme is parallelized on a nCUBE 2 computer. The dispersion analysis shows that as a rule of thumb 5 samples per wavelength are needed to suppress the grid dispersion and anisotropy. The stable condition of the scheme is obtained. The tests show that in the homogeneous acoustic and elastic medium the finite difference solutions match the analytic solutions excellently. In the elastic medium the finite difference method can model the far field P and S waves as well as the near field term accurately. The tests also demonstrate that the second-order Higdon's absorbing boundary condition works very well in an acoustic and elastic medium.

	P wave velocity α (m/s)	S wave velocity β (m/s)	density ρ (g/c.c.)
Fluid	1500	—	1.0
Solid	4000	2300	2.3

Table 2.1: The velocity and the density values of the acoustic and elastic medium used in the test.

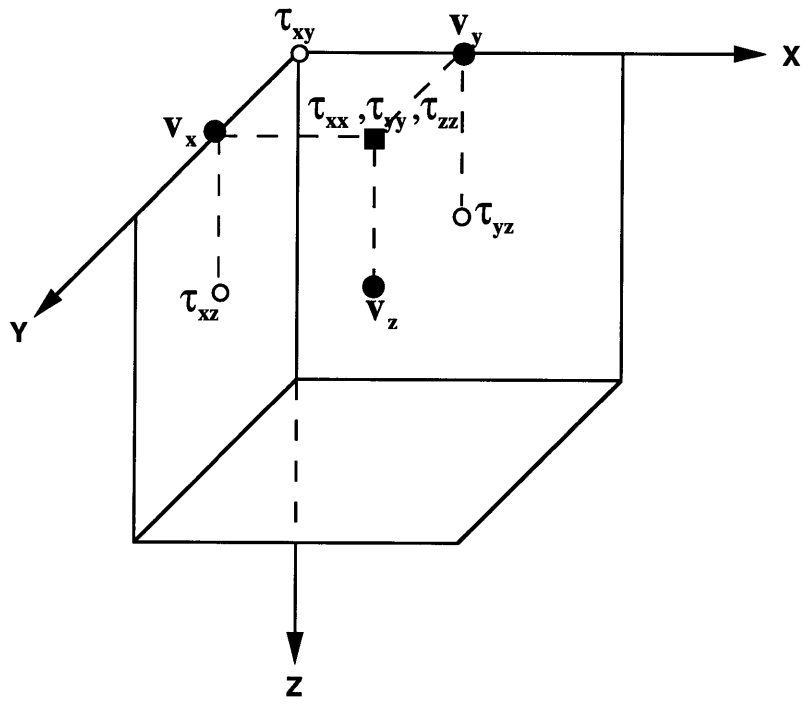

Figure 2-1: Staggered grid used to discretize Equation (2.5) and (2.6). Solid circles represent the velocities. Open circles represent the shear stresses. The solid square represents the normal stresses.

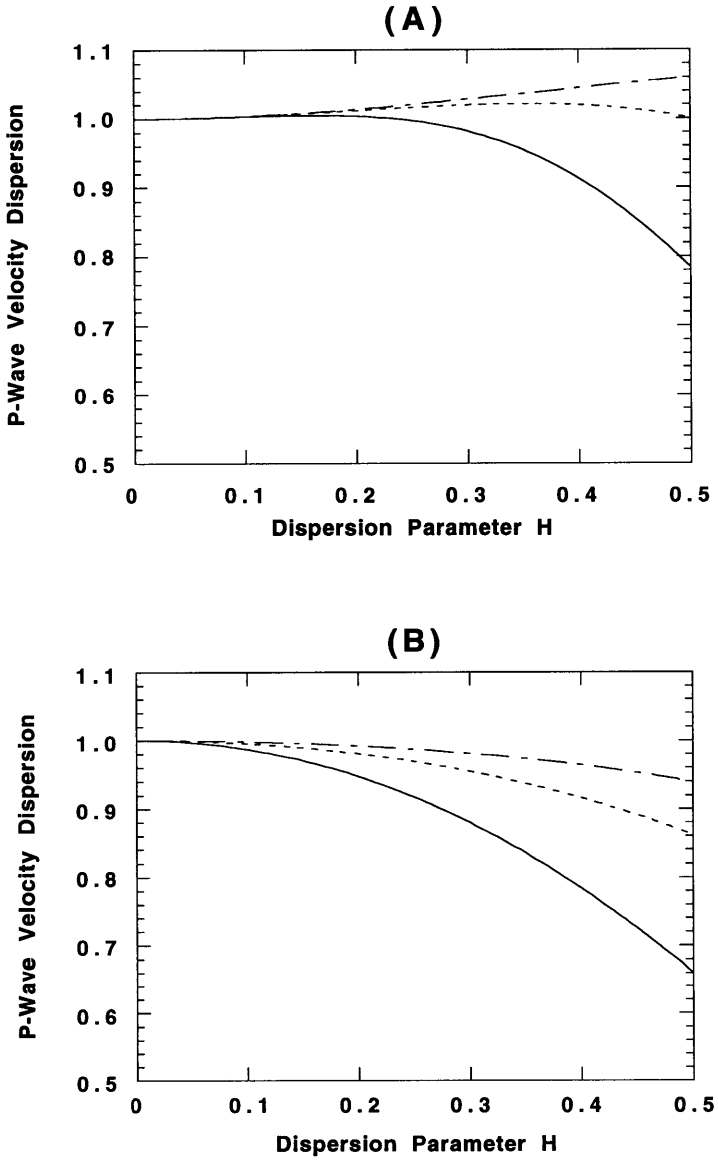

Figure 2-2: Normalized P wave velocity dispersion versus sample rate per wavelength. (A) the fourth-order finite difference. (B) the second-order finite difference. Solid line for direction ($\gamma_1 = 0, \gamma_2 = 90, \gamma_3 = 90$), dashed line for direction ($\gamma_1 = 45, \gamma_2 = 45, \gamma_3 = 90$) and dash/dot for direction ($\gamma_1 = 54.7, \gamma_2 = 54.7, \gamma_3 = 54.7$).

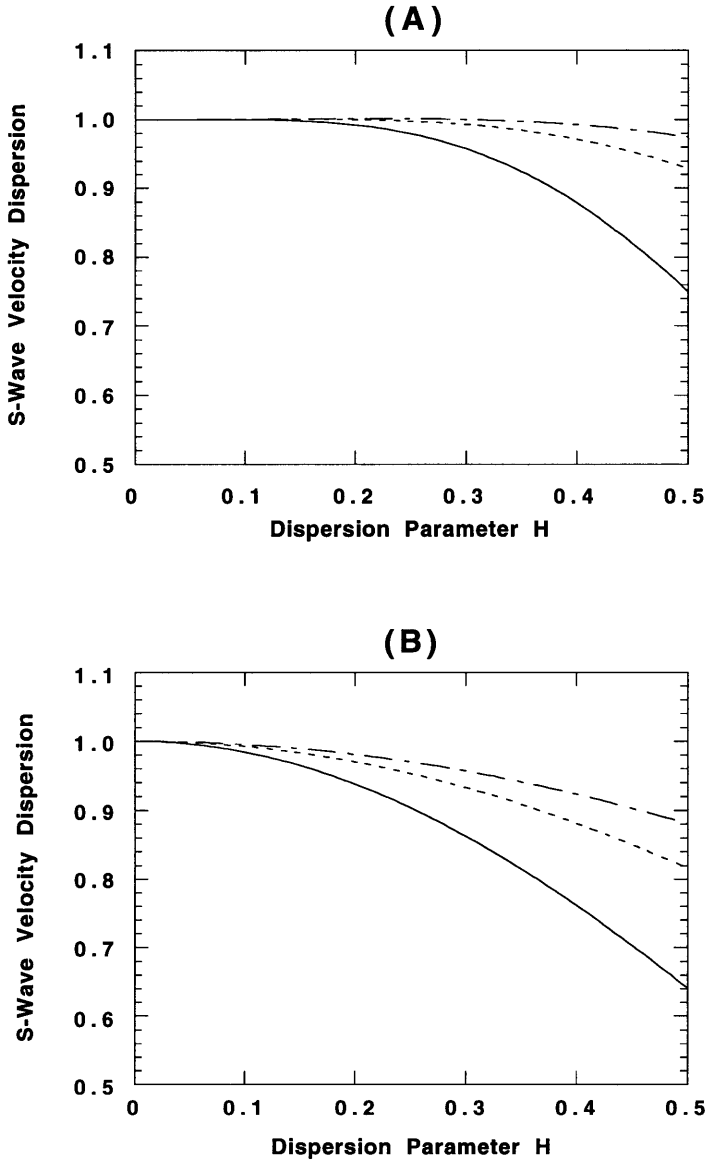

Figure 2-3: Normalized S wave velocity dispersion versus sample rate per wavelength. (A) the fourth-order finite difference. (B) the second-order finite difference. $\nu = 0.25$. Solid line for direction ($\gamma_1 = 0, \gamma_2 = 90, \gamma_3 = 90$), dashed line for direction ($\gamma_1 = 45, \gamma_2 = 45, \gamma_3 = 90$) and dash/dot line for direction ($\gamma_1 = 54.7, \gamma_2 = 54.7, \gamma_3 = 54.7$).

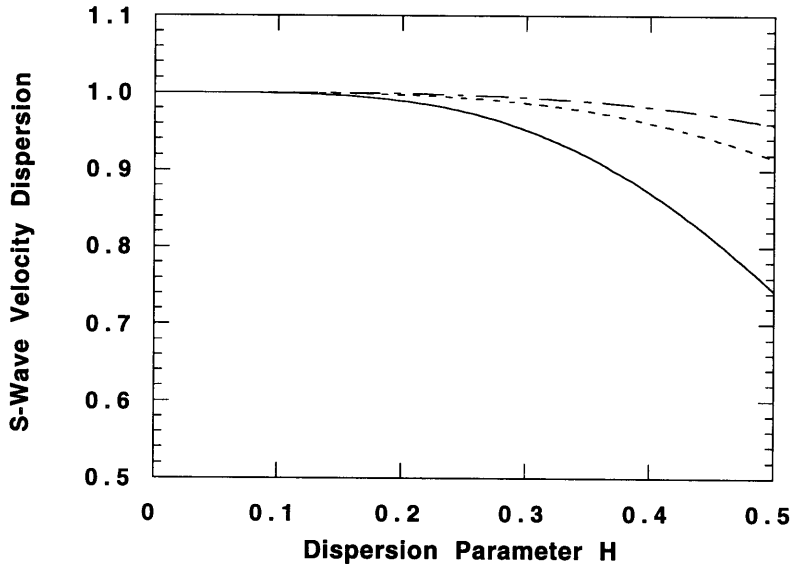

Figure 2-4: Normalized S wave velocity dispersion versus sample rate per wavelength for the fourth-order finite difference. $\nu = 0.4999$. Solid line for direction ($\gamma_1 = 0, \gamma_2 = 90, \gamma_3 = 90$), dashed line for direction ($\gamma_1 = 45, \gamma_2 = 45, \gamma_3 = 90$) and dash/dot line for direction ($\gamma_1 = 54.7, \gamma_2 = 54.7, \gamma_3 = 54.7$).

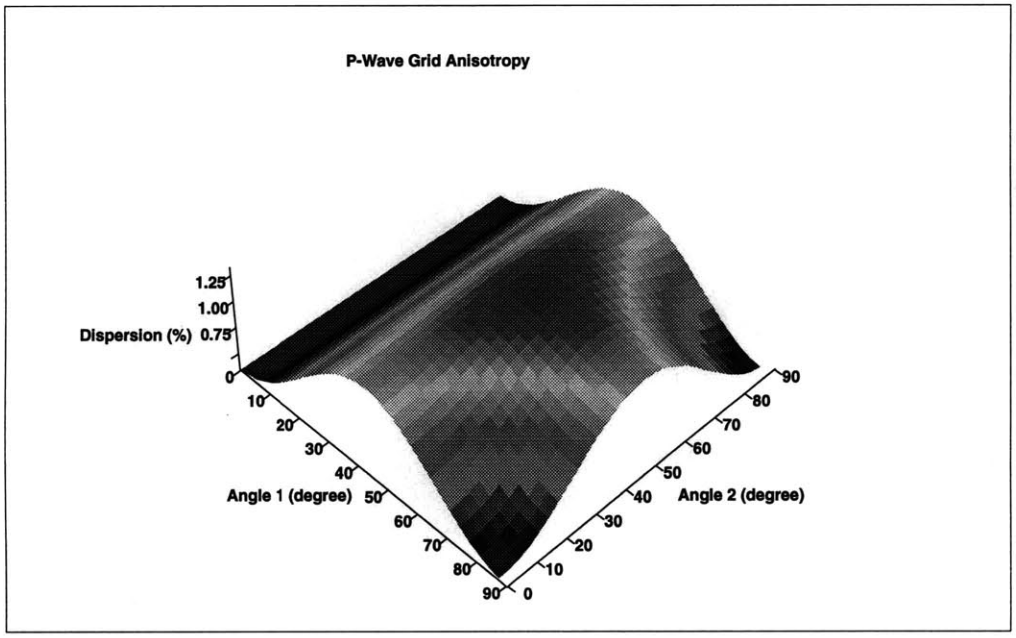

Figure 2-5: The fourth-order finite difference grid anisotropy for the P wave. H=0.2. Conversions from Angle 1 and Angle 2 to $\gamma_{1,2,3}$ are given in Equation (2.26).

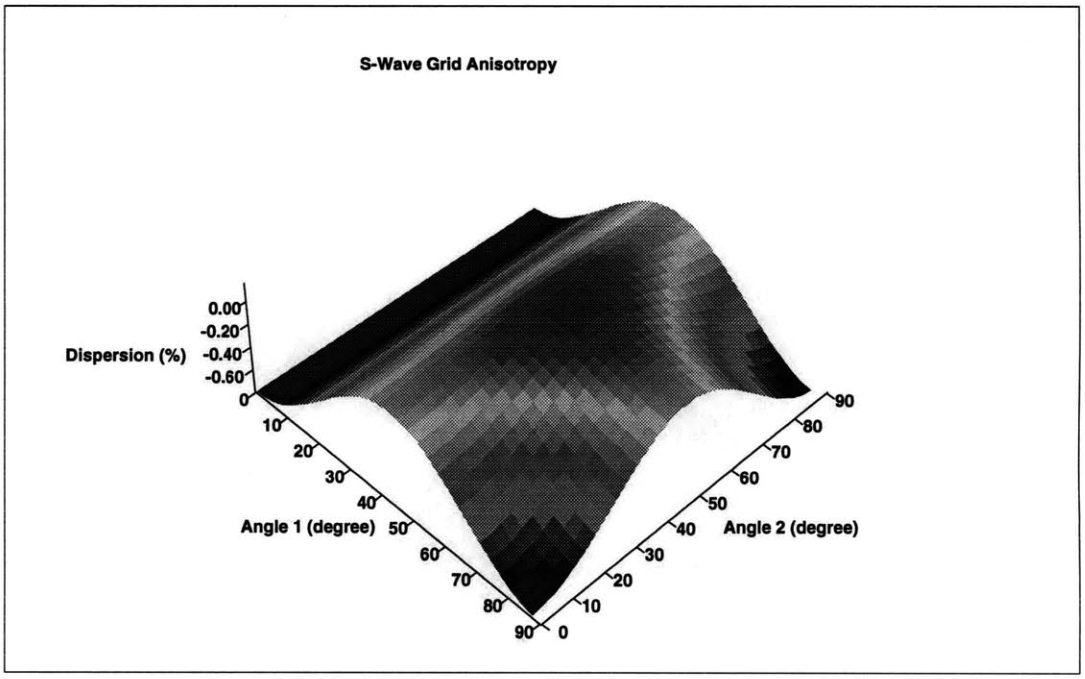

Figure 2-6: The fourth-order finite difference grid anisotropy for the S wave. H=0.2. and $\nu = 0.25$. Conversions from Angle 1 and Angle 2 to $\gamma_{1,2,3}$ are given in Equation (2.26).

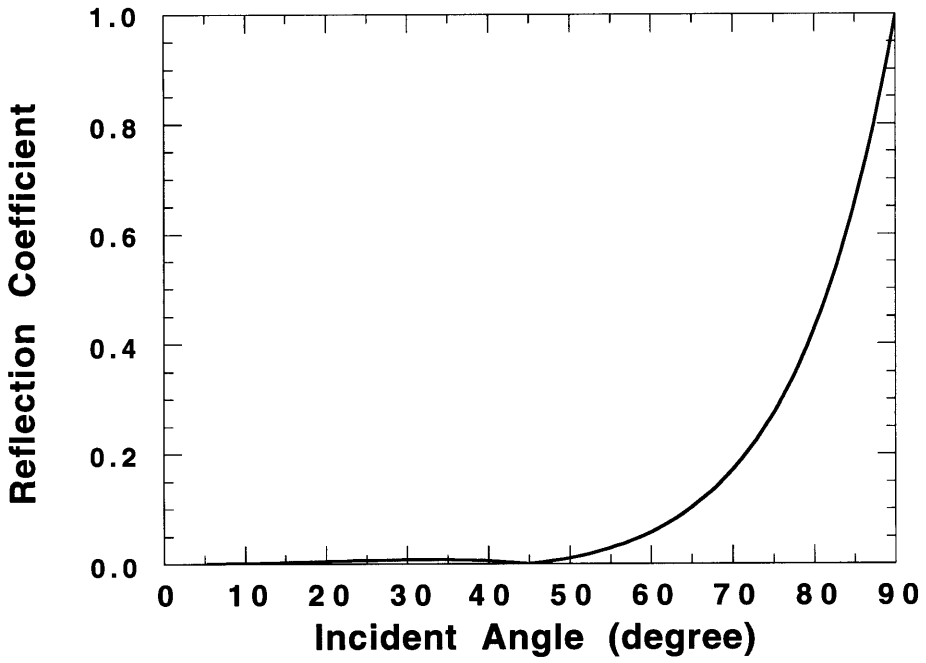

Figure 2-7: Reflection coefficient of the acoustic case. The perfect absorbing angles are chosen as 0 and 45 degrees. m = 2.

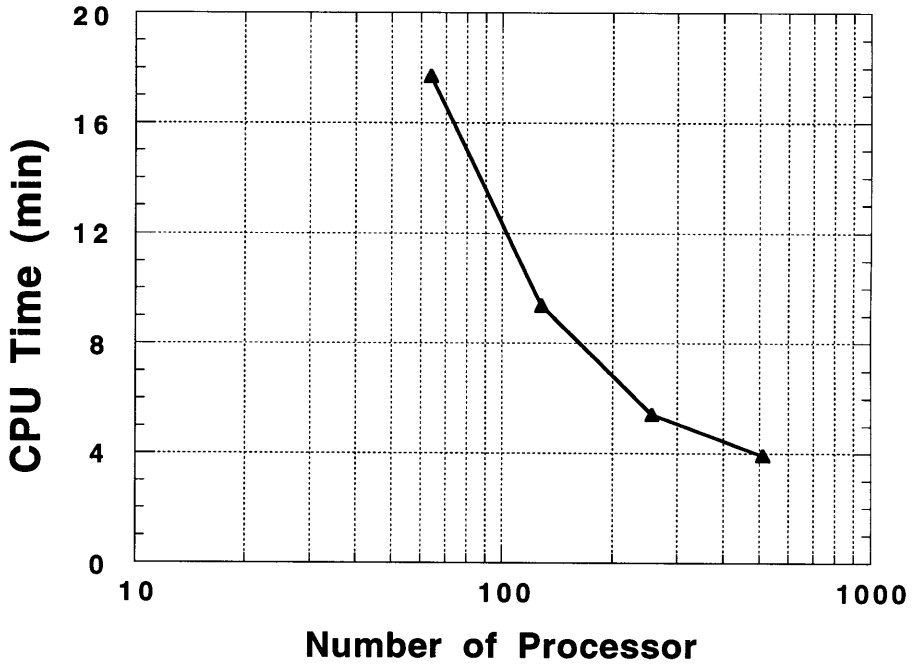

Figure 2-8: CPU time versus number of processors for a 100 time step finite difference calculation on a $100 \times 100 \times 100$ grid.

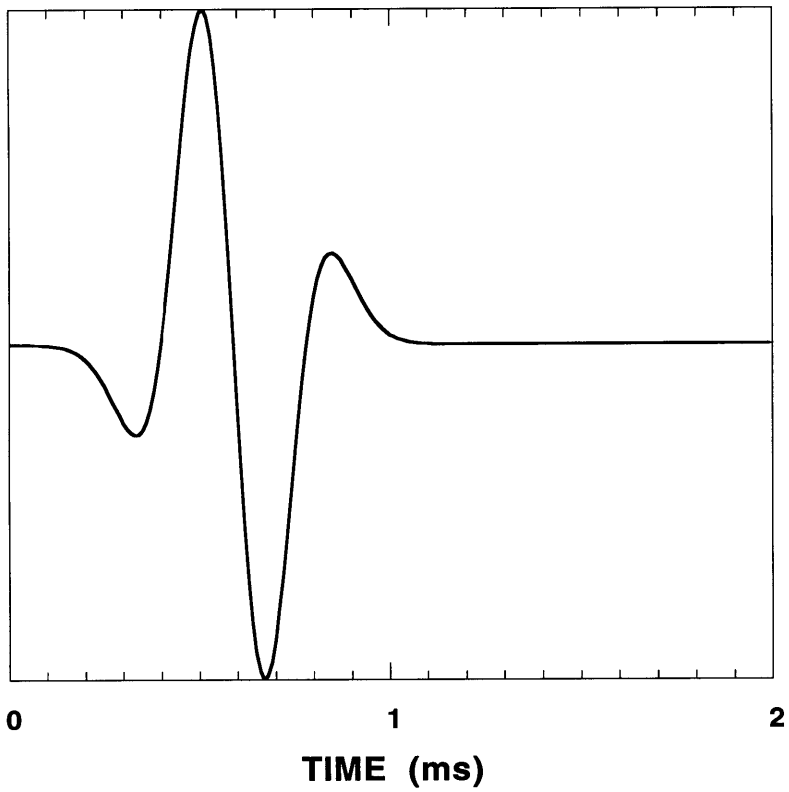

Figure 2-9: Kelly source time function for pressure at the center frequency 2.5 kHz. The scale is arbitrary.

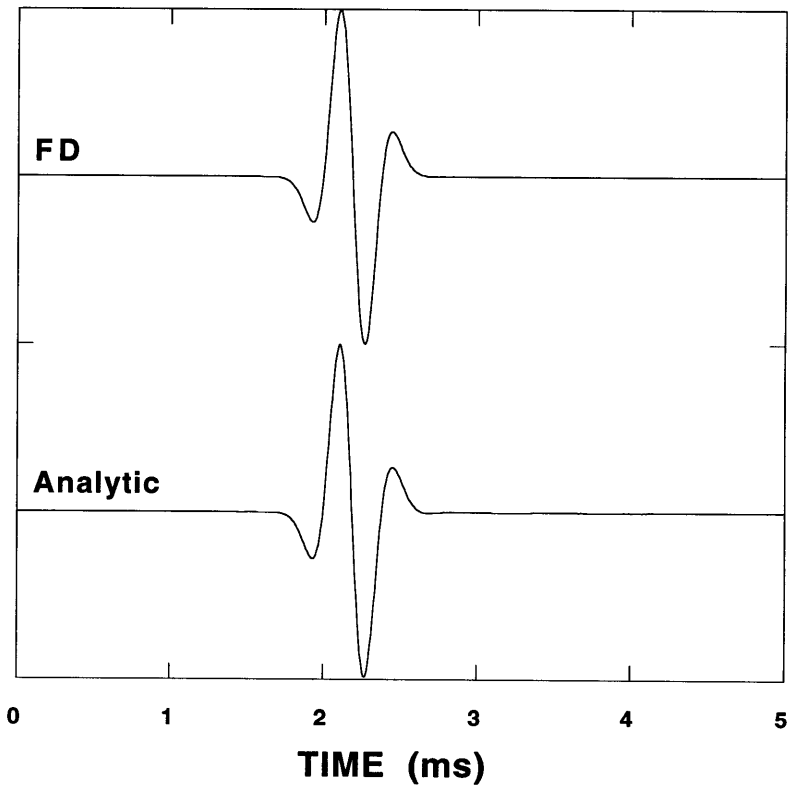

Figure 2-10: Comparison of the finite difference (FD) solution with the analytic solution for the homogeneous acoustic medium. The explosion source at center frequency 2.5 kHz is used. The amplitudes are normalized.

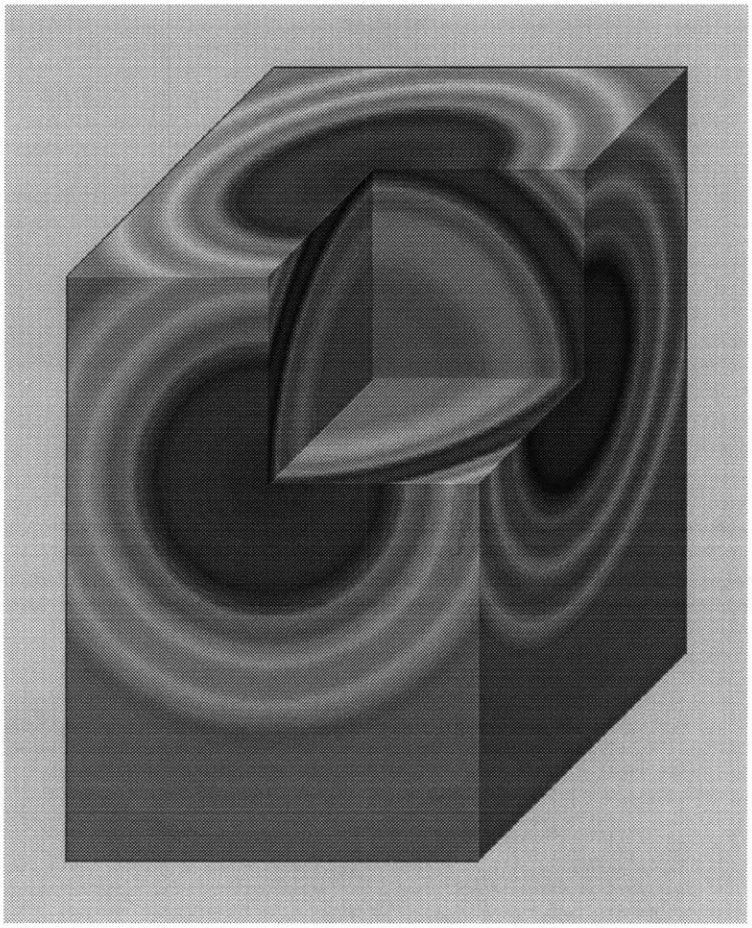

Figure 2-11: Snapshot of the pressure wavefield for the homogeneous acoustic medium at time 1.2 ms. The source center frequency is 2.5 kHz. The image size is $50 \times 50 \times 70$.

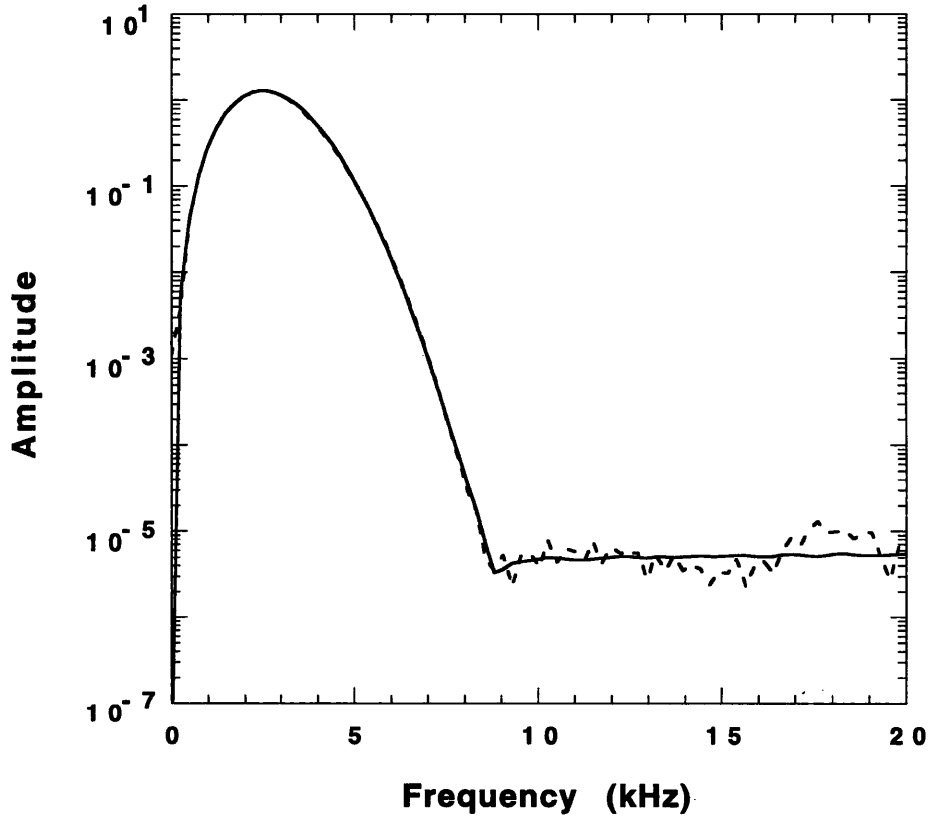

Figure 2-12: Comparison of the finite difference solution (dashed line) with the analytic solution (solid line) for the homogeneous acoustic medium in the frequency domain. The explosion source at center frequency 2.5 kHz is used.

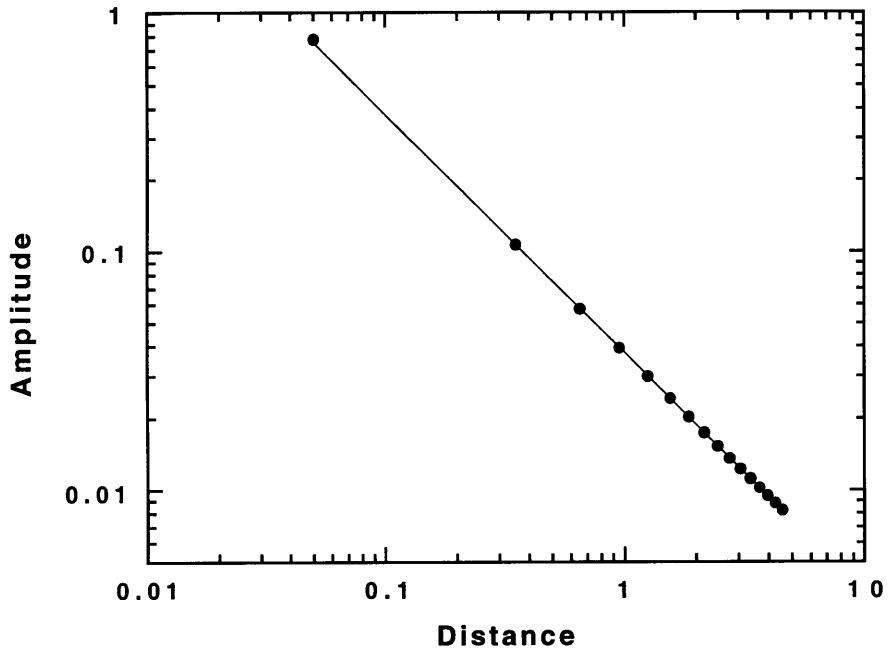

Figure 2-13: The point source implementation in the finite difference scheme (dot) against 1/r (solid line). Distance is normalized by the wavelength.

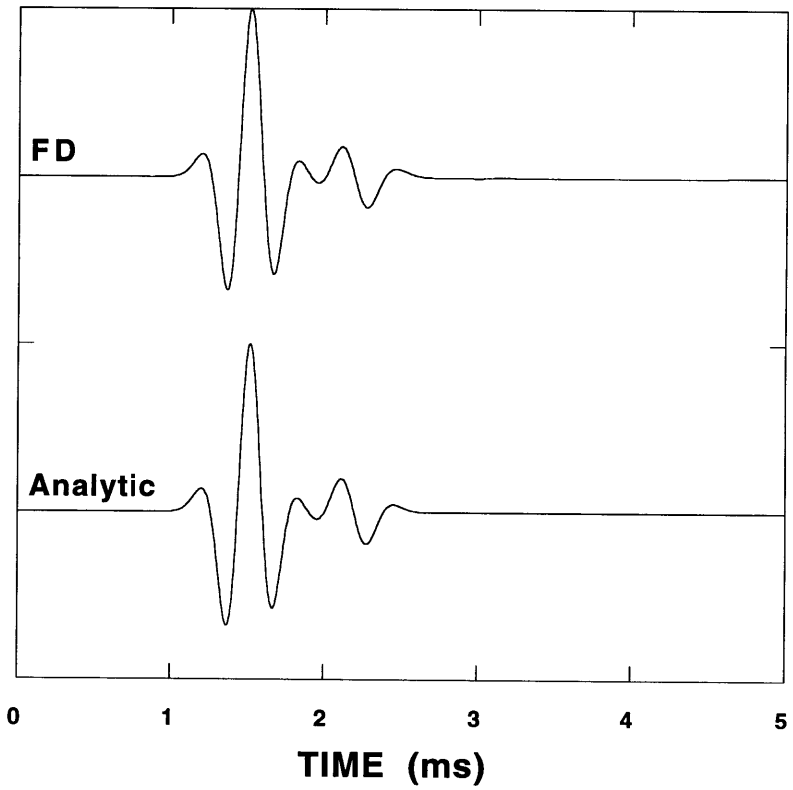

Figure 2-14: Comparison of the finite difference (FD) solution with the analytic solution in the homogeneous elastic medium. The vertical force at the center frequency 2.5 kHz is used. The amplitudes are normalized.

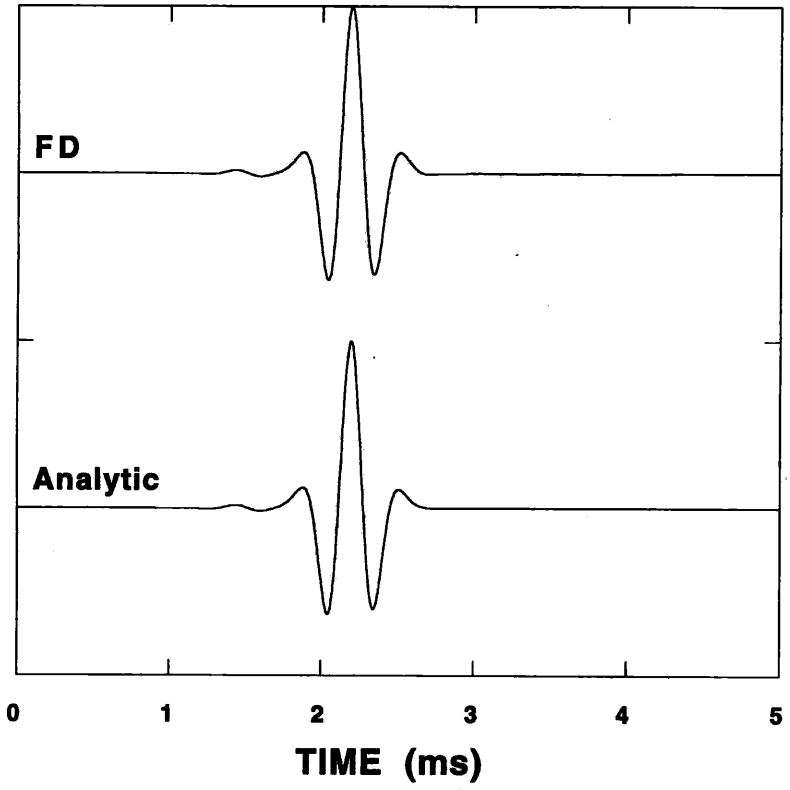

Figure 2-15: Comparison of the finite difference (FD) solution with the analytic solution in the homogeneous elastic medium. The horizontal force at the center frequency 2.5 kHz is used. The amplitudes are normalized.

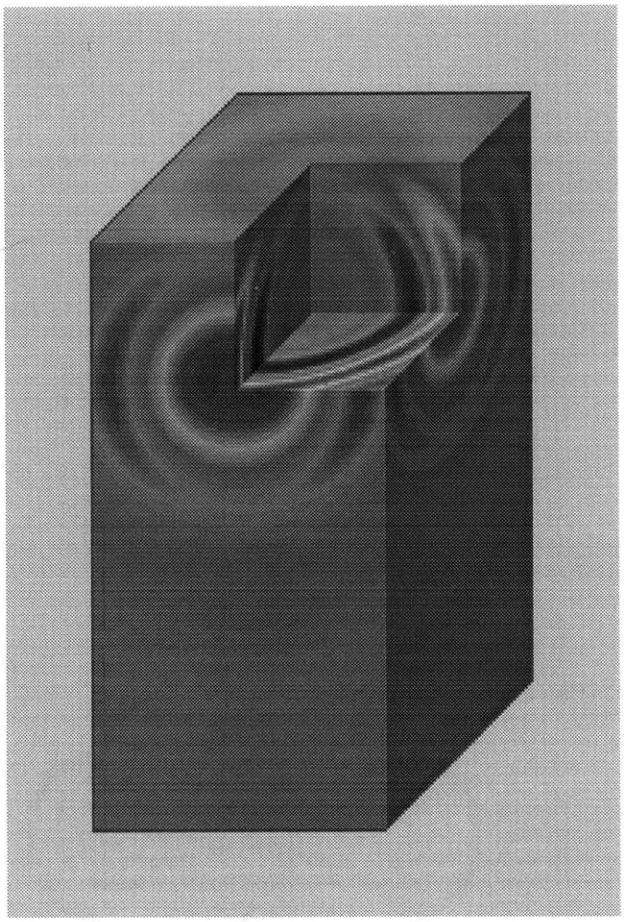

Figure 2-16: Snapshot of the vertical velocity wavefield in a homogeneous elastic medium at time 1.2 ms. The vertical force at center frequency 2.5 kHz is used. The image size is $50 \times 50 \times 100$.

Chapter 3

Applications To Borehole Wave Propagation: Geometry Effect

3.1 Introduction

Understanding wave propagation in a fluid-filled borehole is essential for acoustic logging data processing and interpretation. The first theoretical work to treat the borehole wave propagation problem was done by Biot in 1952. He calculated the borehole guided waves, the pseudo-Rayleigh wave and the Stoneley wave dispersion curves. Peterson (1974) analyzed the borehole wave propagation problem by a complex analysis method. The branch cuts and the poles on the complex plane are directly linked to the refracted P and S waves and the guided waves in the borehole.

A number of papers have been published on the synthetic full-waveform acoustic log (White and Zechman, 1968; Rosenbaum, 1974; Tsang and Rader, 1979; Cheng and Toksöz, 1981; Schoenberg et al., 1981; Paillet and White, 1982; Baker, 1984; Tubman et al., 1984; Schmitt and Bouchon, 1985). The discrete wavenumber technique or a similar one are used to generate the synthetic logs. The centered monopole source (explosion source) and the azimuthal symmetric borehole are considered. Radial layering is allowed. In the early 80's the shear wave logging method was invented to

measure the formation shear wave velocity directly, especially in the soft formation (formation shear wave velocity is less than the borehole fluid velocity). The synthetic dipole log also considered the azimuthal symmetric borehole model (Kurkjian and Chang, 1986; Winbow, 1988; Schmitt, 1988). This method works excellently for the simple borehole model which is vertically homogeneous. This allows for the transformation of the vertical axis into the wavenumber, solves the problem in the wavenumber-frequency domain, and then transforms back to the space-time domain. The wavenumber integration is performed numerically and the frequency integration is done by inverse FFT. The boundary element method, combined with the discrete wavenumber technique, is used to treat the vertically irregular borehole (Bouchon and Schmitt, 1989), or the elliptic borehole (Liu and Randall, 1992).

Bhashvanija (1983) and Stephen et al. (1985) applied the finite difference method to the borehole wave propagation in a 2-D cylindrical coordinate. They solve the wave equation in the displacement form by finite difference. The fluid-solid boundary at the borehole wall is treated explicitly to satisfy the boundary conditions, which are the continuity of the normal displacement, stress, and vanishing of the tangential stress. Kostek (1990) applied staggered grid finite difference to the borehole problem in a cylindrical coordinate. The fluid-solid boundary is not treated explicitly because of the staggered grid. Randall et al. (1991) studied monopole and dipole acoustic logs using the staggered grid in a 2-D cylindrical coordinate. They considered an arbitrary azimuthal mode number in the formulation. Randall (1991) also studied the multipole acoustic log in the nonaxisymmetric borehole using the staggered grid finite difference method. In this case the borehole and the formation are assumed invariant in the axial z direction, which allows spatial Fourier transform. The finite difference is performed on a X-Y Cartesian grid. The above methods can be called a 2.5-D finite difference method (2-D model plus 3-D source). The only true 3-D finite difference method applied to the borehole acoustic logging was done by Yoon and McMechan (1992). They adopt the second-order staggered grid finite difference

scheme.

The reasons for choosing the Cartesian coordinate in this thesis to model the borehole wave propagation instead of the cylindrical coordinate are the following: First, we are interested in the 3-D structure effect on the acoustic log. These models don't possess azimuthal symmetry, so the cylindrical coordinate doesn't have an advantage. Second, on the 3-D cylindrical grid it is very difficult to treat the point of $r = 0$, and the grid size increases as r becomes large. It is hard to control the grid dispersions. Finally, in the next chapter we will consider the borehole wave propagation in an anisotropic formation. The Cartesian coordinate is a generic coordinate to describe the elastic constant tensor.

The differences between this thesis and the work done by Yoon and McMechan (1992) are the following. First, the accuracy of our scheme is fourth-order and theirs is second order. Our scheme includes anisotropy (Chapter 4), a dipole source, a better absorbing boundary condition, and runs on a parallel computer. Second, our staggered grid is arranged differently. In our arrangement the borehole wall is located where the tangential stress vanishes. Finally, in Yoon and McMechan's paper there isn't any comparison with the known solutions. In this thesis we compare our finite difference method with the analytic solutions in the homogeneous acoustic, elastic, and transversely isotropic medium. The finite difference results of the borehole monopole and dipole wave propagation are compared with the discrete wavenumber method. Also the finite difference synthetics of the borehole wave propagation in an orthorhombic formation are compared with the ultrasonic lab measurements (Chapter 4).

In this chapter the fourth-order finite difference method is applied to borehole wave propagation in an isotropic formation. The method is further tested in the borehole environment against the discrete wavenumber method for the monopole and dipole sources. More complicated borehole models are considered next. They are an off-centered source, an elliptic borehole, and layered formation.

3.2 Discrete Wavenumber Method Comparisons

We test the finite difference method for wave propagation in a fluid-filled borehole embedded in an elastic formation in this section. The discrete wavenumber method is a widely used numerical method to compute waveforms in simple borehole geometries (Cheng and Toksöz 1981; Schmitt 1988). The finite difference results are compared with the discrete wavenumber solutions. This test is unlike those done in Chapter 2, where the medium is homogeneous and only body waves are involved. Here the medium is inhomogeneous, borehole wall (fluid-soild interface) is a very sharp boundary, and both body and guided waves are involved.

There are four waves propagating in a fluid-filled borehole embedded in an elastic formation. The two body waves are the refracted P and S waves. They propagate as compressional waves in the fluid, are critically refracted along the borehole wall as compressional and shear waves, and are then refracted back into the fluid as compressional waves. The two guided waves are Stoneley and pseudo-Rayleigh waves. The Stoneley wave has a phase velocity lower than both the formation shear and fluid velocities. Its amplitude decays exponentially on both sides of the fluid-solid boundary. The Stoneley wave is slightly dispersive. The pseudo-Rayleigh wave has phase velocities between the formation shear and fluid velocities. Its amplitude decays exponentially in the formation and is oscillatory in the fluid. The pseudo-Rayleigh wave is highly dispersive and has a cut-off frequency for each mode.

The physical parameters of the borehole fluid and formation are listed in Table 3.1. A grid of $70 \times 70 \times 200$ is used to build the borehole model. The borehole radius is 0.1 m. Because the finite difference grid is in the Cartesian coordinate, the borehole has to be approximated by a rough edged circle. The borehole is numerically drilled along the Z axis.

First the monopole source is considered. The explosion source at center frequency 7 kHz is located on the grid at (35, 35, 40), which is the center of the borehole. The source is away from the $z = 0$ because it is the absorbing boundary. Five pressure

receivers are located along the borehole center. The distance between the source and the first receiver is 0.7 m and the receiver spacing is 0.2 m. The grid size is 1 cm, which is about $\frac{1}{20}$ of the fluid P wavelength at the center frequency. The time step is 0.001 ms. The second-order Higdon's absorbing boundary condition is used to reduce the reflections. The local P and S wave velocities are substituted into Higdon's formula. Inside the borehole two velocities are set to the fluid velocity. The CPU time for 3000 time step calculations is about 4 hours and 16 minutes with 128 processors.

The comparison of the finite difference synthetics with the discrete wavenumber solutions is plotted in Figure 3-1. They agree very well. The mismatch reflects the small error of phase difference between the Stoneley wave and the pseudo-Rayleigh wave, which is caused by the grid dispersion. This comparison demonstrates that the staggered grid scheme handles the sharp fluid-solid boundary very well. It also shows that in the inhomogeneous medium Higdon's absorbing boundary condition successfully absorbs the body waves as well as the guided waves. The snapshot of the wavefield τ_{xx} at time 0.8 ms is plotted in Figure 3-2. Most of the wave energy is trapped inside the borehole due to the hard formation (the fluid velocity is less than the formation shear wave velocity). The wavefield is complicated because there are four different kinds of waves present in the borehole. It is hard to identify these waves clearly on the snapshot.

To further test the finite difference results we keep all the parameters the same, but increase the source center frequency to 14 kHz. This reduces the grid size to $\frac{1}{10}$ of the fluid P wavelength at the center frequency. The comparison of the finite difference synthetics with the discrete wavenumber solutions is plotted in Figure 3-3. Once again the agreement is very good. The fourth-order scheme requires fewer grid points per wavelength to get good results. At this frequency range the seismograms are dominated by the pseudo-Rayleigh wave. So the mismatch shown in the 7 kHz comparison does not appear here.

In the above test we only considered the hard formation. In the soft formation

there are no pseudo-Rayleigh arrivals. The seismograms consist of the leaky P mode and the Stoneley wave. The finite difference and the discrete wavenumber comparison is plotted in Figure 3-4. They are in good agreement. The soft formation parameters are listed in Table 3.1 under the entry "shale". The same grid size and time step as in the previous test are used. The source center frequency is 7 kHz. There are some Stoneley wave amplitude differences between the finite difference synthetics and the discrete wavenumber solutions. The amplitude differences are caused by the discretization of the fluid-solid boundary at the borehole wall. This discretization makes the borehole wall less sharp than it is. So the Stoneley wave amplitudes are slightly small in the finite differenec synthetics.

Next we consider the dipole source. The dipole is implemented through initiation of the velocity on the source grid. A source with center frequency 3 kHz is located at the borehole center. The dipole direction is along the X axis. All other parameters are the same as the monopole calculation. The receiver records the velocity v_x. Comparison of the finite difference results with the discrete wavenumber solutions is shown in Figure 3-5. The two solutions agree reasonably well. The flexural mode is a highly dispersive wave. The flexural wave at different frequency travels with a different velocity. The grid dispersion also depends on the frequency. So the different errors are added at different frequencies. Also, in the Cartesian coordinate the borehole wall is approximated by "stair-like" boundary instead of the circular one. The above two reasons explain the discrepancy of the comparison. The wavefield snapshot at time 1.1 ms is shown in Figure 3-6. In the dipole log the wavefields are dominated by the flexural mode so the snapshot is very easy to understand. The image is slightly processed. The zero value of the field is presented by the grey color. It separates the positive and negative part of the fields. The cycles from the seismograms are also reflected on the image. We can also observe from the image that the source radiates waves, then interacts with the formation and sends the flexural mode down the borehole.

The dipole log was invented to measure the formation shear wave velocity directly in the soft formation. Comparison of the finite difference results with the discrete wavenumber solution in the soft formation is shown in Figure 3-7. The parameters are the same as the soft formation monopole test. The source center frequency is 3 kHz. This comparison is very similar to the hard formation test. The finite difference solution is more dispersive than the discrete wavenumber solution.

The finite difference synthetics of the monopole and dipole logs in the fluid-filled borehole surrounded by the hard and the soft formation agree well with the discrete wavenumber results. The discrepancy can be explained by the grid dispersion and the rough edged circle approximation of the borehole wall.

3.3 Off-centered Source

In the field situations there is no guarantee that the logging tool is always located at the center of the borehole. We have to investigate the off-centered tool effect. Tadeu (1992) and Schmitt (1993) studied the off-centered tool effect by using the discrete wavenumber method. The off-centered source breaks the azimuthal symmetry, even if the borehole and the formation are azimuthally symmetric. This azimuthal dependence has to be included in the wavefield expansion. In the finite difference simulation this is simply done by putting the source and the receiver at the desired positions.

To demonstrate the off-centered source effect, the borehole model in the previous section is used. All parameters are kept the same. The source is moved a half radius (0.5 cm) away from the center of the borehole along the X axis. This is illustrated in Figure 3-8. The receiver positions are still at the center of the borehole. Synthetics obtained from a 7 kHz monopole source are plotted in Figure 3-9. The plot shows the large amplitude Stoneley wave compared with the center source (Figure 3-1). This can be understood by Stoneley wave amplitude distribution. Its amplitude decays exponentially on both sides of the borehole wall. When the source is moved closer to

the borehole wall it will excite Stoneley waves more efficiently.

Off-centered dipole sources are considered next. Figure 3-10 and Figure 3-11 show the waveforms of dipole sources applied along the X and the Y directions, respectively. The source positions are the same as the monopole. Figure 3-10 and Figure 3-11 display the same waveforms as the centered dipole source (Figure 3-5). The differences of these plots are the amplitudes. The maximum amplitudes of the centered dipole, the off-centered dipole in the X direction and in the Y direction are 0.01313, 0.01206 and 0.01041, respectively. This can be explained as follows: in the low frequency range, the dipole source excites the dominant flexural mode. These three source positions are capable of exciting the flexural mode but with different efficiency. The snapshot of the wavefield from the off-centered dipole in the X direction at time 1.1 ms is shown in Figure 3-12. The off-centered source is very clear from the image. Although the image is not exactly as the centered dipole, they share the same characteristics.

In a circular borehole there are two flexural modes, which have the same phase and group velocities. From a mathematical point of view, the two orthogonal modes are needed to form a complete set. A flexural wave in any direction can be obtained by a linear superposition of these two modes. Because these two modes are identical in velocity, off-centered dipole sources with different orientations produce the same waveforms. These two modes degraded into one because of the symmetry of the model. In order to split these two modes we have to break the azimuthal symmetry. This leads us to the next section: the elliptic borehole.

3.4 Elliptic Borehole

Wells drilled in the earth are often noncircular. This can be caused by tectonic stress, or washout in soft or unconsolidated formations. There are a number of studies of the noncirclar borehole wave propagation problem. Ellefsen (1990) applied the

perturbation theory to the normal modes for a slightly irregular borehole. A more complete study of noncircular modes in a fluid-filled borehole was done by Randall (1991). He used the boundary integral method to solve the problem. This method extended to include an external source for the waveform calculations (Liu and Randall, 1992). Randall (1991) also developed the 2.5-D finite difference technique to compute multipole acoustic waveforms in nonaxisymmetric borehole and formations. But the borehole and formation are assumed vertically uniform. The finite difference calculations are performed on the horizontal X-Y plane. In this section the 3-D finite difference technique is applied to compute the monopole and the dipole log in an elliptic borehole.

The elliptic borehole, with the minor radius 10 cm in the X direction and the major radius 20 cm in the Y direction, is embedded in an isotropic formation. The model is illustrated in Figure 3-13. All other parameters are the same as the test borehole model. First the monopole source at the center frequency 7 kHz is applied at the center of the borehole. The pressure receivers are also located at the center of the borehole. The synthetics are plotted in Figure 3-14. The waveforms in the elliptic borehole are very different from the circular borehole with the 10 cm radius (Figure 3-1). It is difficult to tell from the waveforms how ellipticity affects the individual wave type. It is more interesting to investigate the ellipticity effect on the dipole log, because it is dominated by the flexural modes. The waveforms from a 3 kHz dipole source in the X and Y directions are plotted in Figure 3-15 and Figure 3-16, respectively. The receivers record the velocity in the source's direction. The elliptic borehole breaks the azimuthal symmetry. So it splits the two identical flexural modes into odd and even flexural modes with different phase and group velocities (Randall 1991). For the dipole source applied along the major axis (Figure 3-16), a very dispersive, low frequency even flexural mode is obtained. The even flexural mode is sensitive to the major radius. The snapshot of the wavefield image (Figure 3-17) shows the low frequency characteristics very clearly. The wavefield pattern inside of

the borehole also matches the pattern of the even flexural mode given by Randall (1991). For the dipole source applied along the minor axis of ellipse (Figure 3-15), a less dispersive and high frequency odd flexural mode is observed. The odd flexural mode is insensitive to the major radius. The waveforms are similar to the 10 cm circular borehole one (Figure 3-5). The wavefield image is shown in Figure 3-18. The wavefields are directed in the minor axis direction.

3.5 Layering

The crust of the Earth can be approximately described as a stratified medium on the global scale. Locally the geological process tilted these layers or even overturned them. A tilted or even horizontal well can be drilled in a perfectly horizontal layered crust. In this section we consider the wave propagation in a circular fluid-filled borehole surrounded by the layered formation.

3.5.1 Horizontal bed

Horizontal drilling has become common in the oil industry. It is interesting to investigate the borehole wave propagation along the borehole which is drilled parallel to a layer boundary. The geometry of this problem is illustrated in Figure 3-19. The borehole is infinitely long and Figure 3-19 only shows part of it. The physical parameters of Layer 1 and Layer 2 are listed in Table 3.1 under the entries formation and sandstone. This makes the borehole host layer a slow formation.

First we investigate the effect of the tool position. A monopole source at center frequency 10 kHz is used. The source and the receiver separation is 2 m. The seismograms are plotted in Figure 3-20. The detailed part of the seismograms (0 to 1.0 ms) are plotted in Figure 3-21. For the purpose of comparison the seismogram from the centered tool in the borehole without the bed is shown in trace (a). Because the formation is slow, the seismogram is dominated by the leaky P. The small amplitude

Stoneley wave can be seen around 2.2 ms. The seismogram from the centered tool with the bed 20 cm away from the borehole center is shown in trace (b). We observe an arrival before the leaky P (Figure 3-21 (b)). It is the refracted P from the bed boundary, because the velocity of Layer 1 is faster than Layer 2. This refracted P provides one way to detect the bed near the borehole from the acoustic logging. The 2D slice of the 3D wavefield clearly demonstrates the refracted P from the bed boundary (Figure 3-22). The seismograms from the off-centered tool are plotted in trace (c) for the half radius (5 cm) away from the bed and (d) for the half radius close to the bed. The waveforms in the trace (c) and (d) are very different from the centered tool. The amplitudes are reduced. When the tool is close to the bed, the refracted P waves move forward, and when the tool moves away from the bed, the refracted P waves move back. Also the off-centered tool generates a relatively strong Stoneley wave.

Next we investigate the effect of the distance between the borehole center and the bed. The seismograms are plotted in Figure 3-23. The detailed part of the seisgrams (0 to 1.0 ms) are plotted in Figure 3-24. The tool is centered inside the borehole. Trace (a) is the one without the bed. Trace (b), (c) and (d) are for the bed away from the borehole center at 10, 20 and 30 cm, respectively. When the bed is tangential to the borehole wall, the waveform is very different and the amplitue is much smaller (Figure 3-23 (b)). When the bed is moving away from the borehole, the refracted P wave also moves back (Figure 3-24). This suggests that to detect the structure far away from the borehole the long spacing tool is needed.

Finally, we consider the dipole log. In the dipole log case the properties of Layer 1 and Layer 2 are exchanged. First the dipole source is directed towards the bed. The waveforms are shown in Figure 3-25. The horizontal bed changed the waveforms dramatically. The amplitude at offset 1.1 m is reduced significantly. This is the shear wave interference caused by the layer boundary. But when the dipole source is directed parallel to the bed (Figure 3-26), the synthetics are almost the same as the

one without the bed. This demonstrates that the dipole is a directional source. It only sensitizes to a structure which is in the source's direction.

The wavefield snapshot from the dipole, which is toward the bed, at time 1.1 ms is plotted in Figure 3-27. The image is rotated 90 degrees vertically. The borehole wall and the bed boundary can be clearly seen from the snapshot. Because the velocity in Layer 1 is slower than the borehole host layer the wavefronts fall back in Layer 1. The wavefield snapshot from the dipole, which is parallel to the bed, is shown in Figure 3-28. The layer boundary is not very clearly divided from the image, but that the shear wave in Layer 1 is slower than Layer 2 can still be observed.

3.5.2 Tilted layers

In logging practice it is also common to encounter the tilted layer. A fluid-filled borehole penetrating a tilted layer formation is considered. The model is illustrated in Figure 3-29. The layer boundary intercepts the borehole axis at an angle of 45 degrees. The strike of the layer boundary is parallel to the Y axis. Layer 1 and Layer 2 have the same physical properties as the horizontal bed dipole examples. The borehole radius is 0.1 m. The grid size is 0.01 m and the time step size is 0.001 ms. The whole 3-D grid is $70 \times 70 \times 300$. The source is located at the grid point (35, 35, 40). The layer boundary crosses the borehole center at the grid point (35, 35, 200). The receivers are located at the borehole center. The distance of the source and the first receiver is 0.7 m. The receiver spacing is 0.2 m. The layer boundary cross point is at offset 1.6 m.

The synthetic monopole waveforms are plotted in Figure 3-30. For the purpose of comparison the synthetics from the horizontal layered formation are shown in Figure 3-31. In the horizontal layered case, the boundary also crosses the borehole center at the grid point (35, 35, 200). The plots demonstrate that the horizontal layered boundary generates a stronger reflection and transmission than the 45 degree tilted boundary. The tilted boundary represents the smooth change of the formation

properties. So it reduces the reflection and drives more energy away from the borehole to the formation. The tilted boundary also helped the S wave to the P wave conversion at the boundary (Figure 3-30), which is the small first arrival on the seismograms at offset 1.9 to 2.5 m. But this conversion is not shown in the horizontal boundary case. The different incident angles, zero degree at the horizontal boundary and 45 degrees at the tilted boundary, explain the occurrence or absence of these conversions.

In the dipole log, the synthetics of the dipole, which is parallel to the boundary strike (Y axis), are plotted in Figure 3-32. The synthetics of the dipole, which is perpendicular to the boundary strike, are plotted in Figure 3-33. The dipole synthetics in the borehole near the horizontal layer boundary are shown in Figure 3-34. In the horizontal layer case the transmitted flexural wave in Layer 2 is very clear. The transmitted flexural wave in Layer 2 reflects the fact that the shear wave velocity in Layer 2 is slower than in Layer 1. Transmitted flexural waves across the 45 degree tilted boundary have only about half the amplitude of the one transmitted across the horizontal boundary. There is no clear reflected flexural wave from both boundaries. The 2-D slice wavefield from the dipole in the borehole near the horizontal layer boundary is shown in Figure 3-35. The flexural wave transmitted through the boundary can be seen (the last cycle). The wavefronts are still flat. The 2-D slice wavefield from the dipole in the borehole near the 45 degree tilted layer boundary is shown in Figure 3-36. The flexural wave transmitted through the boundary can also be seen (the last cycle), but the wavefronts become tilted about 45 degrees.

3.6 Conclusion

In this chapter a 3-D finite difference method is applied to the borehole wave propagation in an isotropic formation. The finite difference synthetics of the monopole and the dipole log in a fluid-filled borehole are compared with the discrete wavenumber method. They agree well. Both the hard and the soft formation cases are tested.

This demonstrates that the staggered grid scheme handles the fluid-solid boundary very well. Higdon's second-order absorbing boundary condition works well in the inhomogeneous boundary. It not only can absorb the body waves but also the guided waves.

The off-centered dipole sources in both X and Y directions generate the same waveforms as the centered dipole. The amplitudes are slightly different. The Stoneley wave amplitude is larger from the off-centered monopole than from the centered one.

In the elliptic borehole, two flexural modes are split. The dipole source, directed along the minor axis, excites the odd flexural mode, which is insensitive to the major radius. The dipole source, directed along the major axis, excites the even flexural mode, which is low frequency and dispersive.

In a horizontal well near a horizontal bed, when the dipole source is parallel to the horizontal bed, there is little effect of the bed on the waveform and when the dipole is toward the bed, there is a strong shear wave interference. The amplitudes vary strongly with the offsets. The refracted P waves from the bed boundary can be used to detect the bed, but this refracted P wave is affected by the tool positions in the borehole and the distance between the borehole and the bed. In the borehole, near the 45 degree tilted layer boundary, the monopole log has less reflection and transmission than at the horizontal boundary. The dipole log, too, has less transmission than at the horizontal boundary. There is no clear reflected flexural mode from the tilted and horizontal layer boundary.

	P wave velocity (m/s)	S wave velocity (m/s)	Density (g/c.c.)
Borehole Fluid	1500	—	1.0
Formation	4000	2300	2.3
Sandstone	2770	1100	2.16
Shale	2000	1150	1.6

Table 3.1: Borehole model parameters

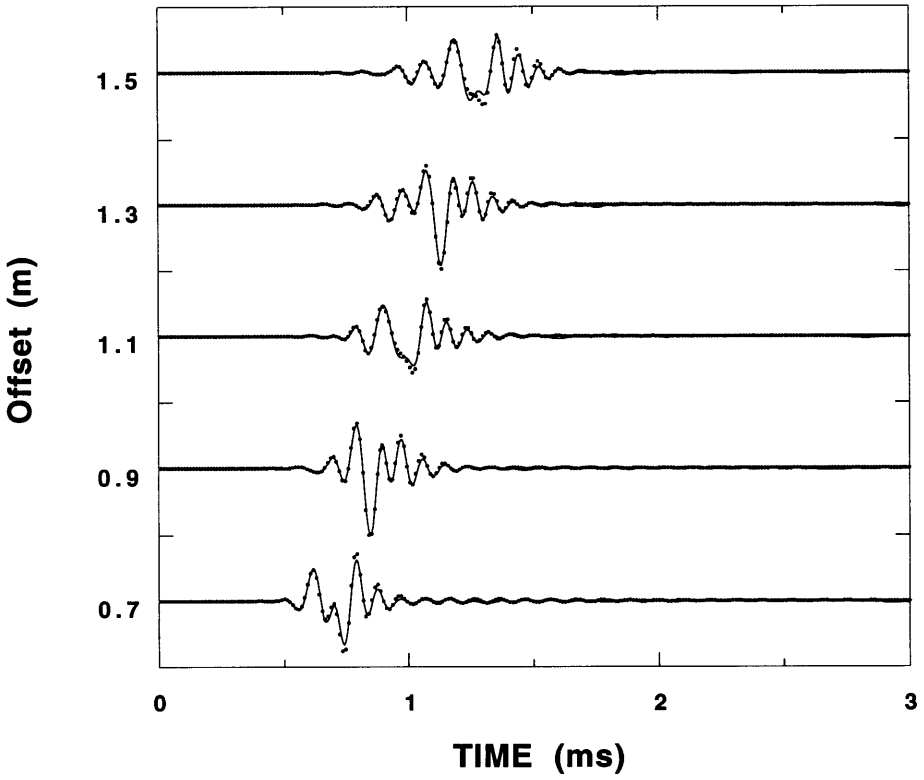

Figure 3-1: Comparison of the finite difference solutions (solid line) with the discrete wavenumber solutions (dot) in a fluid-filled borehole. The monopole source at center frequency 7.0 kHz is used. The amplitudes are normalized.

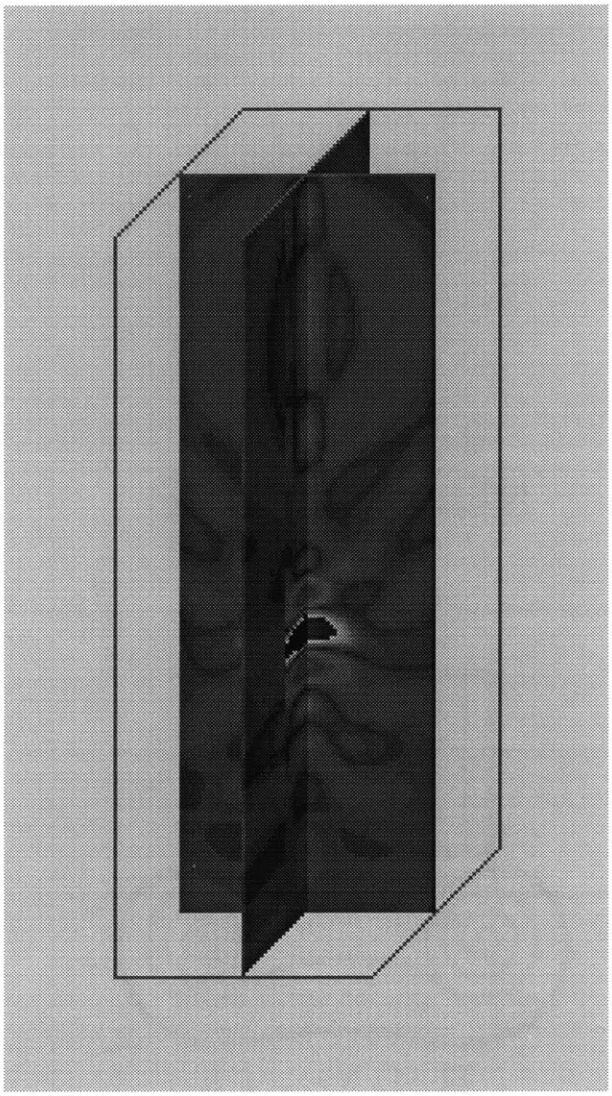

Figure 3-2: Snapshot of the stress τ_{xx} field at time 0.8 ms. The monopole source in a fluid-filled borehole. Source center frequency is 7.0 kHz. The image size is $70 \times 70 \times 200$.

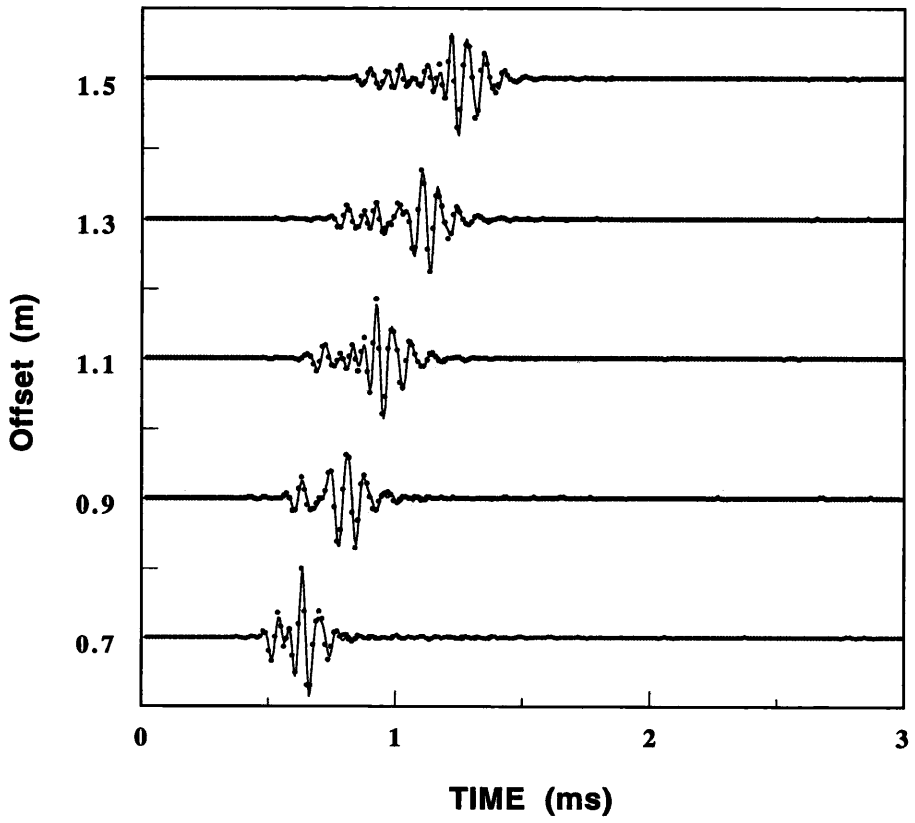

Figure 3-3: Comparison of the finite difference solutions (solid line) with the discrete wavenumber solutions (dot) in a fluid-filled borehole. The monopole source at center frequency 14 kHz is used. The amplitudes are normalized.

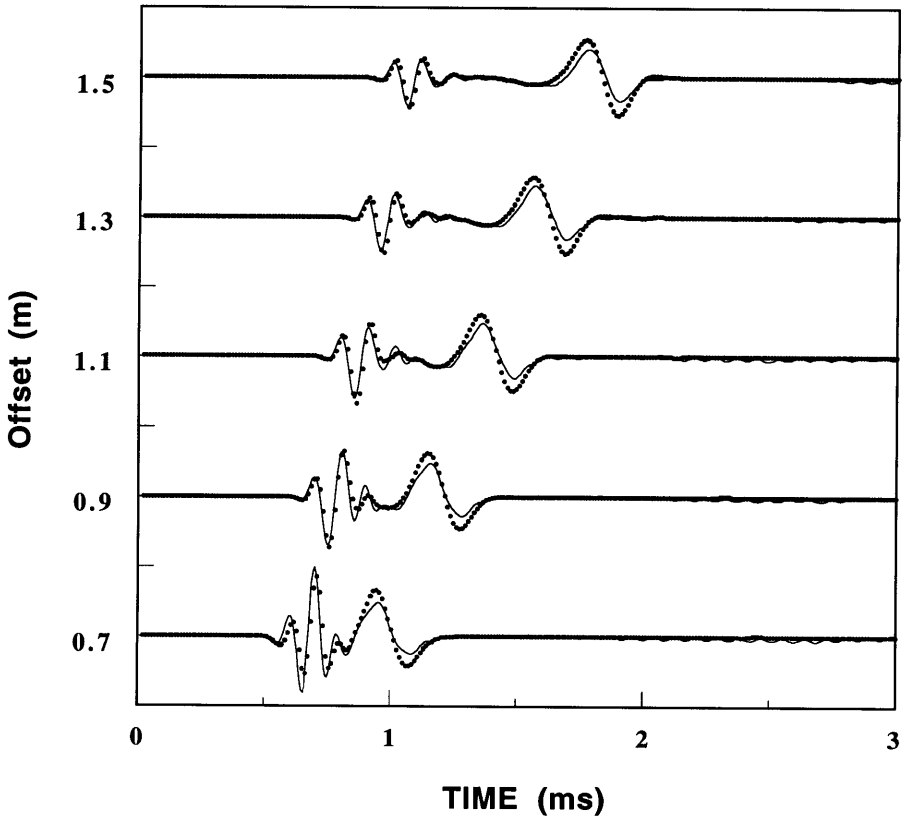

Figure 3-4: Comparison of the finite difference solutions (solid line) with the discrete wavenumber solutions (dot) in a fluid-filled borehole with soft formation. The monopole source at center frequency 7.0 kHz is used. The amplitudes are normalized.

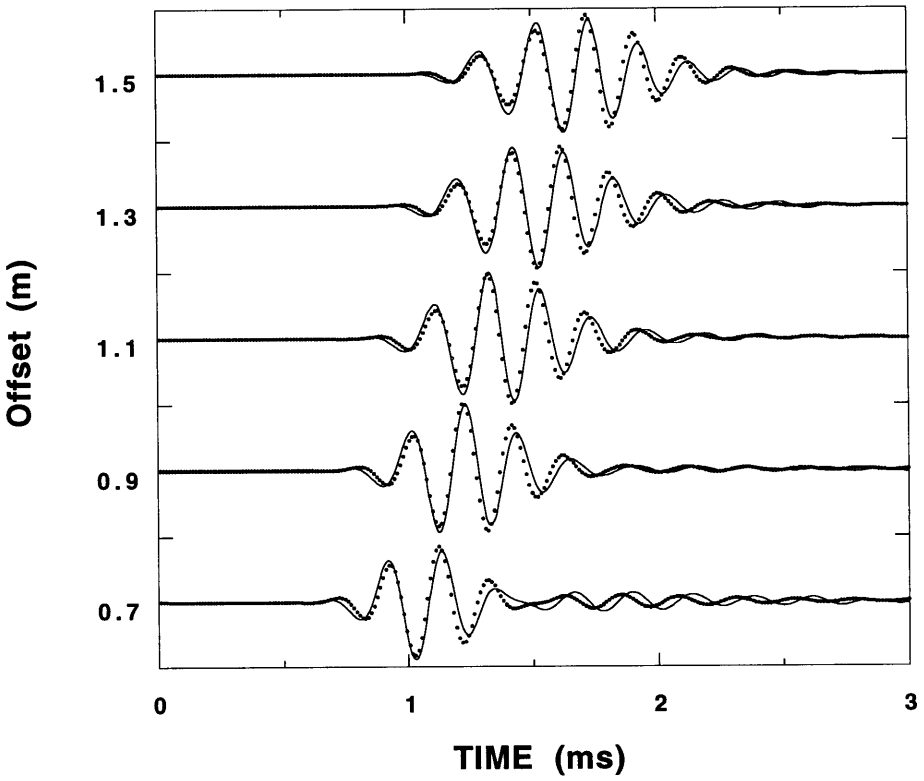

Figure 3-5: Comparison of the finite difference solutions (solid line) with the discrete wavenumber solutions (dot) in a fluid-filled borehole. The dipole source at center frequency 3.0 kHz is used. The amplitudes are normalized.

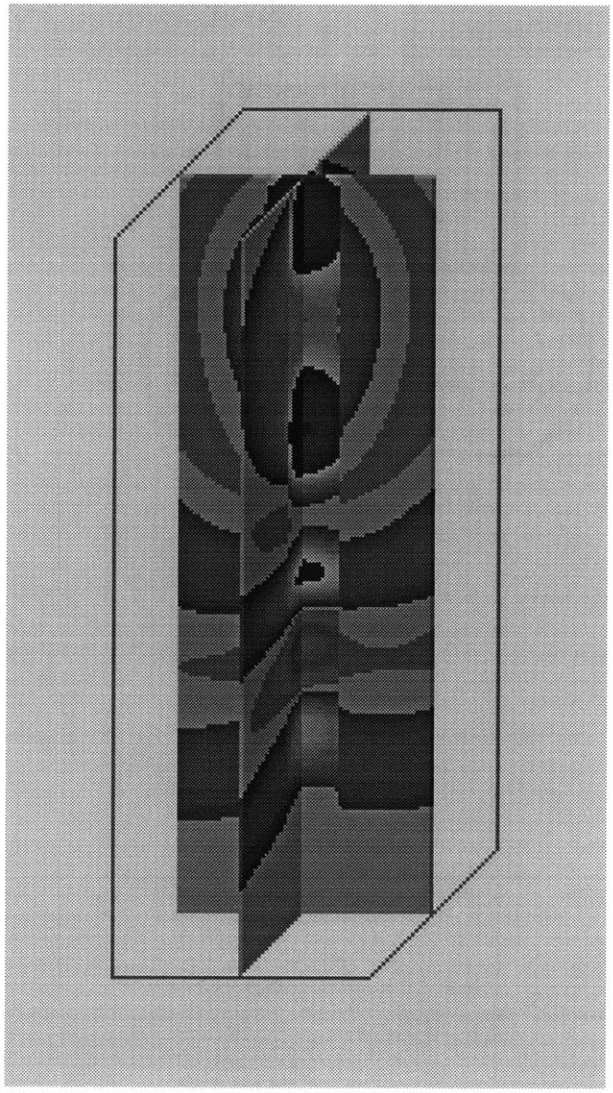

Figure 3-6: Snapshot of the velocity v_x field at time 1.1 ms. The dipole source in a fluid-filled borehole. Source center frequency is 3.0 kHz. The image size is $70 \times 70 \times 200$.

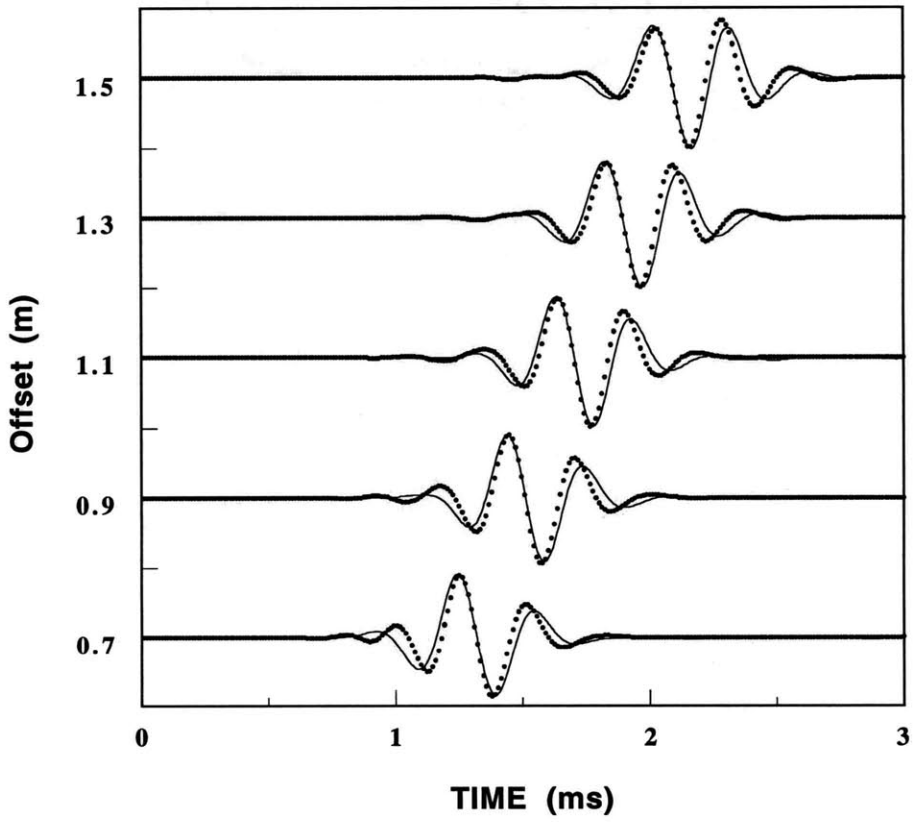

Figure 3-7: Comparison of the finite difference solutions (solid line) with the discrete wavenumber solutions (dot) in a fluid-filled borehole with the soft formation. The dipole source at center frequency 3.0 kHz is used. The amplitudes are normalized.

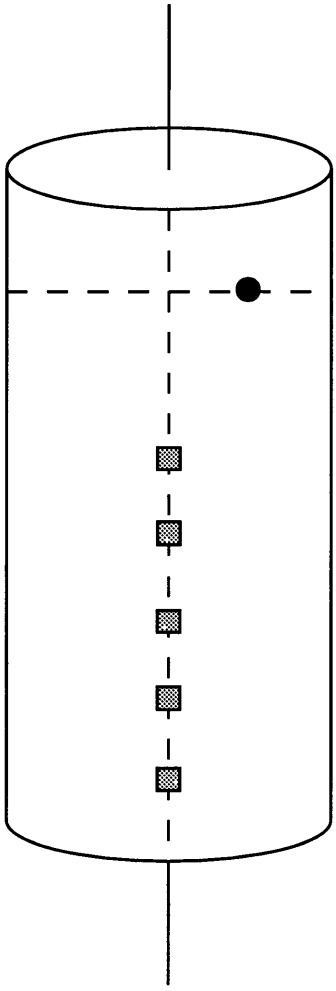

Figure 3-8: Geometry of off-centered source in the borehole. The source (solid circle) and receivers (shaded square) are also shown.

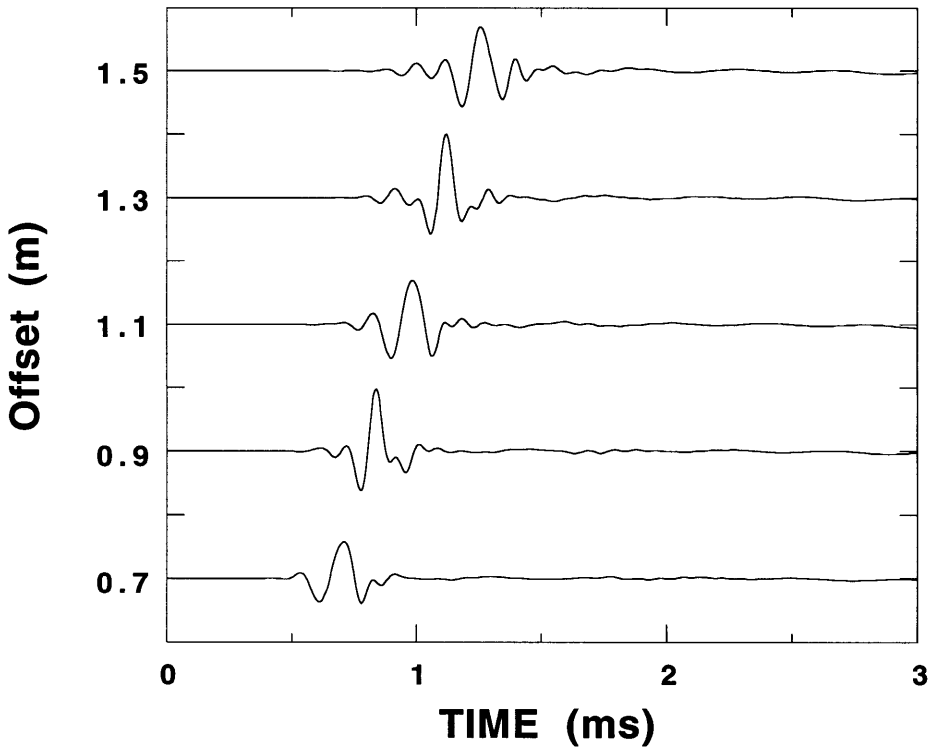

Figure 3-9: Seismograms from the off-centered monopole source. Source center frequency is 7 kHz. Waveforms are the pressure.

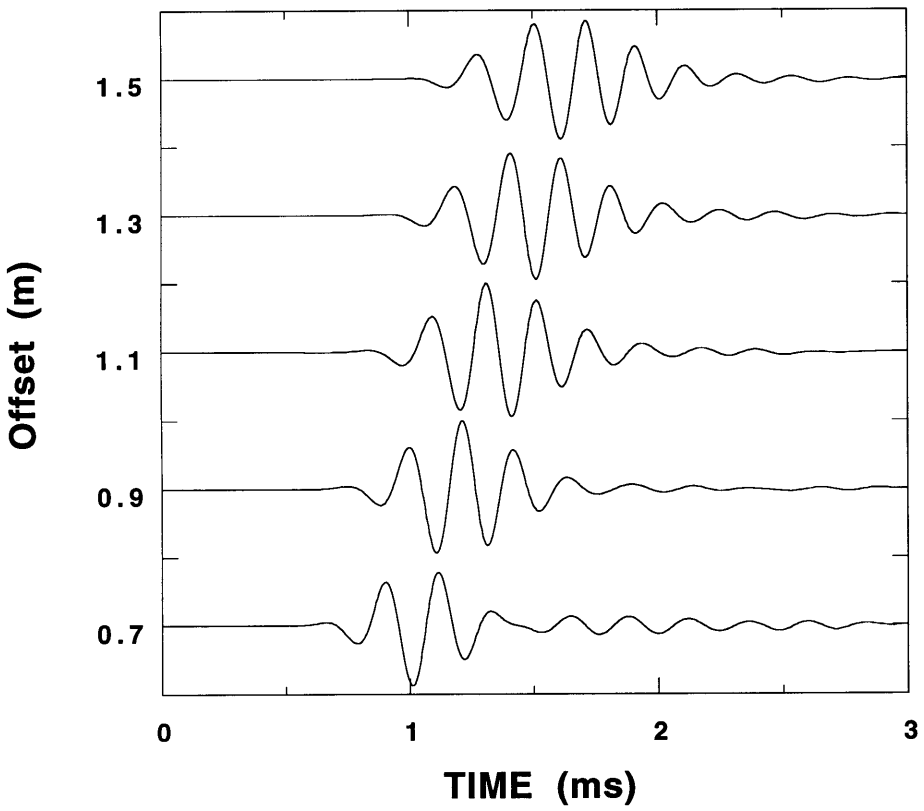

Figure 3-10: Seismograms from the off-centered dipole source in X direction. Source center frequency is 3 kHz. Waveforms are the velocity v_x.

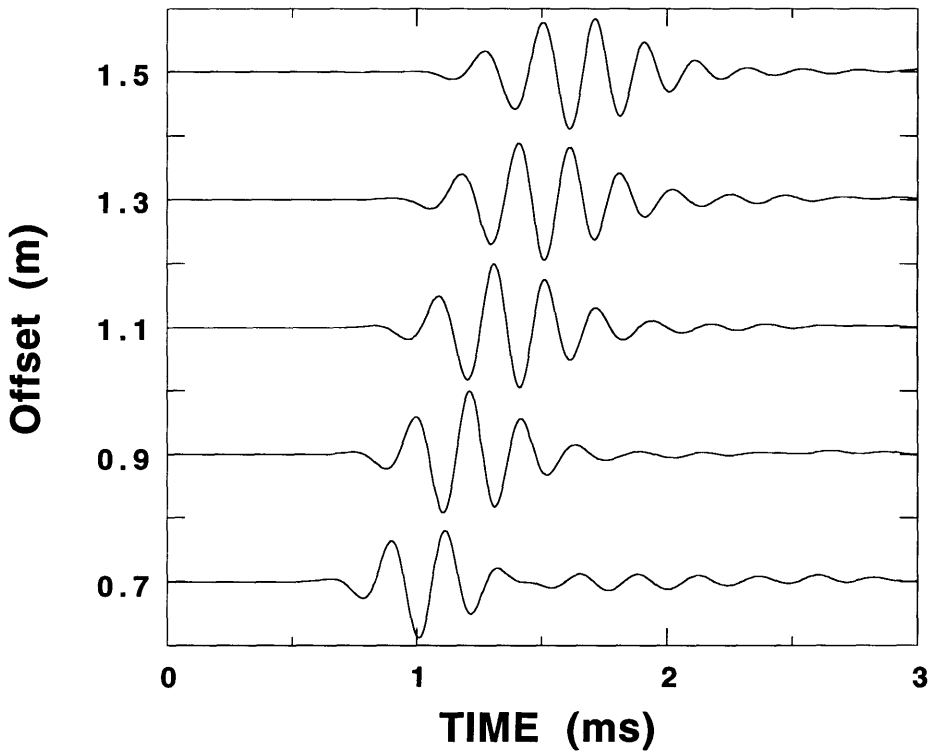

Figure 3-11: Seismograms from the off-centered dipole source in Y direction. Source center frequency is 3 kHz. Waveforms are the velocity v_y.

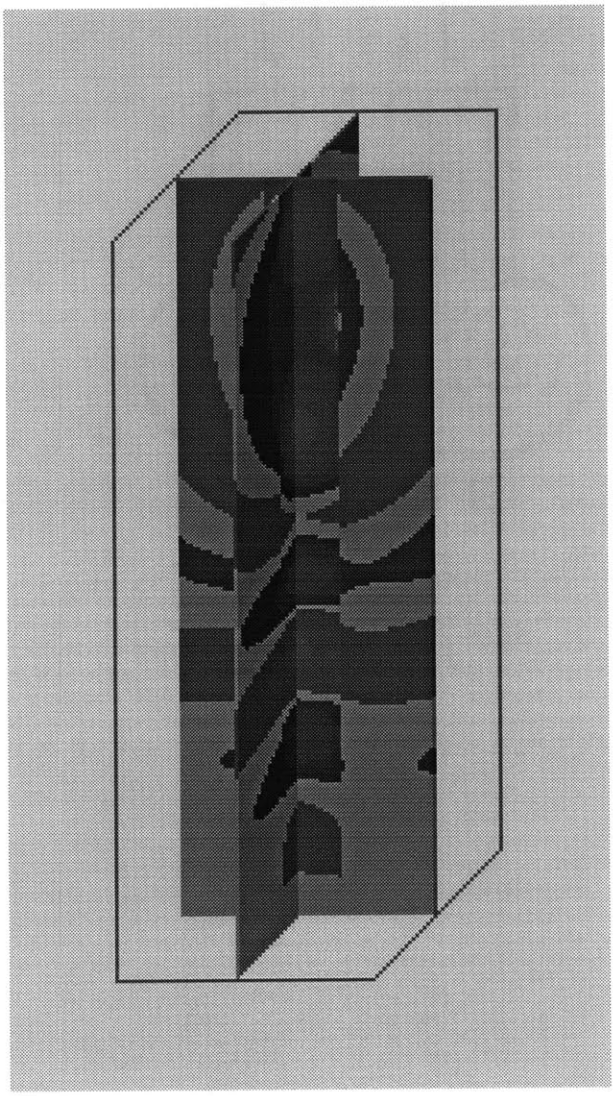

Figure 3-12: Snapshot of the velocity v_x field at time 1.1 ms. The off-centered dipole source is in X direction. Source center frequency is 3.0 kHz. The image size is $70 \times 70 \times 200$.

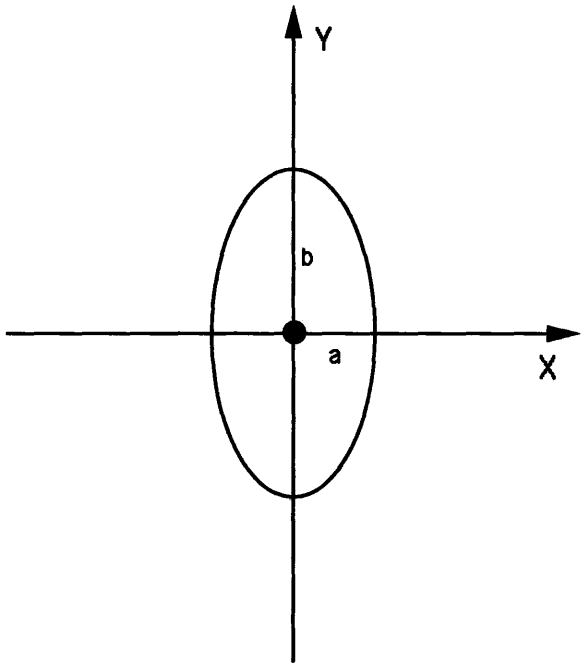

Figure 3-13: Geometry of the elliptic borehole. It is assumed $b = 2a$. The source (solid circle) is located at the center of the borehole

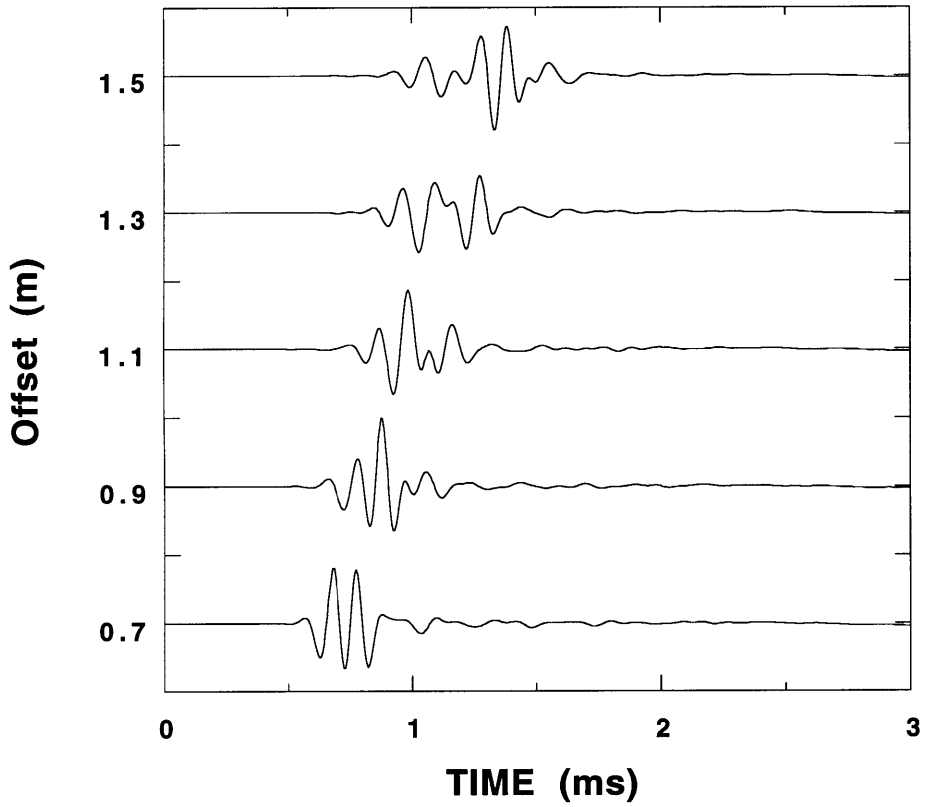

Figure 3-14: Seismograms of the monopole source in the elliptic borehole. The source center frequency is 7 kHz. Waveforms are the pressure at the borehole center.

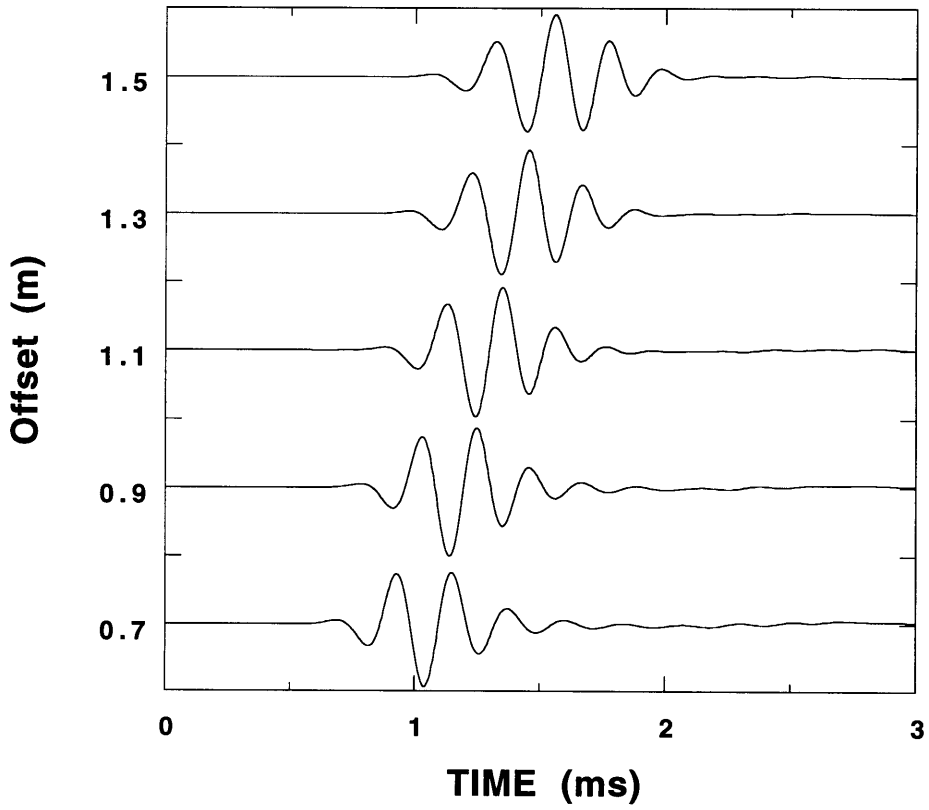

Figure 3-15: Seismograms of the dipole source along the minor axis in the elliptic borehole. Source center frequency is 3 kHz. Waveforms are the velocity v_x.

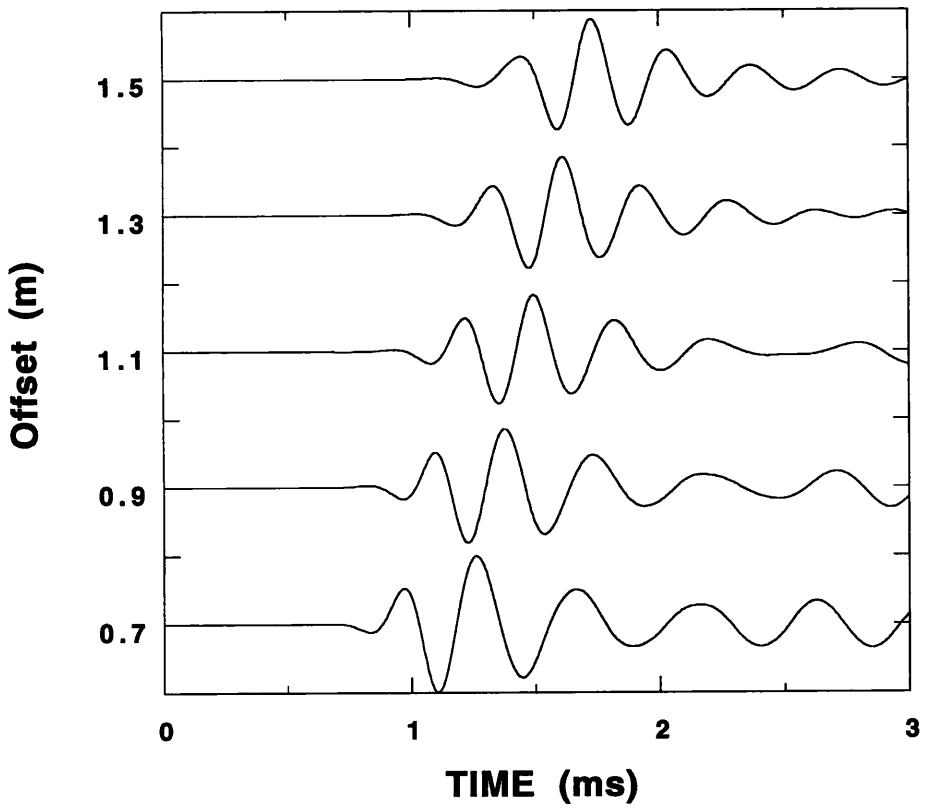

Figure 3-16: Seismograms of the dipole source along the major axis in the elliptic borehole. Source center frequency is 3 kHz. Waveforms are the velocity v_y.

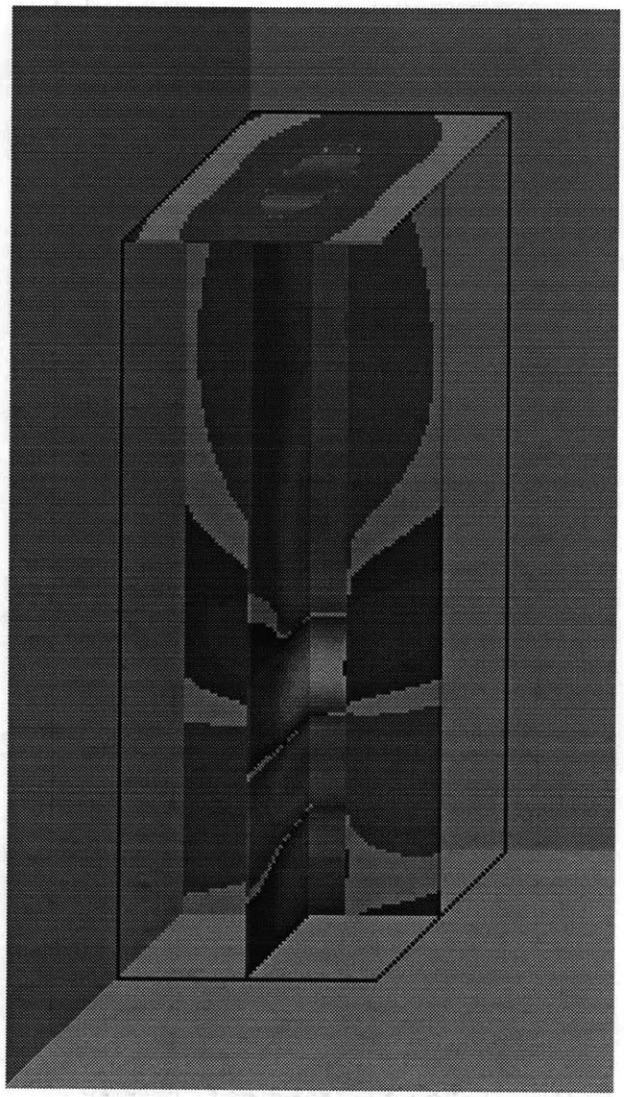

Figure 3-17: Snapshot of the velocity v_y field at time 1.1 ms. The dipole source is along the major axis. The source center frequency is 3.0 kHz. The image size is $70 \times 70 \times 200$.

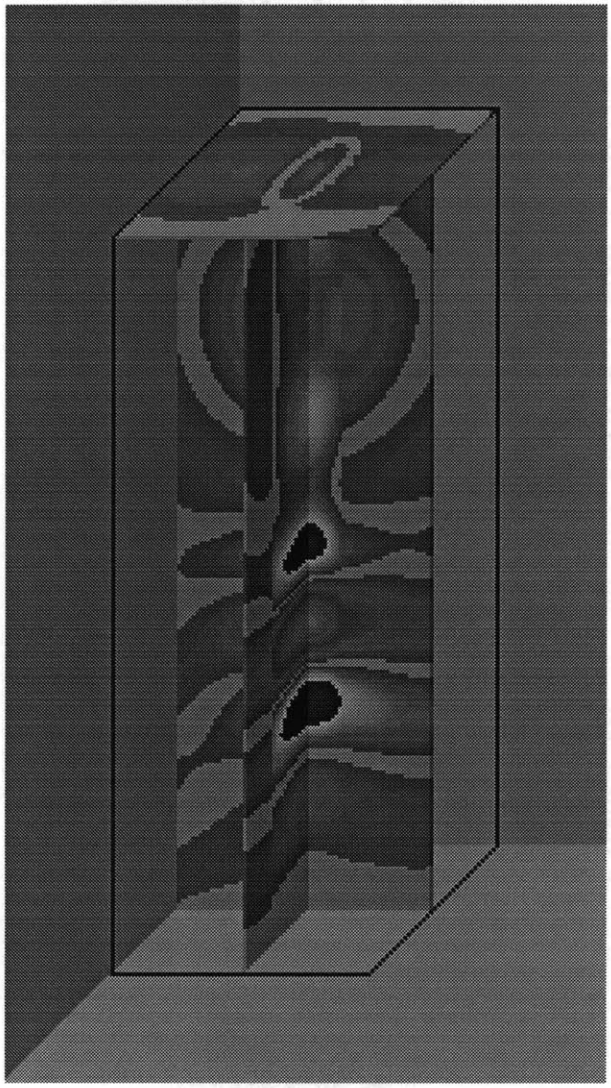

Figure 3-18: Snapshot of the velocity v_x field at time 1.1 ms. The dipole source is along the minor axis. The source center frequency is 3.0 kHz. The image size is $70 \times 70 \times 200$.

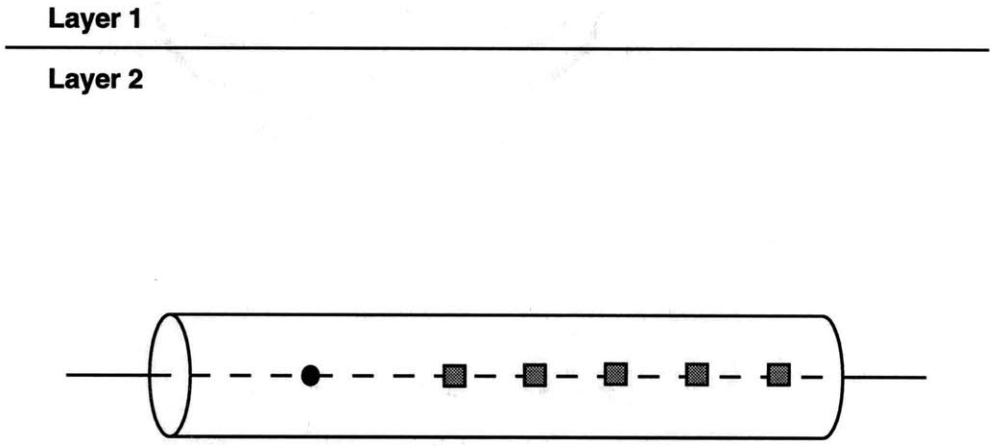

Figure 3-19: Geometry of the borehole near a horizontal bed. The source (solid circle) and receivers (shaded square) are also shown.

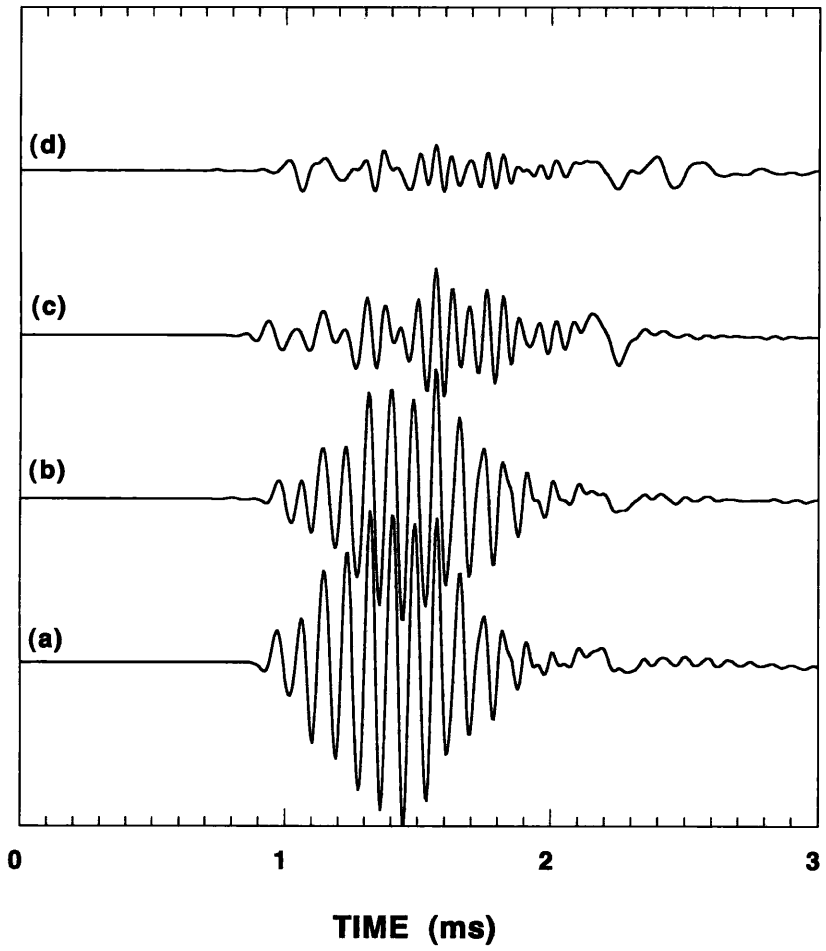

Figure 3-20: Seismograms from the borehole near the horizontal bed. Monopole source of center frequency 10 kHz is used. The source and the receiver separation is 2 m. (a) center tool and no horizontal bed. (b) center tool with horizontal bed. (c) off-centered tool away from the bed by the half borehole radius. (d) off-centered tool close to the bed by the half borehole radius.

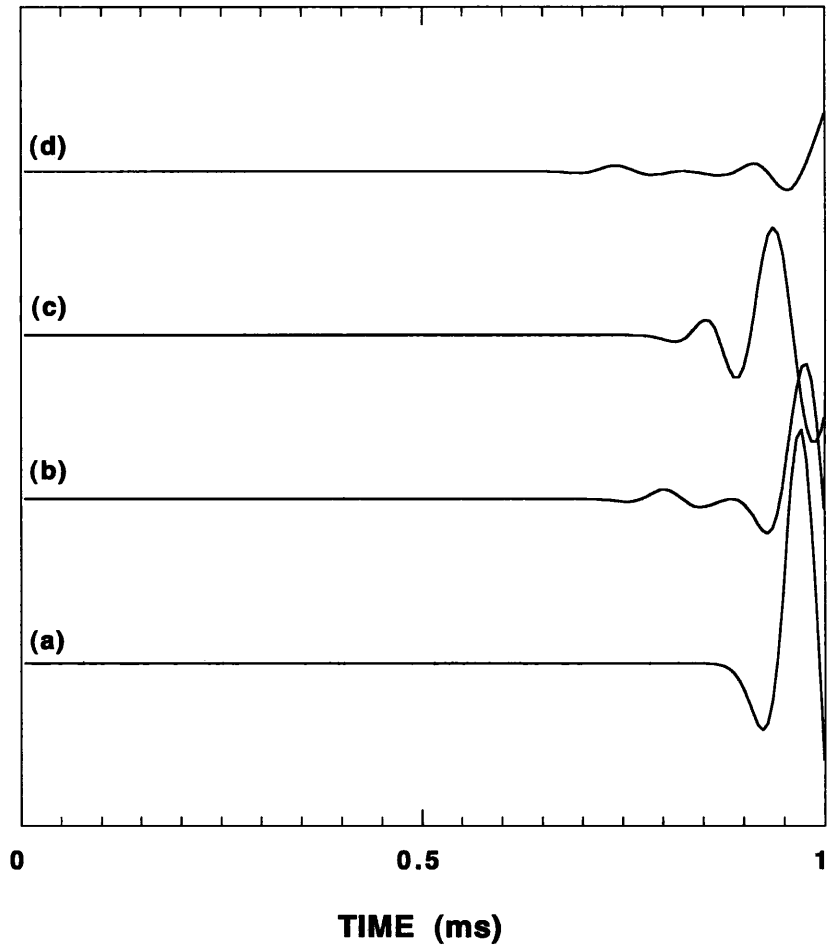

Figure 3-21: Seismograms from the borehole near the horizontal bed. It shows the 0 to 1.0 ms part of the previous figure.

Figure 3-22: 2-D slice of stress τ_{xx} from the borehole near the horizontal bed at time 0.5 ms. The monopole source of center frequency 10 kHz is used. The image size is 80×320.

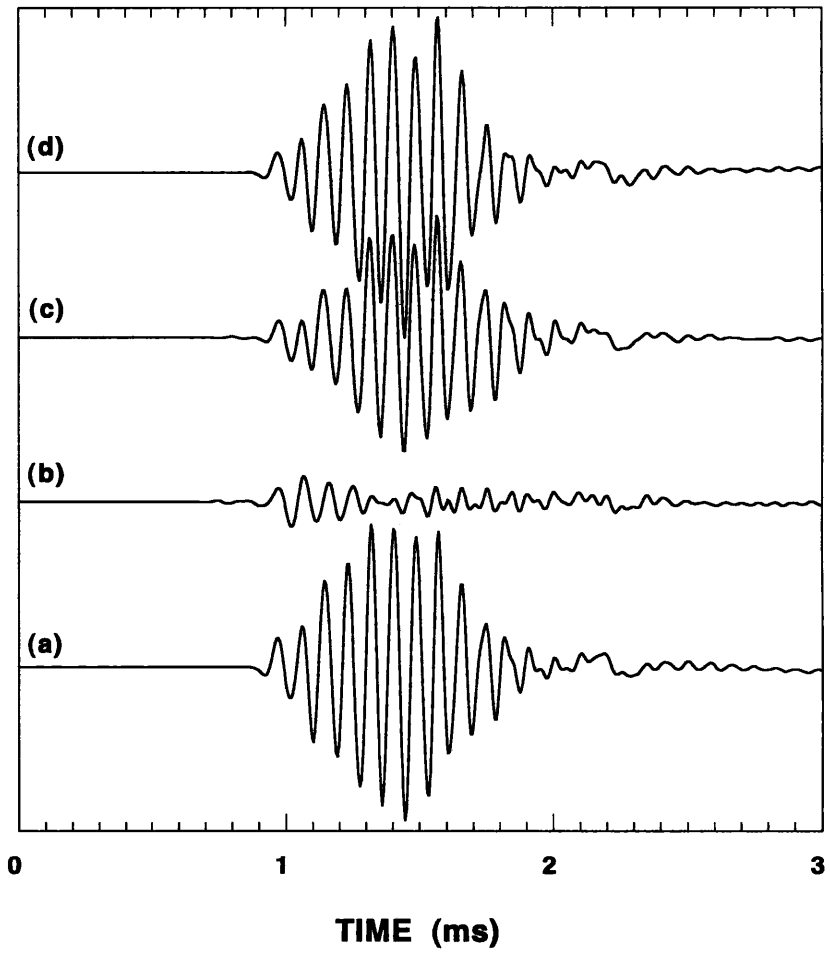

Figure 3-23: Seismograms from the borehole near the horizontal bed. Monopole source of center frequency 10 kHz is used. The source and the receiver separation is 2 m. The tool is centered. (a) no bed. (b) bed 10 cm away from the borehole center. (c) bed 20 cm away from the borehole center. (d) bed 30 cm away from the borehole center.

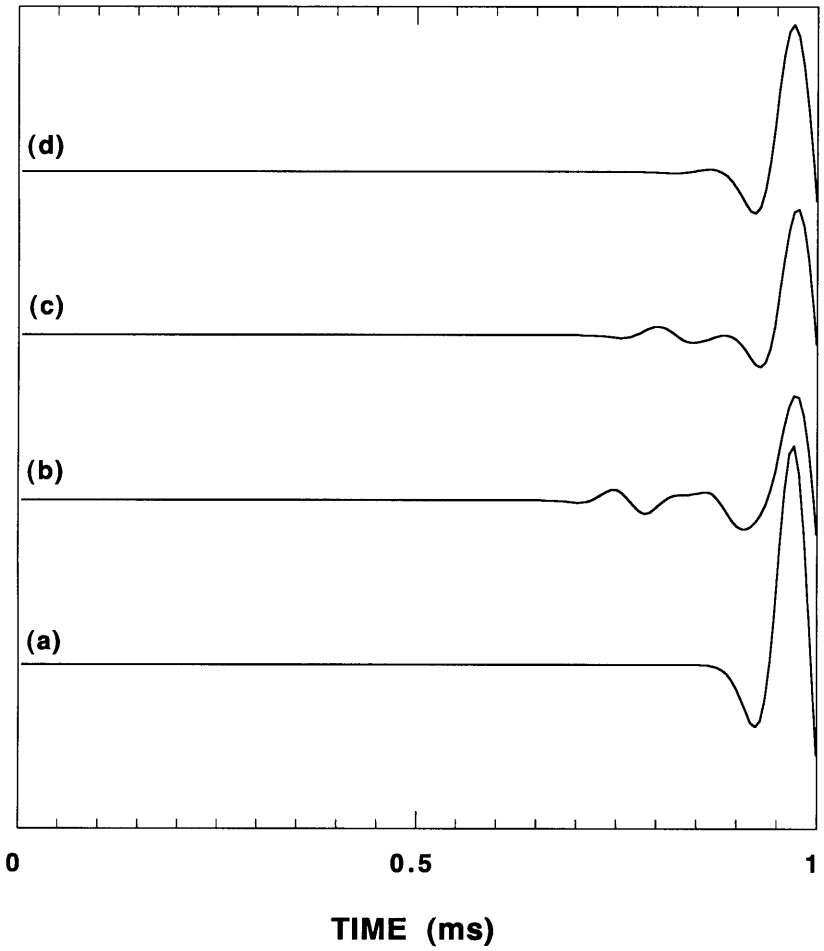

Figure 3-24: Seismograms from the borehole near the horizontal bed. It shows the 0 to 1.0 ms part of the previous figure.

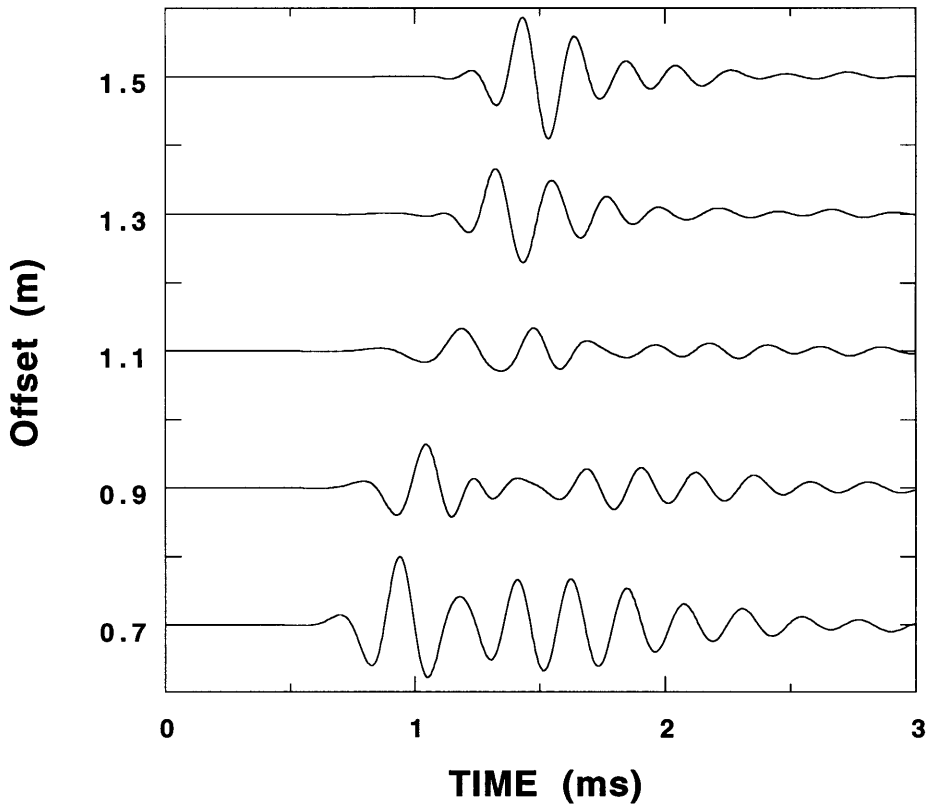

Figure 3-25: Seismograms from the borehole near the horizontal bed. Dipole source is toward the bed and the center frequency is 3 kHz. Waveforms are the velocity v_x at the borehole center.

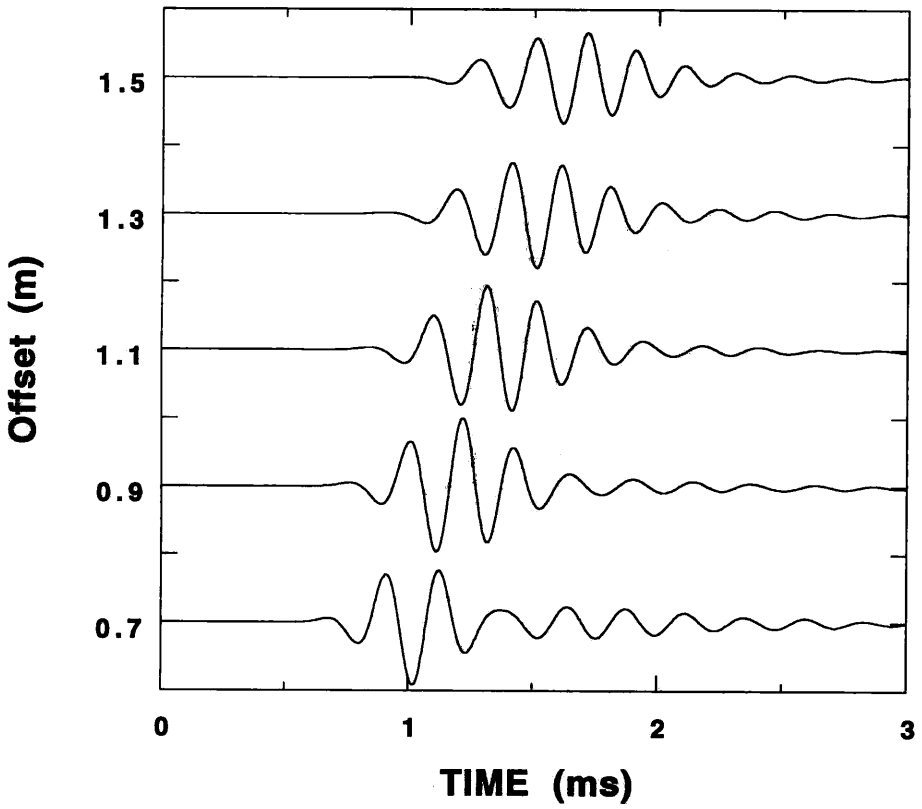

Figure 3-26: Seismograms from the borehole near a horizontal bed. Dipole source is parallel to the bed and the center frequency is 3 kHz. Waveforms are the velocity v_y at the borehole center.

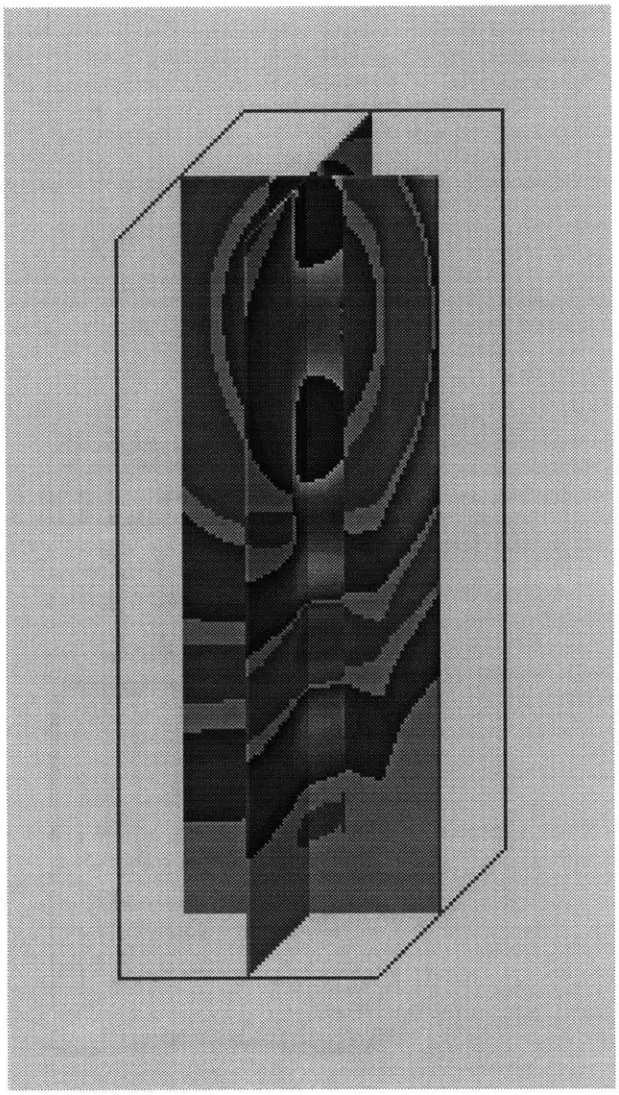

Figure 3-27: The snapshot of velocity v_x from the borehole near the horizontal bed at time 1.1 ms. The dipole source is toward the bed and the center frequency is 3.0 kHz. The image size is $70 \times 70 \times 200$.

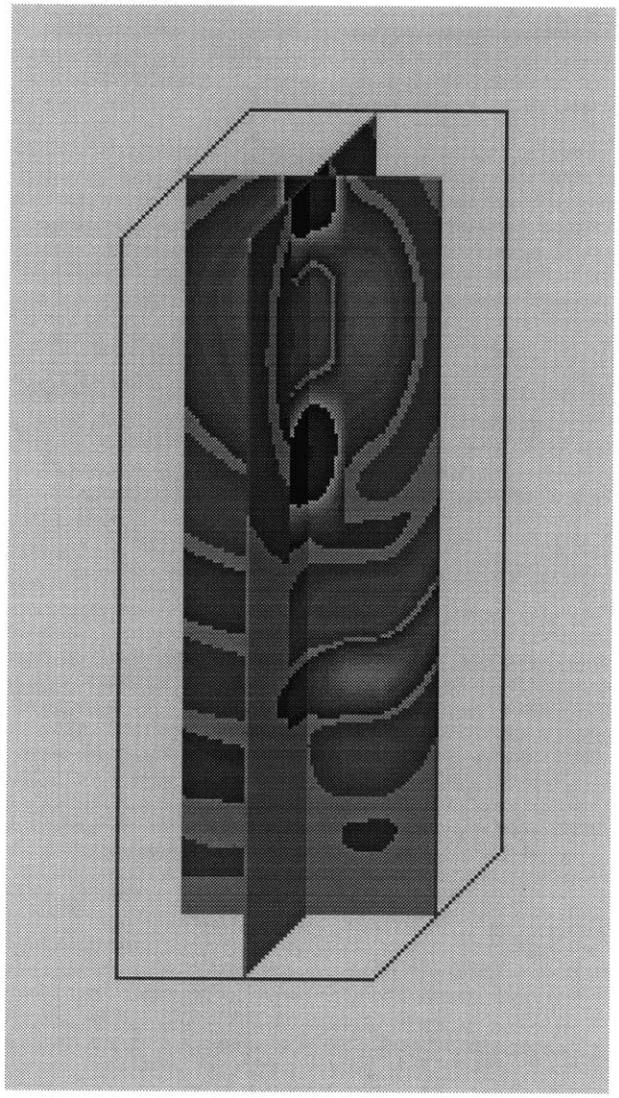

Figure 3-28: The snapshot of velocity v_y from the borehole near the horizontal bed at time 1.1 ms. The dipole source is parallel to the bed and the center frequency is 3.0 kHz. The image size is $70 \times 70 \times 200$.

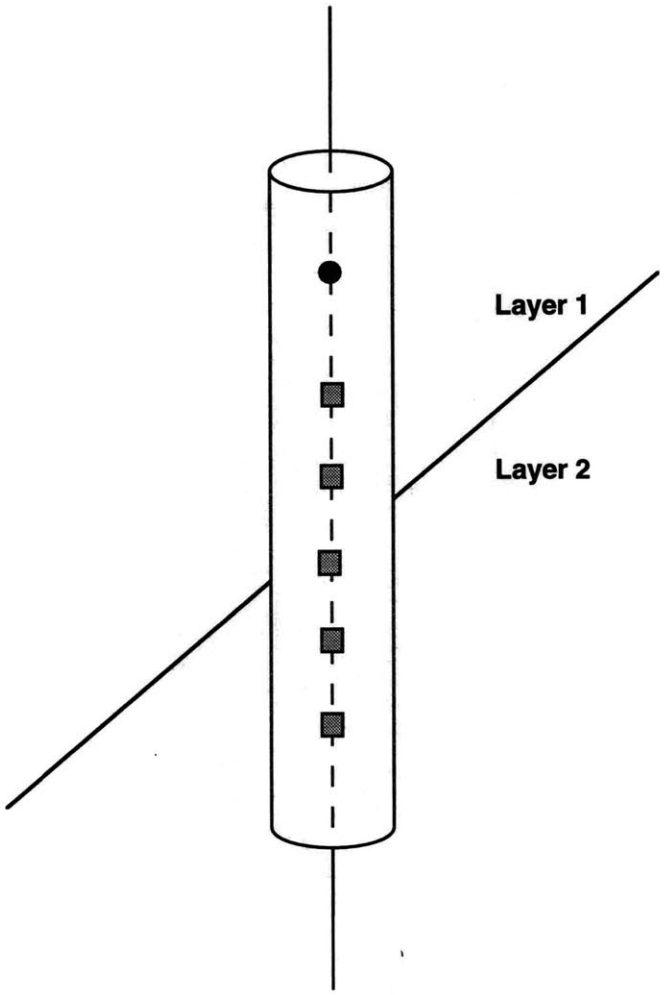

Figure 3-29: Geometry of the borehole in a 45 degree tilted layer formation. The source (solid circle) and receivers (shaded square) are shown.

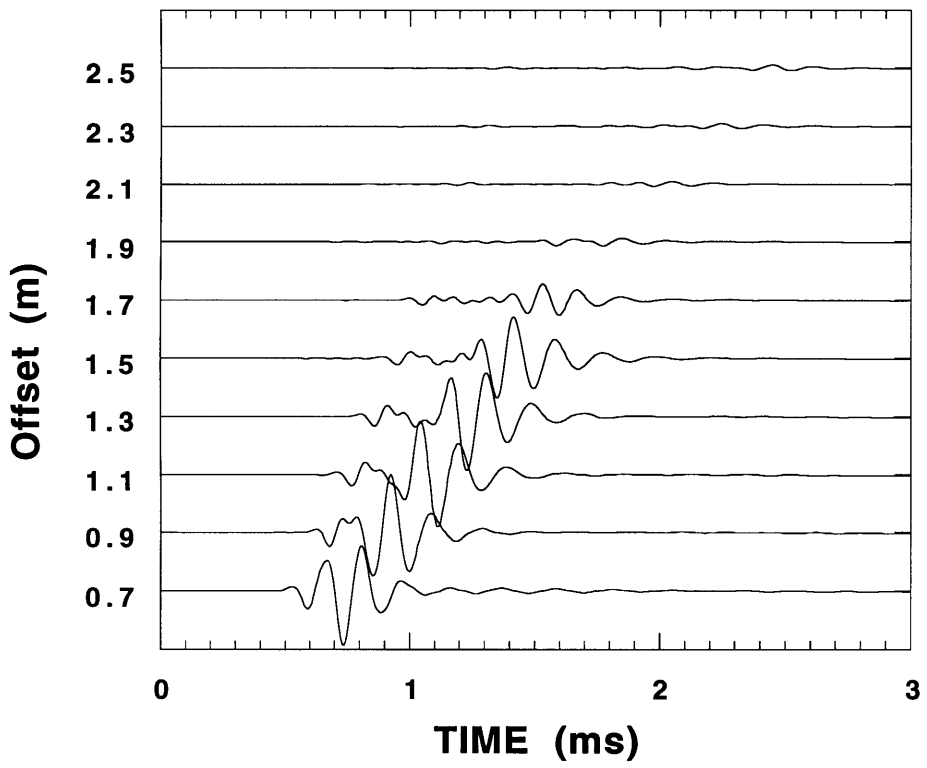

Figure 3-30: Seismograms in the borehole near a 45 degree tilted layer boundary. Monopole source center frequency is 7 kHz. Waveforms are the pressure at the borehole center.

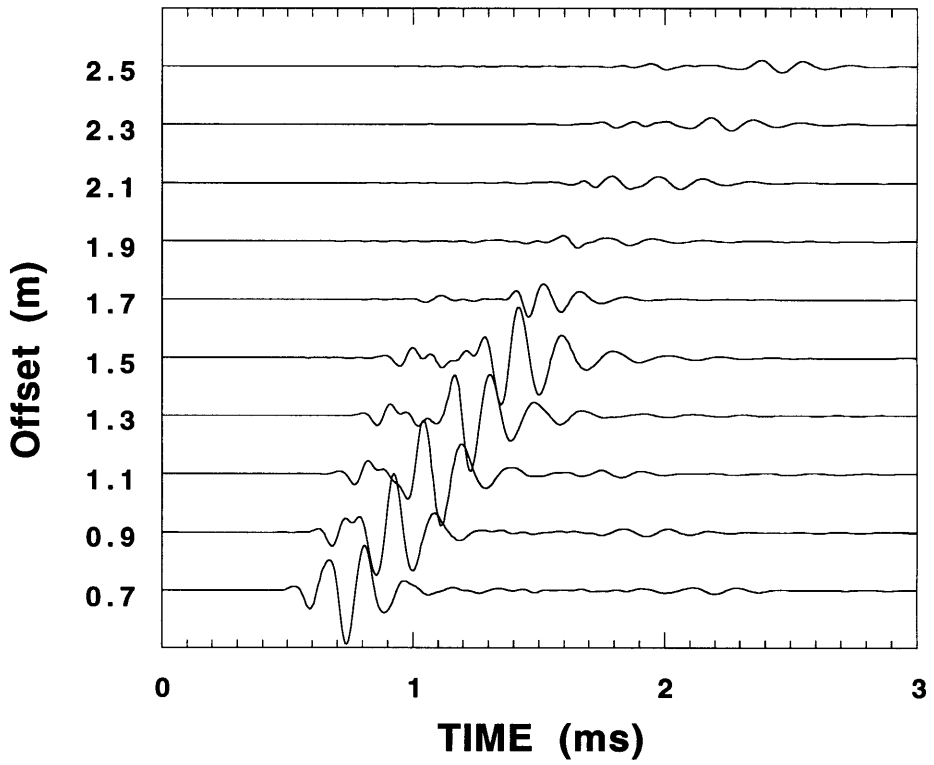

Figure 3-31: Seismograms in the borehole near a horizontal layer boundary. Monopole source center frequency is 7 kHz. Waveforms are the pressure at the borehole center.

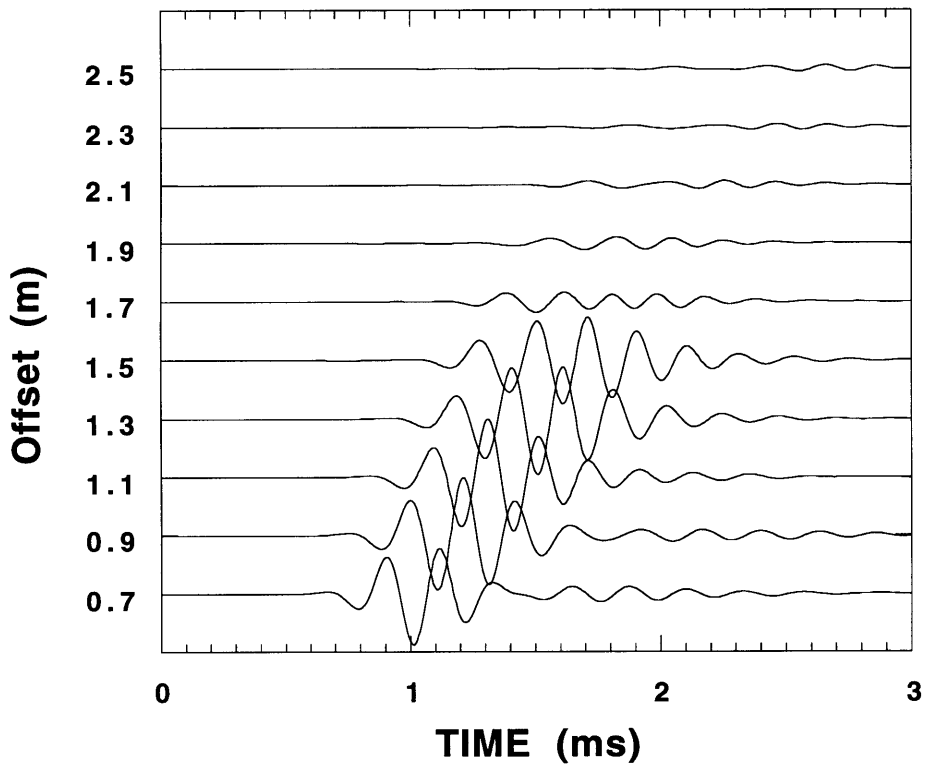

Figure 3-32: Seismograms in the borehole near a 45 degree tilted layer boundary. Dipole source, with 3 kHz center frequency, is parallel to the layer boundary strike. The waveforms are the velocity v_y at the borehole center.

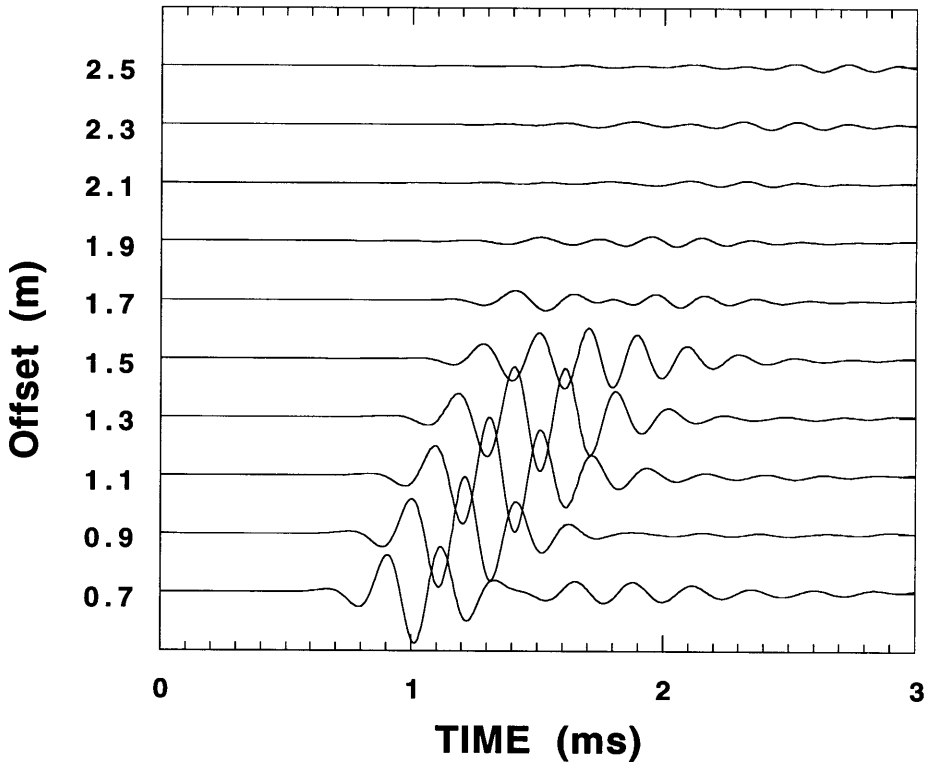

Figure 3-33: Seismograms in the borehole near a 45 degree tilted layer boundary. Dipole source, with 3 kHz center frequency, is perpendicular to the layer boundary strike. The waveforms are the velocity v_x at the borehole center.

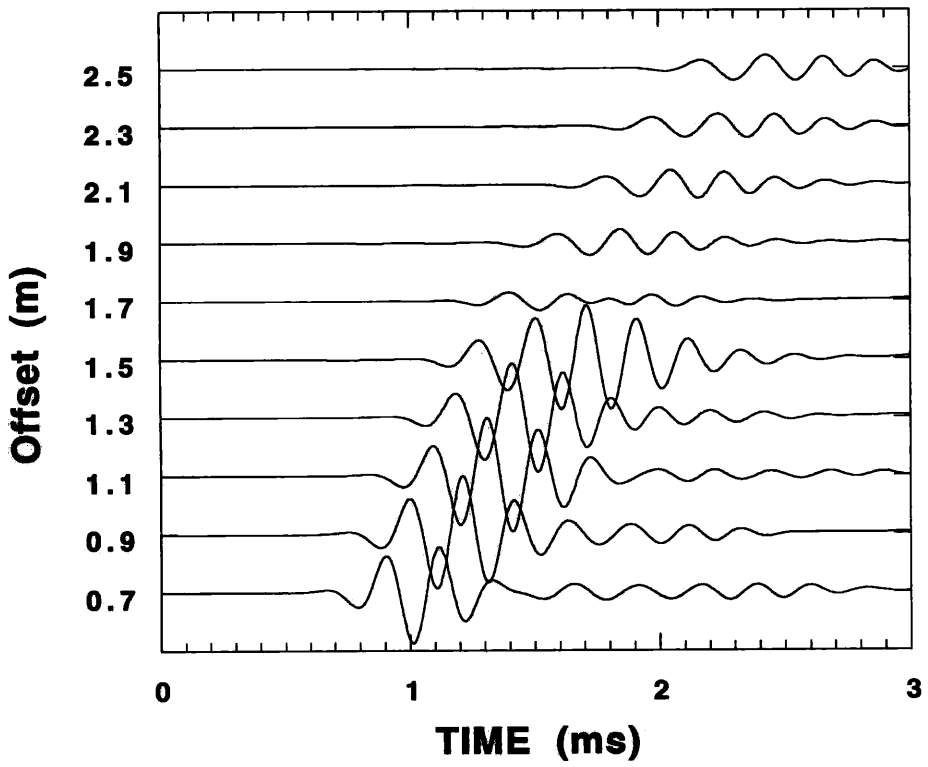

Figure 3-34: Seismograms in the borehole near a horizontal layer boundary. The source center frequency is 3 kHz. Waveforms are the velocity v_x at the borehole center.

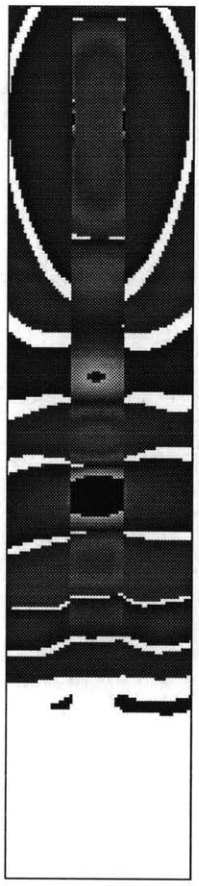

Figure 3-35: The snapshot of velocity v_x from the borehole near the horizontal layer boundary at time 1.4 ms. It is a 2-D slice of a 3-D image including the borehole axis. The image size is 70×300.

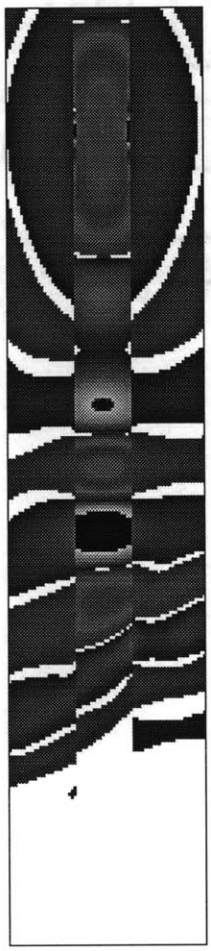

Figure 3-36: The snapshot of velocity v_y from the borehole near the 45 degree tilted layer boundary at time 1.4 ms. It is a 2-D slice of a 3-D image including the borehole axis. The image size is 70×300.

Chapter 4

Applications To Borehole Wave Propagation: Anisotropy Effect

4.1 Introduction

The crust of the Earth is slightly anisotropic, which is related to geological processes. For example, anisotropy can be caused by aligned fractures in the rock. Knowledge of this anisotropy might help to determine stress or fluid flow directions. Fine layered sedimentary rocks possess transverse isotropy. Acoustic logging provides a technique to measure the anisotropy in the crust.

The effects of the formation anisotropy on the fluid-filled borehole wave propagation are studied by a number of authors. In the case of a transversely isotropic formation with the symmetry axis aligned with the borehole axis, White and Tongtaow (1981) studied the monopole and the dipole logs. Chan and Tsang (1983) examined the refracted waves in a radially layered transversely isotropic formation. Schmitt (1989) investigated the body waves and normal modes in a radially layered transversely isotropic and permeable formation. Leveille and Seriff (1989) and Nicoletis et al. (1990) determined the particle motion and the phase velocity of the Stoneley wave at the zero frequency limit in the case of transverse isotropy with a symmetry axis

perpendicular to the borehole axis. Ellefsen (1990) developed the perturbation and finite element method to study borehole normal modes in a general anisotropic formation. Sinha et al. (1991) extended the perturbation method to compute borehole flexural waveforms in an anisotropic formation. Norris and Sinha (1993) also applied the perturbation method to derive Stoneley wave phase velocity in a weak anisotropy formation. Renlie and Raaen (1993) examined acoustic log in a borehole surrounded by a formation with stress-relief-induced anisotropy, which is called radial transverse isotropy. Leslie and Randall (1992) extended their 2.5-D finite difference method to model acoustic wave propagation in a borehole penetrating a general anisotropic formation. Only numerical examples of transversely isotropic formations are shown. Ultrasonic experiments are performed on a scaled borehole model in a phenolite solid. The orthorhombic phenolite is approximated as a transversely isotropic solid. The lab measurements are compared with the 2.5-D finite difference dipole synthetics.

In this chapter the 3-D finite difference time domain method is extended to include anisotropy. The finite difference results are compared with the analytic solutions in a transversely isotropic solid. Borehole wave propagations in the orthorhombic formation are simulated with a borehole drilled in different directions. Finite difference simulations are compared with the ultrasonic lab measurements using a scaled borehole model.

4.2 Finite Difference Method in an Anisotropic Medium

Wave propagation in an anisotropic elastic medium can also be described by the equation of motion:

$$\rho \frac{\partial^2}{\partial t^2} u_i = \tau_{ij,j} \tag{4.1}$$

where ρ is the density, u_i is the displacement vector, and τ_{ij} is the stress tensor. The generalized Hooke's law links the stress tensor τ_{ij} to the strain tensor ε_{ij} in a linear fashion:

$$\tau_{ij} = c_{ijkl}\varepsilon_{kl} \tag{4.2}$$

where c_{ijkl} is the fourth-order elastic constant tensor. The strain tensor is defined as:

$$\varepsilon_{ij} = \frac{1}{2}(u_{i,j} + u_{j,i}) \tag{4.3}$$

In order to simplify the elastic constants tensor in Cartesian coordinates the strain tensor is replaced by the strain vector defined as

$$E = \begin{pmatrix} \varepsilon_{xx} \\ \varepsilon_{yy} \\ \varepsilon_{zz} \\ 2\varepsilon_{yz} \\ 2\varepsilon_{xz} \\ 2\varepsilon_{xy} \end{pmatrix} \tag{4.4}$$

The stress tensor is replaced by the stress vector

$$T = \begin{pmatrix} \tau_{xx} \\ \tau_{yy} \\ \tau_{zz} \\ \tau_{yz} \\ \tau_{xz} \\ \tau_{xy} \end{pmatrix} \tag{4.5}$$

The fourth order elastic constant tensor can be replaced by a 6×6 symmetric stiffness matrix because of the symmetry property of the tensor.

$$C = \begin{pmatrix} c_{11} & c_{12} & c_{13} & c_{14} & c_{15} & c_{16} \\ & c_{22} & c_{23} & c_{24} & c_{25} & c_{26} \\ & & c_{33} & c_{34} & c_{35} & c_{36} \\ & & & c_{44} & c_{45} & c_{46} \\ & & & & c_{55} & c_{56} \\ symmetric & & & & & c_{66} \end{pmatrix} \tag{4.6}$$

Here the abbreviated subscript notations are used to reduce the four subscripts of the tensor. The relations between the full subscripts and the abbreviated subscripts in Cartesian coordinates are

Full subscript (ij) or (kl)	Abbreviated subscripts (I)
xx	1
yy	2
zz	3
yz or zy	4
xz or zx	5
xy or yx	6

The generalized Hooke's law can be written in the matrix form as:

$$T = CE \tag{4.7}$$

In this chapter, orthorhombic anisotropy of with nine elastic constant are considered. The reasons are the following: orthorhombic anisotropy gives the most general case without the normal stress and the shear strain coupling. It can be straightforward to implement on the staggered grid used in Chapter 2 (for the general anisotropy case, some average schemes are needed to make a centered finite difference operator on the staggered grid due to the offset of the normal and the shear stress). For practical geophysical applications, orthorhombic anisotropy provides very good models for most actual rocks.

An orthorhombic solid has three perpendicular planes of symmetry. The stiffness matrix is

$$\begin{pmatrix} c_{11} & c_{12} & c_{13} & 0 & 0 & 0 \\ & c_{22} & c_{23} & 0 & 0 & 0 \\ & & c_{33} & 0 & 0 & 0 \\ & & & c_{44} & 0 & 0 \\ & & & & c_{55} & 0 \\ symmetric & & & & & c_{66} \end{pmatrix} \tag{4.8}$$

For example, some type of granites possess this kind of anisotropy.

A widely used anisotropic type is the transverse isotropy, which can be reduced from the orthorhombic system. It has one axis of rotational symmetry. This solid is represented by 5 independent elastic constants. The stiffness matrix is

$$\begin{pmatrix} c_{11} & c_{12} & c_{13} & 0 & 0 & 0 \\ & c_{11} & c_{13} & 0 & 0 & 0 \\ & & c_{33} & 0 & 0 & 0 \\ & & & c_{44} & 0 & 0 \\ & & & & c_{44} & 0 \\ symmetric & & & & & c_{66} \end{pmatrix} \tag{4.9}$$

where $c_{12} = c_{11} - 2c_{66}$. Transverse isotropy is used to model rocks with aligned fractures, sedimentary rocks or the layered earth in which the layer thickness is much smaller than the wavelength.

Orthorhombic anisotropy can also be reduced to the other types. For example, when $c_{11} = c_{22}$, $c_{23} = c_{13}$ and $c_{44} = c_{55}$, the orthorhombic system reduces to a 6 constants tetragonal system. When $c_{11} = c_{22} = c_{33}$, $c_{44} = c_{55} = c_{66}$ and $c_{12} = c_{13} = c_{23}$, the orthorhombic system reduces to a 3 independent elastic constants cubic system.

When the elastic constants are not dependent on the orientation, the solid is called

isotropy. There are two independent parameters. The stiffness matrix is

$$\begin{pmatrix} c_{11} & c_{13} & c_{13} & 0 & 0 & 0 \\ & c_{11} & c_{13} & 0 & 0 & 0 \\ & & c_{11} & 0 & 0 & 0 \\ & & & c_{44} & 0 & 0 \\ & & & & c_{44} & 0 \\ symmetric & & & & & c_{44} \end{pmatrix} \tag{4.10}$$

where $c_{11} = c_{13} + 2c_{44}$. Using Lamé constants, $c_{13} = \lambda$, $c_{44} = \mu$ and $c_{11} = \lambda + 2\mu$. This is the case we discussed in Chapter 2 and Chapter 3.

Equation (4.1) and (4.7) are reformulated by using velocity and stress for the orthorhombic anisotropic medium. The first order hyperbolic equations in Cartesian coordinates can be written in their components form as

$$\begin{aligned} \rho\frac{\partial v_x}{\partial t} &= \frac{\partial \tau_{xx}}{\partial x} + \frac{\partial \tau_{xy}}{\partial y} + \frac{\partial \tau_{xz}}{\partial z} \\ \rho\frac{\partial v_y}{\partial t} &= \frac{\partial \tau_{xy}}{\partial x} + \frac{\partial \tau_{yy}}{\partial y} + \frac{\partial \tau_{yz}}{\partial z} \\ \rho\frac{\partial v_z}{\partial t} &= \frac{\partial \tau_{xz}}{\partial x} + \frac{\partial \tau_{yz}}{\partial y} + \frac{\partial \tau_{zz}}{\partial z} \end{aligned} \tag{4.11}$$

and

$$\begin{aligned} \frac{\partial \tau_{xx}}{\partial t} &= c_{11}\frac{\partial v_x}{\partial x} + c_{12}\frac{\partial v_y}{\partial y} + c_{13}\frac{\partial v_z}{\partial z} \\ \frac{\partial \tau_{yy}}{\partial t} &= c_{12}\frac{\partial v_x}{\partial x} + c_{22}\frac{\partial v_y}{\partial y} + c_{23}\frac{\partial v_z}{\partial z} \\ \frac{\partial \tau_{zz}}{\partial t} &= c_{13}\frac{\partial v_x}{\partial x} + c_{23}\frac{\partial v_y}{\partial y} + c_{33}\frac{\partial v_z}{\partial z} \\ \frac{\partial \tau_{xy}}{\partial t} &= c_{44}(\frac{\partial v_x}{\partial y} + \frac{\partial v_y}{\partial x}) \\ \frac{\partial \tau_{xz}}{\partial t} &= c_{55}(\frac{\partial v_x}{\partial z} + \frac{\partial v_z}{\partial x}) \\ \frac{\partial \tau_{yz}}{\partial t} &= c_{66}(\frac{\partial v_y}{\partial z} + \frac{\partial v_z}{\partial y}) \end{aligned} \tag{4.12}$$

The above equations are discretized on the staggered grid shown in Figure 2-1. Because we only consider the orthorhombic anisotropic medium, the normal stress and shear strain are not related by Hooke's law. The finite difference operators, defined in Chapter 2, are properly centered. The first order time derivative is approximated by the second order finite difference operator and the first order space derivatives are approximated by the fourth order finite difference operators. These operators are described in Chapter 2. The medium parameters $c_{11}, c_{12}, c_{13}, c_{22}, c_{23}, c_{33}, c_{44}, c_{55}, c_{66}$ and ρ are assigned at the grid point $(m+\frac{1}{2}, n+\frac{1}{2}, k)$. In order to update the velocities, the needed density values are obtained from the average of two nearby assigned densities. In order to update the shear stress, the needed shear moduli are determined by four nearby assigned shear moduli using the harmonic average. This automatically puts the shear modulus zero at the fluid-solid boundary.

To control the grid dispersion and the grid anisotropy we adopt the same rule of thumb used in Chapter 2. The stable condition used to determine the time step size is

$$\Delta t < \frac{\Delta}{\sqrt{3} v_p (|\eta_1| + |\eta_2|)} \tag{4.13}$$

where v_p is the fastest quasi-P wave velocity in the model.

In order to simulate the infinite medium on a computer with limited memory we have to eliminate the reflections from the artificial boundaries. Higdon's absorbing boundary condition operator is generalized to an anisotropic medium

$$B = \prod_{j=1}^{m} (c_j \frac{\partial}{\partial t} - \alpha \frac{\partial}{\partial x}) \tag{4.14}$$

because in the anisotropic medium, the wave propagates with the different velocity in the different directions. The velocity α in the absorbing boundary condition is properly chosen according to the direction of the boundary. As example, for the boundary at $x = x_0$ for the P wave absorbing term we choose $\alpha = \sqrt{\frac{c_{11}}{\rho}}$ and for the

boundary at $y = y_0$ for the P wave absorbing term we choose $\alpha = \sqrt{\frac{c_{22}}{\rho}}$.

Finally, the 3-D finite difference scheme for an orthorhombic medium is implemented on the nCUBE parallel computer by using the Grid Decomposition Package. The constants of the orthorhombic medium are stored in a small data array instead of ten full 3-D arrays so as to reduce the memory requirements. At every grid point an index file is searched to determine which constants will be used in the calculations.

4.3 Comparison With the Analytic Solution

In this section the finite difference method is tested in a homogeneous transversely isotropic medium. The same test is used by Carcione et al. (1992) to verify their 3-D spectral scheme for wave propagation in anisotropic media.

The medium chosen for the test is Mesaverde clay shale (Thomsen, 1986). It is a transversely isotropic solid. The properties of the clay shale are listed in Table 4.1. The slowness surfaces are plotted in Figure 4-1. The 3-D slowness surfaces have azimuthal symmetry. The plotted 2-D section (X-Z plane) contains the symmetry axis. There are three types of wave: quasi-P, quasi-S and pure shear. Quasi-P and quasi-S are coupled.

The parameters used for the finite difference calculations are the following: A $70 \times 70 \times 200$ grid with grid size of 4 cm and time step size 0.002 ms. The source is a point vertical force. The source time function is a Kelly wavelet at center frequency 2.5 kHz. The source-receiver distance is 4 m along the Z axis. The second order Higdon's absorbing boundary condition is used. The analytical solution of a vertical force acting along the symmetry axis of a transversely isotropic solid is given in Appendix C.

Figure 4-2 compares the normalized finite difference and the analytical solutions from the vertical force. The total time is 4 ms. The vertical velocity v_z is shown in the plot. The agreement is excellent. Figure 4-3 shows the wavefield snapshot

of the vertical velocity v_z at time 1.6 ms. The 3-D image is sliced at the XZ, YZ and XY plane. The wavefield is symmetric about the Z axis. The wavefronts are no longer spherical because of the anisotropy. The seismogram and the snapshot show the good performance of Higdon's absorbing boundary condition in the anisotropic medium with properly chosen velocities.

4.4 Borehole Wave Propagation in Orthorhombic Medium

In this section the 3-D time domain finite difference method is applied to the fluid-filled borehole wave propagation in an orthorhombic formation. The anisotropic elastic constants used here are obtained from phenolite XX-324. The phenolite possesses a strong anisotropy and can be described as an orthorhombic solid (Cheadle et al., 1991). The elastic constants of phenolite are determined from the lab velocity measurements. The monopole and dipole logs are simulated in the borehole drilled along the X, Y and Z axis. The finite difference synthetics are compared with the ultrasonic measurements in the scaled borehole model.

4.4.1 Elastic constants of phenolite

A cubic sample of the phenolite is used to do the property measurements (Zhu et al., 1993). The P and S wave velocities are measured along the three principal axes by using the compressional and shear wave transducers (Figure 4-4). The three principal axes are assigned as X, Y and Z. The velocity values are labeled with two indexes. The first is the direction of the propagation and the second is the direction of the particle motion. The six independent velocities can be used to determine six elastic constants along the diagonal of the stiffness matrix. Another three velocity measurements are needed to determine the three off-diagonal constants. The measuring is done between the opposite edges of the phenolite cube (Z. Zhu, 1993, personal communication).

The propagation directions are at a 45 degree angle between two principal axes and perpendicular to the third. The results are listed in Table 4.2. Using the body wave phase velocity formulas given in Appendix D for the orthorhombic solid, nine elastic constants can be determined. The values are listed in Table 4.3. The slowness surfaces of phenolite can be recalculated by using these nine elastic constants. The 3-D slowness surface is sliced at the X-Y plane, the X-Z plane and the Y-Z plane. It is shown in Figure 4-5. The anisotropy is very clear in the plot. The shear wave velocity anisotropy is about 28% and the P wave velocity anisotropy is about 30%.

4.4.2 Borehole wave propagation: monopole

The monopole log in a fluid-filled borehole with the phenolite solid as formation is calculated. The borehole fluid is water. Its velocity is 1500 m/s and the density is 1 g/cm^3. The borehole diameter is 0.24 m. It is numerically drilled along the Y axis. A $70 \times 300 \times 70$ grid is used for the calculations. The grid size is 1 cm and the time step is 0.001 ms. The monopole Kelly source at center frequency 5 kHz is located at (35,40,35) on the grid. The ten pressure receivers are located along the borehole center. The first receiver is 0.7 m away from the source and receiver spacing is 0.2 m.

The seismograms are plotted in Figure 4-6. The first P wave arrival is traveling with velocity v_{yy}, which is 3620 m/s. The large amplitude low frequency Stoneley wave is traveling with phase velocity about 1220 m/s. If the formation is isotropic and the shear wave velocity is 1390 m/s, the Stoneley wave phase velocity is about 1100 m/s. If the formation is isotropic and the shear wave velocity is 1940 m/s, the Stoneley wave phase velocity is about 1300 m/s. So the Stoneley wave velocity in the orthorhombic formation is about the average of these two velocities. Because of the shear wave anisotropy (velocity v_{yx} is greater than the fluid velocity), the shear-pseudo-Rayleigh arrival is observed between the P and Stoneley wave arrivals.

To better understand the phenomenon, the simulation of the wave propagation is done with the borehole numerically drilled along the Z axis. A $70 \times 70 \times 300$ grid

is used. All the other parameters are kept the same. The shear wave is transversely isotropic along the Z axis. The seismograms are shown in Figure 4-7. This time the P wave is traveling with velocity v_{zz}, which is 2740 k/m. The low frequency Stoneley waves have about the same velocity as in the Y borehole. But in the borehole along the Z axis there are no shear-pseudo-Rayleigh arrivals. This is because both v_{zx} and v_{zy} are below the fluid velocity.

4.4.3 Borehole wave propagation: dipole

First the fluid-filled borehole is drilled along the Y axis. Other parameters are the same as the monopole simulations. The waveforms of the dipole source in the X direction are plotted in Figure 4-8. The seismograms are dominated by the flexural modes. Due to the strong shear wave anisotropy, there are two widely separated shear wave arrivals. The fast one is traveling with velocity v_{yx}. The slow one is traveling with velocity v_{yz}. The dipole source is aligned with the fast velocity direction (Figure 4-4). But the dipole source has a radiation pattern of $cos\theta$. So there is energy in the slow shear wave direction too. The slow shear wave velocity means that the small stress can produce large strain, especially when the shear wave is less than the fluid velocity. That is why the large amplitude slow shear wave shows on the seismograms. On the other hand, when the dipole source is aligned in the direction of the slow shear wave (Figure 4-10), there is a very small fast shear arrival shown on the seismograms. The first arrivals on the seismograms are P waves.

For the purpose of comparison the dipole waveforms are also computed in the borehole along the Z axis. The seismograms are plotted in Figure 4-11. In this case both shear wave velocities (v_{xz}, v_{yz}) have the same value and are less than the fluid velocity. The waveforms are dominated by the slow flexural mode.

It is very interesting to look at the wavefield snapshots. This is one of the advantages of the finite difference method. The snapshot of the X direction dipole wavefields in the borehole along the Y axis at time 1.1 ms is shown in Figure 4-9.

This is the case of the fast and the slow shear wave splitting due to the anisotropy. It is beautifully displayed in the snapshot. The fast flexural wave is the one traveling in the first pack. The wavefields spread into the formation. The reason is that the faster shear wave velocity is greater than the borehole fluid velocity. The borehole is not a very effective waveguide. The slow flexural wave is the one trapped inside or near the borehole, because the slow shear wave velocity is less than the borehole fluid velocity. The borehole becomes a very effective waveguide for the slow flexural mode.

The snapshot of the X direction dipole wavefields in the borehole along the Z axis at time 1.1 ms is shown in Figure 4-12. In this case the shear wave velocity v_{zx} and v_{zy} are the same, so there is no shear wave splitting. This is exactly what the snapshot shows. The single flexural wave dominates the wavefields. The other wavefield anomaly is in the source region. The images also show vividly the good performance of the absorbing boundary condition.

In the previous examples, the dipole source and receiver are pointed in the same direction (inline dipole). Here we show one example of the dipole source and receiver that are perpendicular to each other (cross dipole). In the isotropic formation the cross dipole should be zero. But in the anisotropic formation the cross dipole log, combined with the inline dipole log, can provide very useful information about the orientation of the shear wave fast and slow directions. This information can be used to estimate the stress orientations or fluid flow directions.

For the fluid-filled borehole drilled along the Y axis, the source is pointed 45 degrees from the X axis and the receiver is 135 degrees from the X axis. The cross dipole waveforms are plotted in Figure 4-13. The waveforms clearly show the fast and slow shear wave arrivals. Small amplitude P waves are also shown as first arrivals. The shear wave arrivals on the cross dipole can be viewed as follows: The source dipole generates the flexural mode, which is polarized along the two principal axes (X and Z axis). Then they are superposed along the receiver direction. In this case the amplitude of the cross dipole has the same magnitude as the inline dipole. But

the simulations also show that when the cross dipole direction is aligned with the principle axis its amplitude is about 100 times less than the inline dipole.

4.5 Comparison With Ultrasonic Experiments

Finally, the finite difference synthetics are compared with the ultrasonic lab measurements. A block of $25 \times 25 \times 15$ cm^3 phenolite solid is used to do the lab measurements. A 1.27 cm diameter hole is drilled along the X axis (Zhu et al., 1993). The experiments are carried out in a water tank. The borehole fluid is water. The transducer is built using a PZT piezoelectric tube. This tube is cut in half along the diameter and four electrodes are connected to the outer and inner sides of the two half tubes. The monopole or the dipole source can be simulated by using the same tube. When the same electric voltage is applied on the two halves of the tube, the monopole source is generated. When the opposite electric voltage is applied on the two halves of the tube, the dipole source is generated. The monopole and dipole receivers are built using the same method.

This ultrasonic model is amplified by a factor of 20 to do the finite difference simulations. The calculation grid is $320 \times 70 \times 70$. The grid size is 1 cm. The source is located at grid point (40,35,35). The receivers are located along the center of the borehole. The first receiver is 1.5 m away from the source and the receiver spacing is 0.1 m. The monopole waveforms from the finite difference simulation are plotted in Figure 4-14. A Kelly source with 5 kHz center frequency is used. Ultrasonic lab measurements of the monopole waveforms are plotted in Figure 4-15. The time scale of the lab measurements is 20 times smaller than the finite difference results. There is a 0.0072 ms time delay in the lab measurements. The receiver spacing is 0.5 cm. The finite difference results agree well with the lab measurements. Both the synthetics and the measurements very clearly shown the arrivals of the P wave, the shear-pseudo-Rayleigh waves, and the low frequency large amplitude Stoneley waves. The first P

wave arrival is traveling with phase velocity v_{xx}. The shear-pseudo-Rayleigh wave arrivals are caused by the fast shear wave, which is faster than the water velocity. But the Stoneley wave phase velocity is sensitive to both the fast and the slow shear waves.

The dipole waveforms from the finite difference are shown in Figure 4-16. The dipole source is aligned with the Y axis in the calculation. The scaled borehole model measurements are plotted in Figure 4-17. Both plots clearly display the fast and the slow shear wave arrivals due to the shear wave splitting in an anisotropic medium. The small P wave arrivals in the synthetics are not shown on the lab measurements because the lab measurements are low pass filtered to emphasize the two shear wave arrivals (Z. Zhu 1993, personal communication). In general, the synthetics and the lab measurements are in good agreement.

4.6 Conclusions

In this chapter the 3-D finite difference method is extended into an anisotropic medium. The velocity-stress formulation is used. The scheme is second-order accuracy in time and fourth-order accuracy in space. The Higdon's absorbing boundary condition is extended into the anisotropic medium by properly chosen velocities. Once again the scheme is paralleled on the nCUBE computer.

The finite difference results agree excellently with the analytic solution of vertical force in a homogeneous transversely isotropic solid. This comparison also shows the good performance of Higdon's absorbing boundary condition in an anisotropic medium.

Borehole wave propagation in an orthorhombic phenolite formation is simulated. The nine elastic constants of the phenolite solid are determined from lab measurements. In the borehole drilled along the Z axis, the monopole log shows the P wave traveling with velocity v_{zz}. There are no shear-pseudo-Rayleigh wave arrivals due to

the shear wave below the borehole fluid velocity. The dipole log is dominated by the single slow flexural mode.

In the borehole drilled along the Y axis, the monopole log shows that the P wave is traveling with velocity v_{yy}. Because the shear wave velocity v_{yx} is greater than the borehole fluid velocity, there are shear-pseudo-Rayleigh wave arrivals shown on the monopole log between the P wave and Stoneley wave arrivals. There is shear wave splitting in the dipole log due to the anisotropy. Two shear wave arrivals correspond to the fast flexural mode and the slow flexural mode. The Stoneley wave velocity is sensitive to both the fast and the slow shear wave velocities. The cross dipole also clearly records fast and slow shear wave arrivals.

In the borehole drilled along the X axis, the monopole log shows the P wave traveling with velocity v_{xx}. The monopole and dipole synthetics agree well with the scaled ultrasonic lab measurements.

Quantity	Value
c_{11}	66.6 GPa
c_{12}	19.7 GPa
c_{13}	39.4 GPa
c_{33}	39.9 GPa
c_{44}	10.9 GPa
ρ	2590 kg/m^3

Table 4.1: Properties of the transversely isotropic medium, which represents Mesaverde clay shale.

Direction	P wave velocity (m/s)
45 degrees to Y,Z axes 90 degrees to X axis	3200
45 degrees to X,Z axes 90 degrees to Y axis	3300
45 degrees to X,Y axes 90 degrees to Z axis	3900

Table 4.2: The P wave velocities measured between opposite edges of the phenolite cube (Z. Zhu 1993, personal communication).

Quantity	Value
c_{11}	20.80 GPa
c_{12}	11.47 GPa
c_{13}	7.26 GPa
c_{22}	17.46 GPa
c_{23}	7.87 GPa
c_{33}	10.06 GPa
c_{44}	2.59 GPa
c_{55}	2.59 GPa
c_{66}	5.04 GPa
ρ	1340 kg/m^3

Table 4.3: Properties of the orthorhombic medium, which represents Phenolic XX-324.

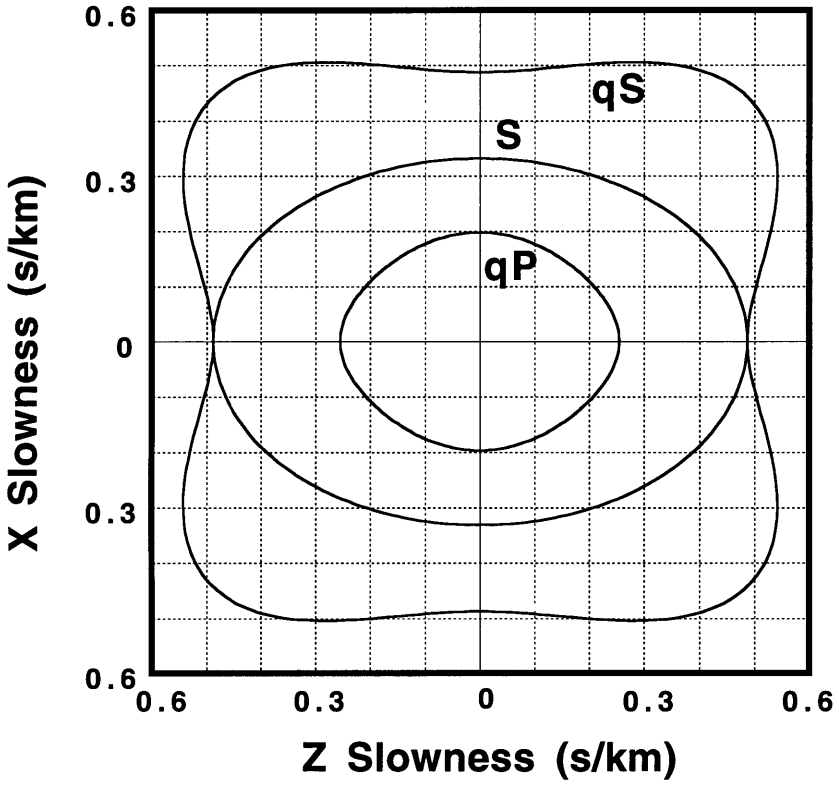

Figure 4-1: Slowness surfaces of Mesaverde clay shale. There are three modes: pure shear, quasi-P, and quasi-S.

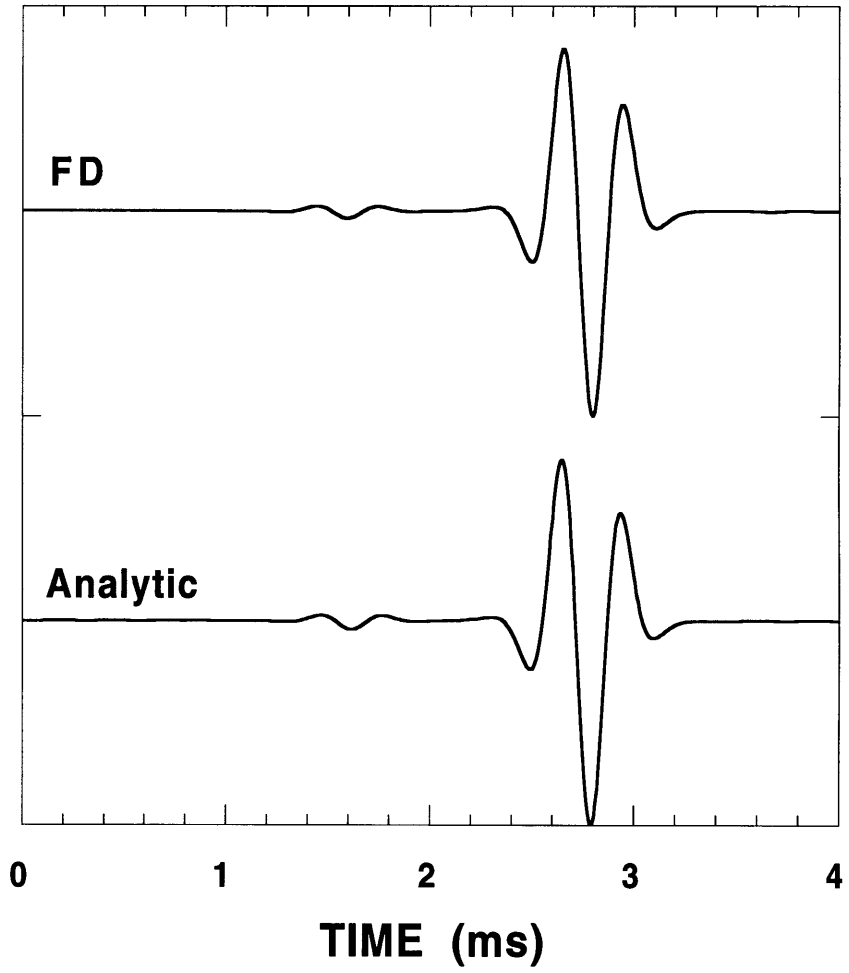

Figure 4-2: Comparison of finite difference result (FD) with analytic solution of a vertical point force in homogeneous transversely isotropic medium. The source center frequency is 2.5 kHz. Both amplitudes are normalized.

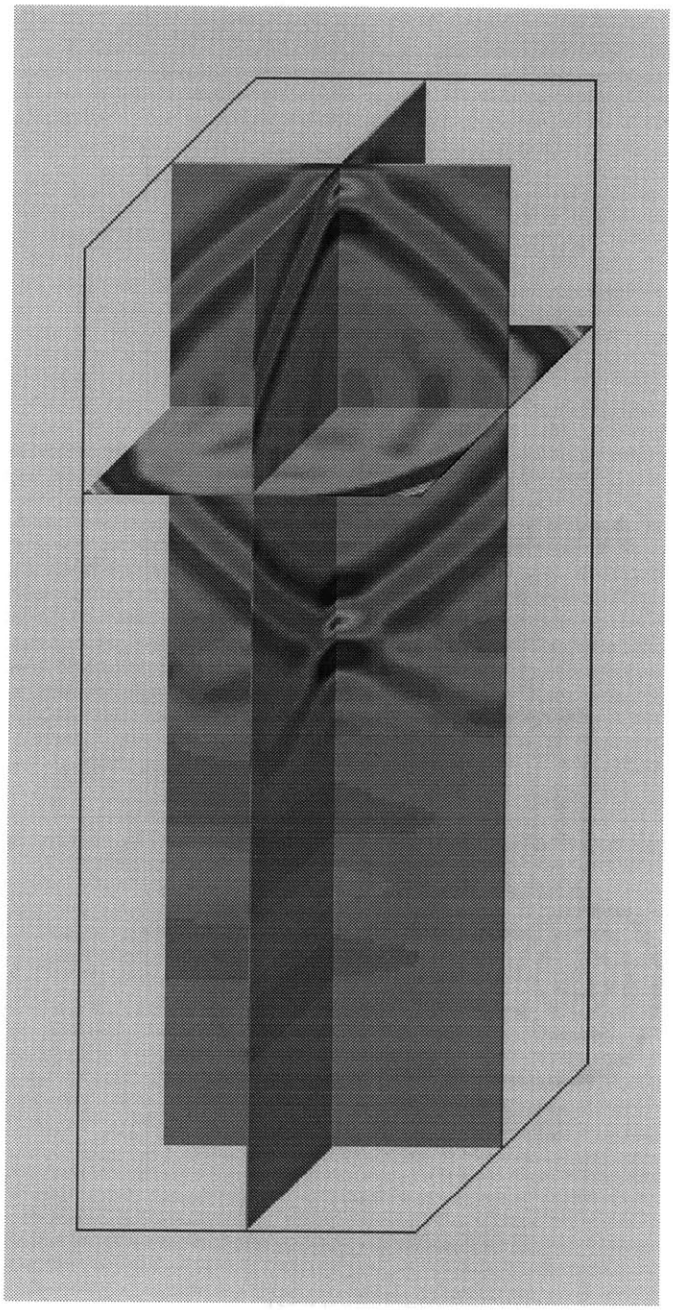

Figure 4-3: The snapshot of the velocity v_z wavefield from a vertical point force in a homogeneous transversely isotropic medium at time 1.6 ms. Source center frequency is 2.5 kHz. The image size is $70 \times 70 \times 200$.

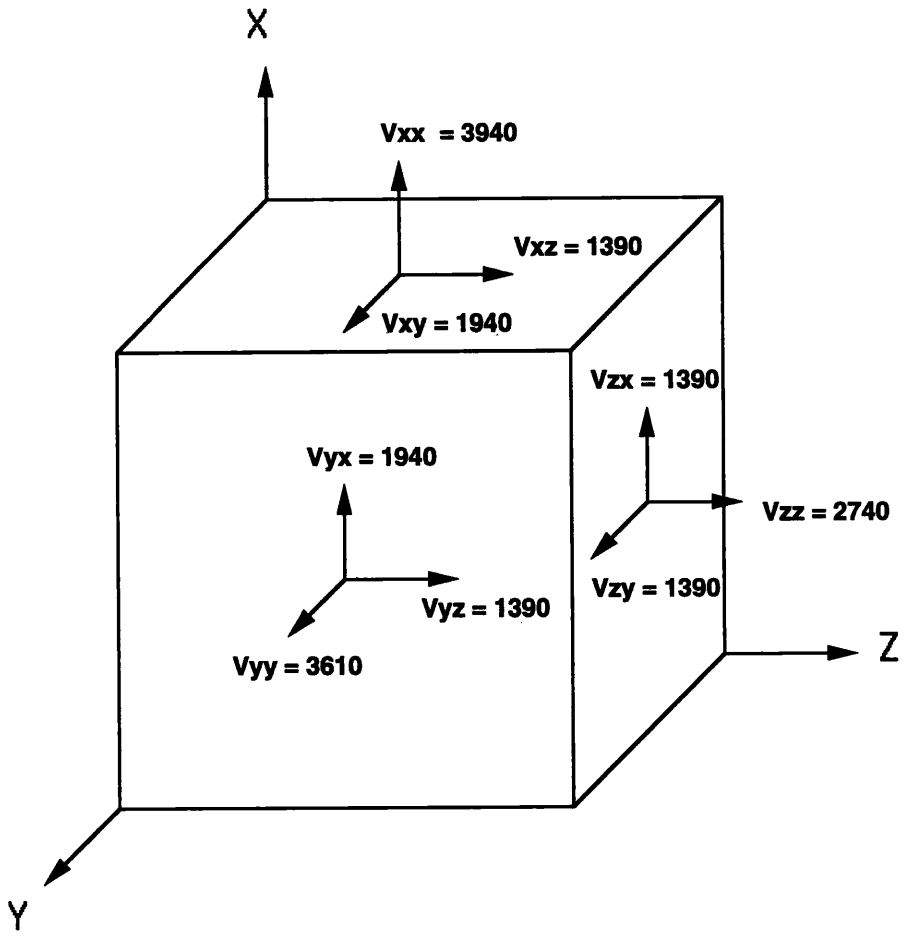

Figure 4-4: The P and S wave velocities measured along the three principal axes of a phenolite cube. The velocity is given with two indexes. The first index is the propagation direction and the second index is the particle motion direction (after Zhu et al., 1993).

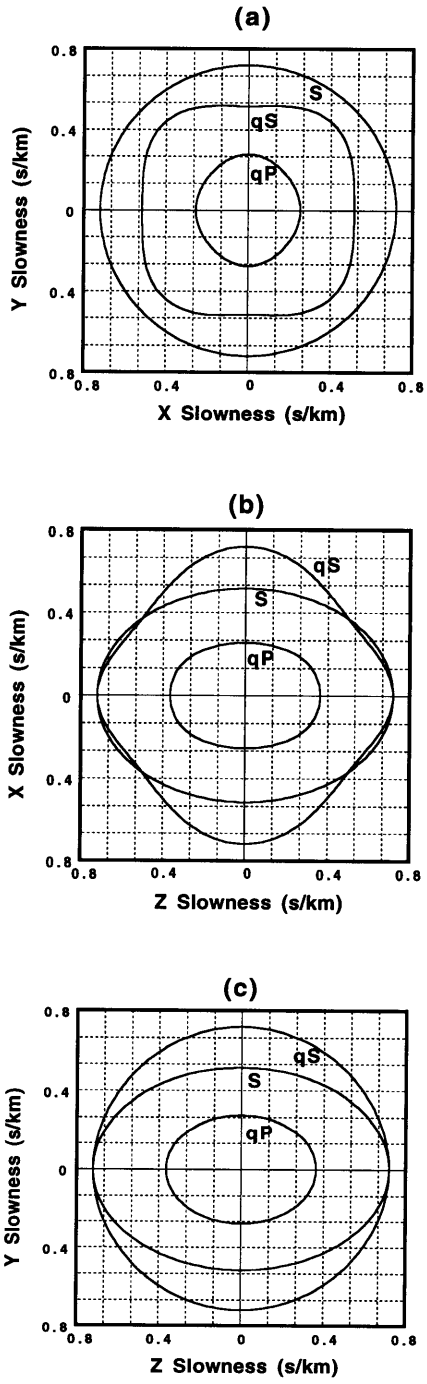

Figure 4-5: Slowness surfaces of phenolite solid. There are three modes: pure shear, quasi-P, and quasi-S. (a) X-Y plane. (b) X-Z plane. (c) Y-Z plane

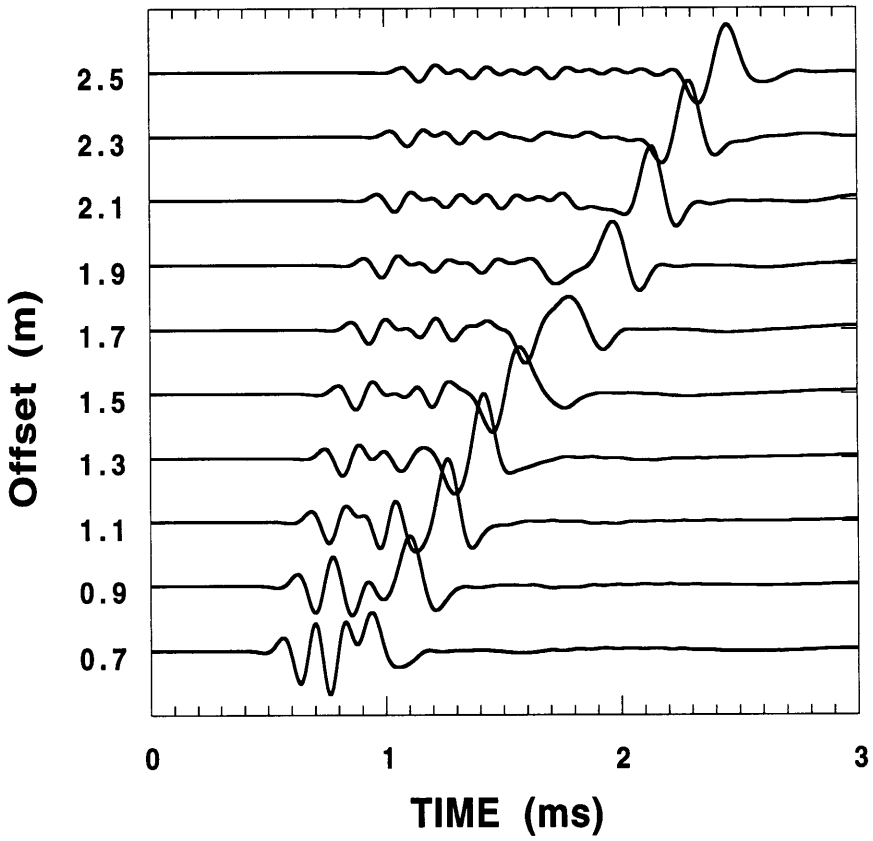

Figure 4-6: Monopole seismograms of fluid-filled borehole drilled along the Y axis in phenolite formation. Source center frequency is 5 kHz.

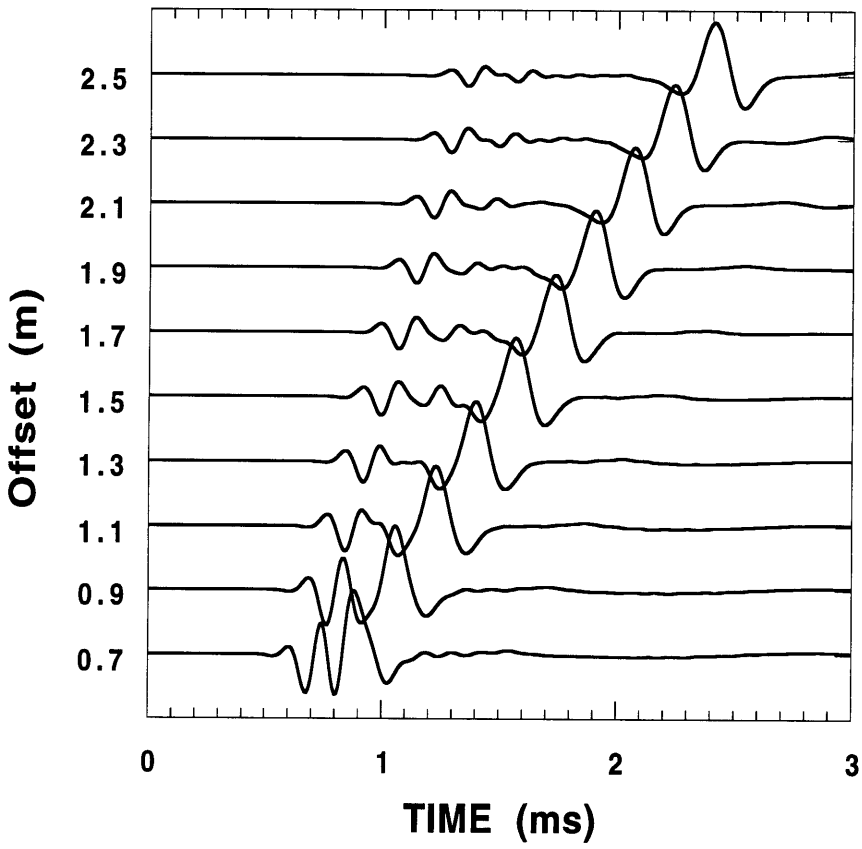

Figure 4-7: Monopole seismograms of a fluid-filled borehole drilled along the Z axis in a phenolite formation. Source center frequency is 5 kHz.

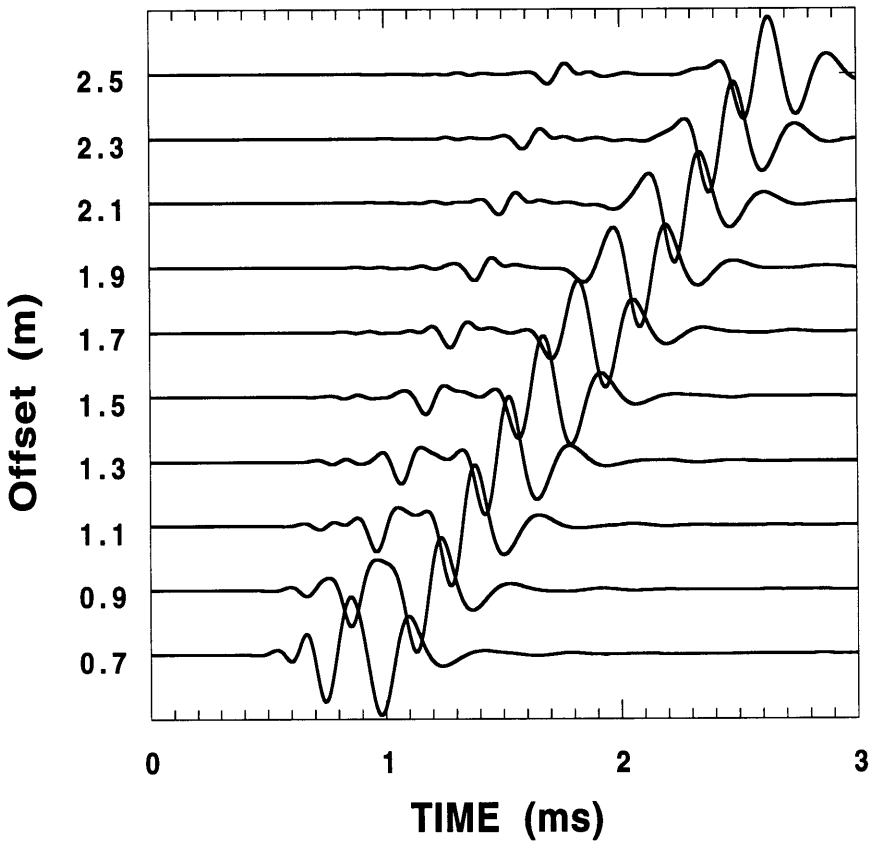

Figure 4-8: Dipole seismograms from a fluid-filled borehole drilled along the Y axis in a phenolite formation. Source center frequency is 5 kHz and dipole is in the X direction.

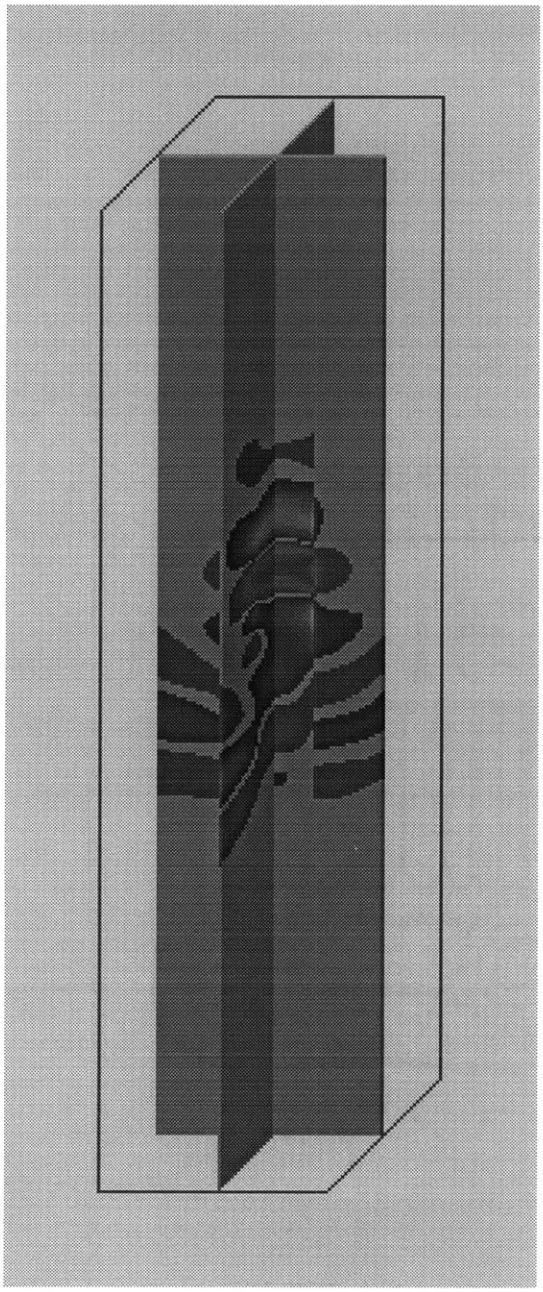

Figure 4-9: Wavefield image from a dipole source at time 1.1 ms. The fluid filled borehole is drilled along the Y axis in a phenolite formation. The vertical direction is the Y axis. Source center frequency is 5 kHz and the dipole is in the X direction.

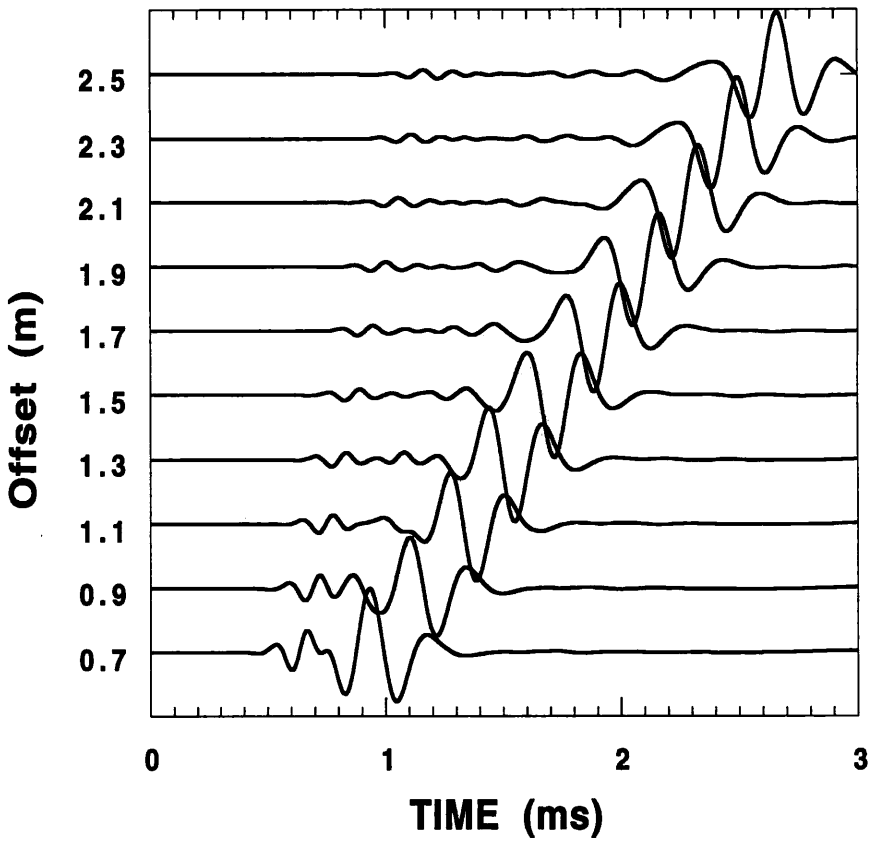

Figure 4-10: Dipole seismograms from a fluid-filled borehole drilled along the Y axis in a phenolite formation. Source center frequency is 5 kHz and the dipole is in the Z direction.

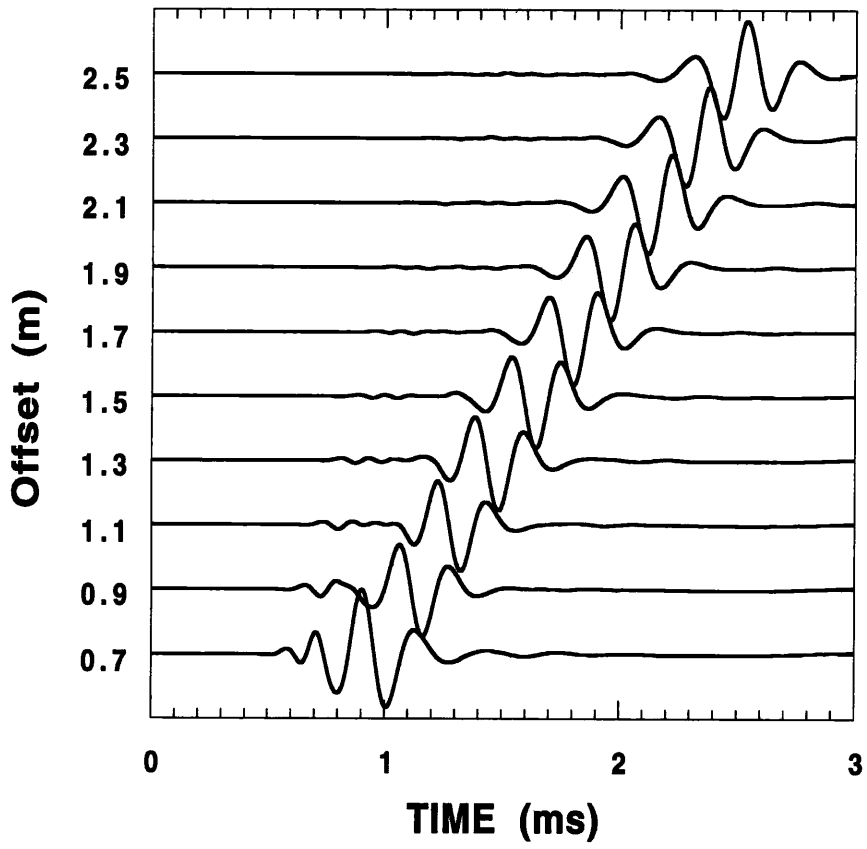

Figure 4-11: Dipole seismograms from a fluid-filled borehole drilled along the Z axis in a phenolite formation. Source center frequency is 5 kHz and the dipole is in the X direction.

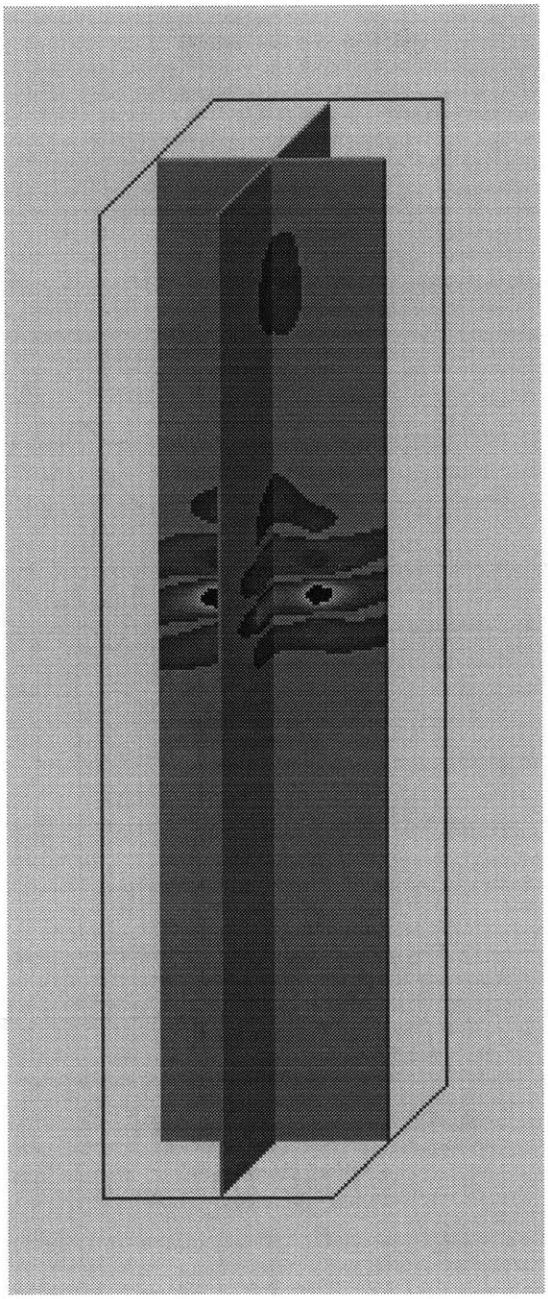

Figure 4-12: Wavefield image from a dipole source at time 1.1 ms. The fluid filled borehole is drilled along the Z axis. Source center frequency is 5 kHz and the dipole is in the X direction.

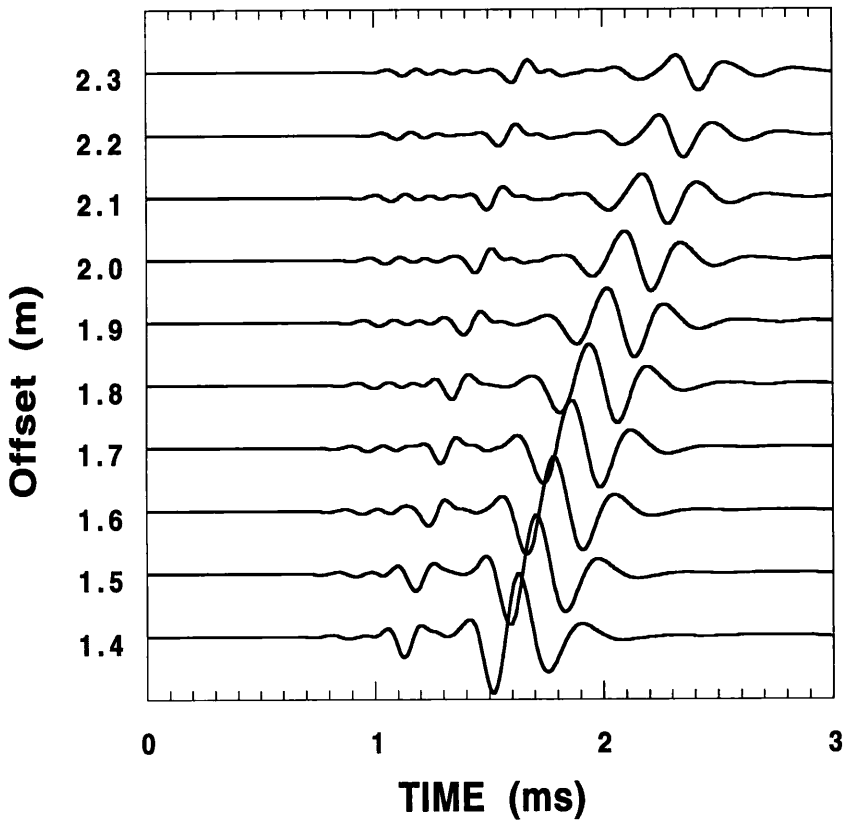

Figure 4-13: Cross dipole seismograms from a fluid-filled borehole drilled along the Y axis in a phenolite formation. Source center frequency is 5 kHz. The source dipole is 45 degrees from the X axis and the receiver dipole is 135 degrees from the X axis.

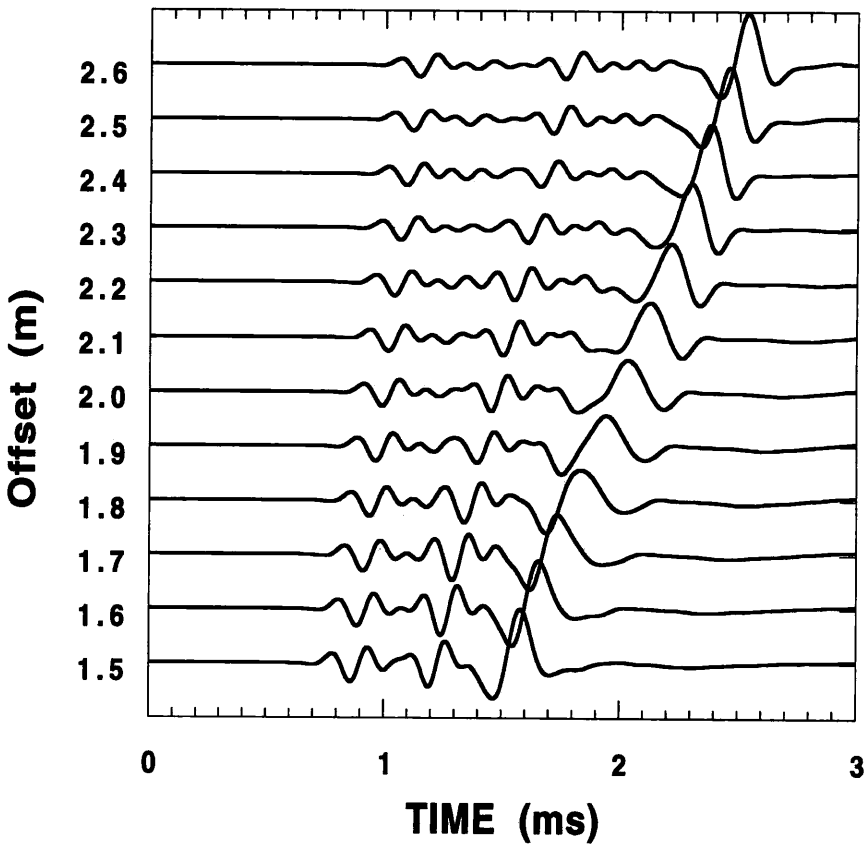

Figure 4-14: Finite difference monopole seismograms from the fluid-filled borehole drilled along the X axis in a phenolite formation. Source center frequency is 5 kHz.

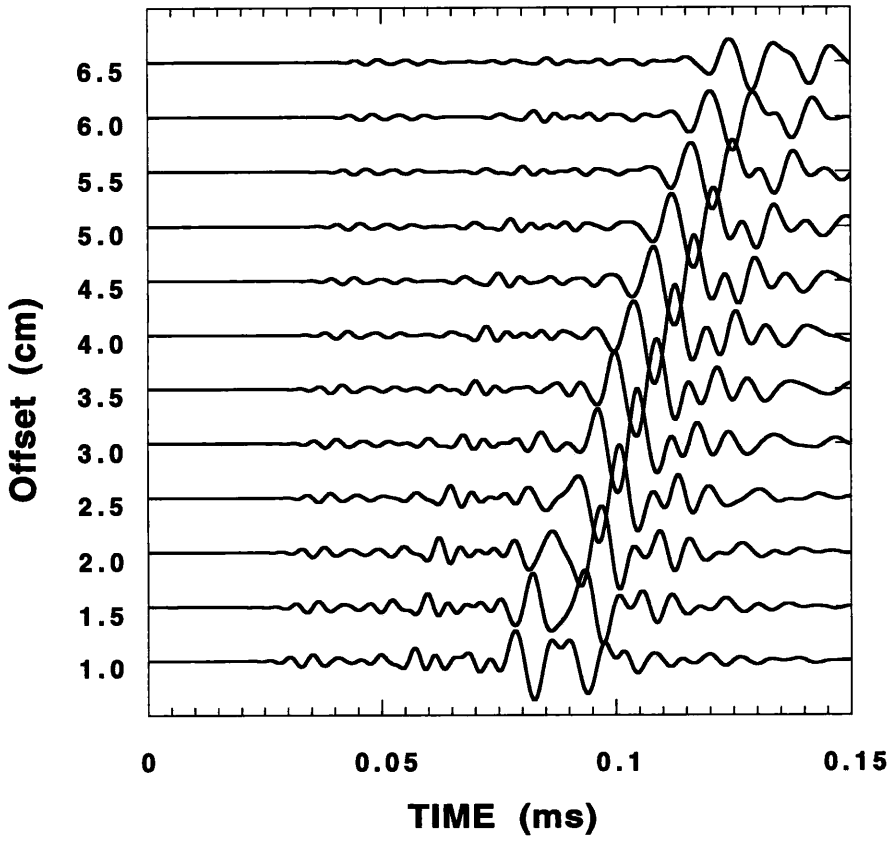

Figure 4-15: Ultrasonic lab measurement of monopole seismograms from the fluid-filled borehole drilled along the X axis in a phenolite solid (After Zhu et al., 1993).

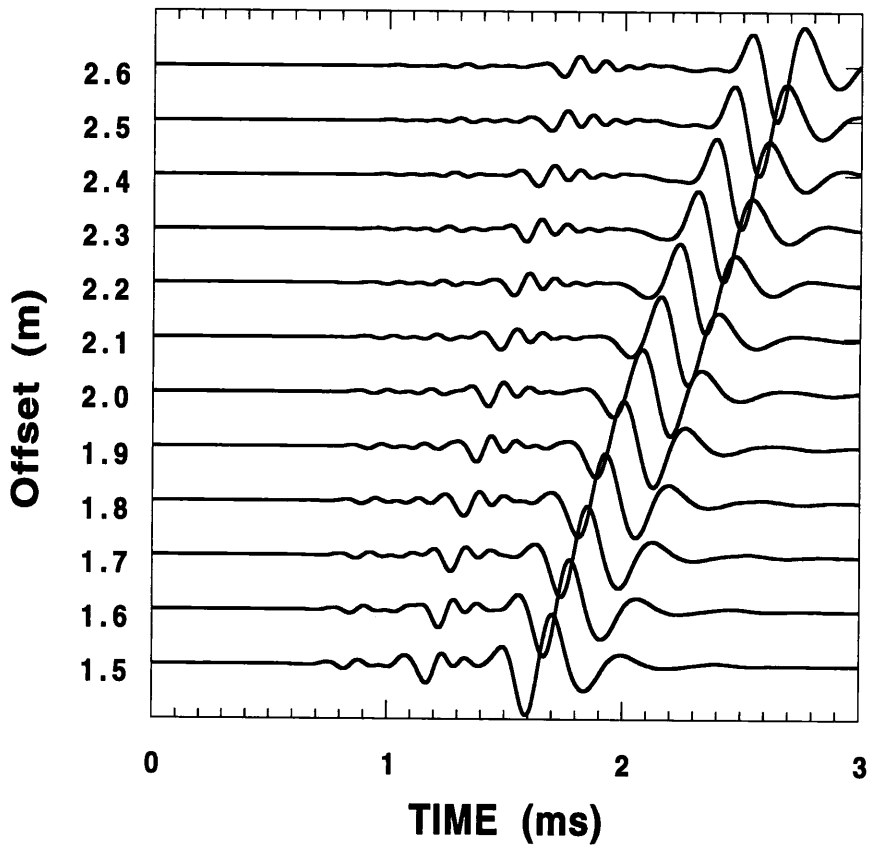

Figure 4-16: Finite difference dipole seismograms from the fluid-filled borehole drilled along the X axis in a phenolite formation. Source center frequency is 5 kHz.

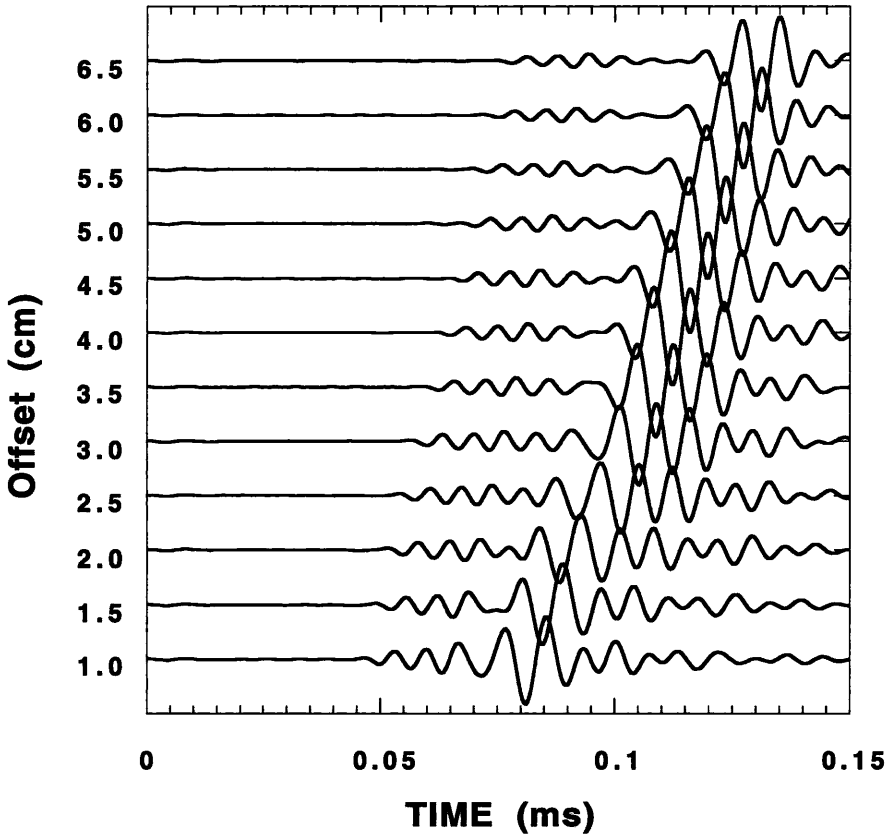

Figure 4-17: Ultrasonic lab measurement of dipole seismograms of a fluid-filled borehole drilled along the X axis in a phenolite solid (After Zhu et al., 1993).

Chapter 5

Field Acoustic Logs: Processing and Anisotropic Effect

5.1 Introduction

In the previous chapters we demonstrate that the 3-D finite difference method can provide reliable fluid-filled borehole wave propagation modeling in complex isotropic and anisotropic formations. The goal of the 3-D finite difference borehole modeling is to interpret field logging data, especially those can not be explained by the simple borehole model and are difficult to process.

In order to obtain information from borehole acoustic logging about the in-situ physical properties of subsurface formations, the common approach is to estimate formation P-wave velocity by picking the first arrival from conventional log data. Since the advance of full waveform logs, we can determine the S-wave velocity in fast formations by measuring the moveout of the shear-pseudo-Rayleigh wave packet. In slow formations this is not possible because there is no refracted shear-pseudo-Rayleigh arrival. One can estimate the shear wave velocity by inverting the Stoneley wave velocity (Cheng and Toksöz, 1983; Stevens and Day, 1986). More recently, the advance of direct shear wave logging using the flexural mode of the borehole makes

the direct measurement of shear wave velocity in slow formations possible (Zemanek et al., 1984).

There is additional information contained in the Stoneley waves such as the permeability of the formation (Rosenbaum, 1974; Schmitt et al., 1988). Williams et al. (1984) showed the strong correlation of in situ permeability with Stoneley wave velocity and attenuation. Since then several attempts have been made to obtain in situ permeability directly from full waveform acoustic logging data. Burns et al. (1988) applied the damped least square inversion to borehole Stoneley wave velocity and attenuation data to estimate in situ permeability. Stoneley wave dispersions were estimated from data collected by a tool with only two receivers. The forward model was based on the Biot-Rosenbaum model of wave propagation in a borehole in a porous formation (Biot, 1956a,b; Rosenbaum, 1974). The results were in reasonable agreement with the core measurements. The ultrasonic model laboratory experiments performed by Winkler et al. (1989) filled the gap between the Biot-Rosenbaum theory and field applications. The laboratory measured Stoneley wave velocity and attenuation in a permeable borehole were in excellent agreement with the predictions of the Biot-Rosenbaum model. Tang et al. (1991) formulated a simplified version of the Biot-Rosenbaum model dealing with the borehole Stoneley wave. It provides a clear physical picture of the propagation of the Stoneley wave in the permeable borehole.

Furthermore, anisotropy affects the different wavemodes differently. The phase velocities of the Stoneley wave are also affected by the mechanical properties of a transversely isotropic formation (White and Tongtaow 1981; Ellefsen 1990). In the case of a transversely isotropic formation with its symmetry axis parallel to the borehole, Stoneley wave phase velocity is sensitive to c_{66} at low frequency, and to c_{44} at high frequency. For a borehole normal to the axis of symmetry of a transversely anisotropic formation (creating a situation with azimuthal anisotropy), there is no analytic solution yet, but Ellefsen et al. (1991) have obtained numerical solutions for the phase velocity dispersion of the Stoneley wave by using the Finite Element Method.

A combination of monopole and dipole logs may allow us to further characterize the formation in terms of velocity anisotropy.

In this chapter we process data from two sections of a borehole where both the array sonic log and shear wave log are available. The P and S wave velocities of the formation are determined by threshold detection. The array data are processed using the Extended Prony's method to estimate the borehole Stoneley wave phase velocity and attenuation as a function of frequency. These are then inverted using the damped least-square method with Stoneley wave amplitude as a weighting function. Inverted shear wave velocities and permeabilities are compared with the shear wave log and the core permeability respectively. The 3-D finite difference simulations are used as an integrated interpretation of the field data set.

5.2 Data Analysis and Inversion

5.2.1 Tool geometry

The array monopole sonic logging data are collected by the ARCO array sonic tool with 12 receivers and two sources. The distance between successive receivers is 6 inches. There are 512 points recorded at each receiver with a sampling rate of 11 μs. There is a 25 μs time delay between each trace. Shear wave logging data are collected by the ARCO dipole shear wave logging tool with two receivers located at 9 and 13.5 ft from the source. There are 1024 data points recorded at each receiver with a sampling rate of 11 μs. The tools collect data every half foot along the borehole. Figure 5-1 shows an iso-offset plot of the array monopole data through a section of the well. The P-wave arrival and the low frequency Stoneley wave can be easily identified on the plot. Figure 5-2 shows the waveforms recorded at the near receiver of the shear wave tool. The shear/flexural mode arrival can be easily identified.

5.2.2 Data processing

The array monopole sonic and shear wave data are processed first to determine the formation P- and S-wave velocities. In both cases the first arrivals are picked by threshold detection and then the picks are correlated across different receiver waveforms to pick the maximum correlation in the first arrival waveform between receivers. The formation P- and S-wave velocities are determined this way from the array monopole and shear wave logs, respectively.

Next, the array monopole sonic data are processed by the Extended Prony's method to estimate borehole Stoneley wave phase velocity and attenuation (Lang et al., 1987; Ellefsen et al., 1989). This method transforms the data from the time domain into the frequency domain and then, at each frequency, the spectral data at each receiver is fitted to a propagating wave mode (pseudo-Rayleigh or Stoneley) of the following form:

$$A(\omega)e^{-\alpha(\omega)z}e^{i(\phi(\omega)+k(\omega)z)} \tag{5.1}$$

where ω = angular frequency

k = wavenumber of the propagating mode

z = distance between source and receiver.

$A(\omega)$ = amplitude of the incident wave at the first receiver

$\phi(\omega)$ = phase of the incident wave at the first receiver

$\alpha(\omega)$ = attenuation coefficient of the propagating mode

In this way, we can find the $A(\omega)$, $k(\omega)$, and $\alpha(\omega)$ which best fit the data by means of a least squares algorithm. The phase velocity is given by

$$c(\omega) = \frac{\omega}{k(\omega)}. \tag{5.2}$$

The attenuation coefficient, α, is sometimes alternately expressed as the imaginary part of the wavenumber k. Using the Extended Prony's method, the velocity disper-

sion and attenuation of the Stoneley wave as a function of frequency can be easily determined. The Stoneley wave velocity and attenuation data obtained here are the input data for the inversion.

5.2.3 Damped least-squares inversion

The inversion problem can be set up using the Taylor expansion as:

$$D_i^o = D_i^c + \sum_{j=1}^{M} \frac{\partial D_i^c}{\partial P_j} \Delta P_j + O(\Delta P_j^2) \qquad (i = 1, 2, ..., N) \tag{5.3}$$

where D_i^o are observed data and D_i^c are calculated data with the initial model P_{jo}. P_j are parameters which describe the model. In our problem the observed data D_i^o consist of Stoneley wave velocity and attenuation estimated from the Prony's method analysis of the array waveform data. The inversion parameters can be shear wave velocity, or permeability, depending on what borehole model we used to do the inversion. The i represents the different frequencies with a total of N frequency points. The total number of inversion parameters is M. Here we approximate the partial derivatives in Equation (5.3) by solving the period equation for the Stoneley wave for small changes in the parameters and then use finite differences in the resulting phase velocity and attenuation.

Equation (5.3) can be linearized by dropping the $O(\Delta P_j^2)$ term and rewritten in a compact form:

$$\mathbf{Ax} = \mathbf{b}. \tag{5.4}$$

The damped least-square solution of (4) is given by:

$$\mathbf{x} = (\mathbf{A}^T\mathbf{A} + \varepsilon^2\mathbf{I})^{-1}\mathbf{A}^T\mathbf{b} \tag{5.5}$$

where ε^2 is the damping factor and $\mathbf{I}$ an identity matrix. The superscript T stands for transposition. The damping factor suppresses the contribution of eigenvectors of matrix $\mathbf{A}^T\mathbf{A}$ whose eigenvalues are less than ε^2 (Aki and Richards 1980). The new value of P_j is

$$P_j = P_{jo} + \Delta P_j \tag{5.6}$$

the above equation gives us only an estimate of P_j, since we have linearized the inverse problem. To improve the estimate we use P_j as a new initial model and iterate the procedure until we obtain a satisfactory fit to the observations. Meanwhile at each iteration we reduce the damping factor ε. In this inversion procedure we can also make use of the amplitude information obtained from the data processing. The normalized amplitudes are used as a weighting function at different frequencies. The phase velocity and attenuation of the Stoneley wave at frequencies with large amplitudes are more reliable than those with small amplitudes.

One parameter of interest is formation permeability. The range of its magnitude is about a factor of 10^4 from core measurements. Here we adopt a logarithmic parameterization scheme in both the data and the model space to set up our inverse problem (Madden 1990). Our original inversion problem consists of a set of linear equations (5.3) and update equations (5.6). With logarithmic parameterization we have

$$\sum_{j=1}^{M} \frac{P_j \partial D_i}{D_i \partial P_j} \Delta \ln P_j = \ln \frac{D_i^o}{D_i}. \tag{5.7}$$

The new value of P_j is

$$P_j = P_{jo} \exp(\Delta \ln P_j). \tag{5.8}$$

One advantage of the logarithmic parameterization scheme is its ability to deal with large changes in the parameters in one iteration. In this case, changes in the permeability of one order of magnitude will only result in a change of unity in the actual parameter vector. This parameterization really helps in stabilizing the inversion and speeds up the convergence.

5.3 Results and Discussions

5.3.1 Isotropic borehole model

This is the simplest borehole model. The fluid-filled borehole of radius R_0 is embedded in an isotropic solid formation and extends to infinity. The borehole is filled with a fluid of velocity V_f and density ρ_f. The compressional wave velocity of the formation is V_p, shear wave velocity V_s, and density ρ_s. The attenuation of the Stoneley wave is controlled by the quality factor of the fluid Q_f and of the formation shear wave Q_s.

The above described procedures of the data processing and inversion are applied to our two data sets using the isotropic borehole model. The borehole radius is 12.2 cm from the caliper log. The fluid compressional wave velocity is taken to be 1.5 km/s. Fluid and formation density are taken to be 1.1 g/cm^3 and 2.15 g/cm^3, respectively. The borehole fluid attenuation Q_f, formation P-wave attenuation Q_p, and S-wave attenuation Q_s, are obtained by trial and error to fit Stoneley wave attenuation data from 2.0 kHz to 3.0 kHz. They are 20, 50, and 25 respectively. The inversion parameter is the formation shear wave velocity. Data used in the inversion are the Stoneley wave phase velocities between 1.5 kHz and 3.0 kHz. The Stoneley wave amplitudes are normalized and used as a weighting function in the damped least-squares inversion. The formation P-wave velocity (V_p) is obtained directly from first arrivals of array data. The initial value of shear velocity is taken to be $V_p/1.7$.

The first data set is the data collected between depths of 2950 ft and 3150 ft. Inverted shear wave velocities are shown in Figure 5-3. The shear wave velocity from the dipole shear wave tool and the P-wave velocities from the array sonic tool are also shown in the figure. There is an excellent agreement between the inverted shear wave velocities and the shear wave velocities from the dipole tool. This agreement comes from the fact that in the slow formation the Stoneley phase velocity is very sensitive to the formation shear wave velocity. Also this simple isotropic borehole model provides a very good approximation to the real well.

The second data set is the data collected in the same borehole lower down at between depths of 3650 ft and 3850 ft. The interval consists of a shale cap section (at around 3690 ft) overlying a fractured and porous permeable sand (about 3700 ft to 3800 ft). The inverted formation shear wave velocity, dipole measured shear wave velocity, and the formation P-wave velocity are plotted in Figure 5-4. In this data set there is one section in the sand (3715 ft to 3780 ft) in which the inverted shear wave velocities disagree with the dipole shear wave velocities. This disagreement is beyond the errors in the measurements. The rest of this chapter is devoted to explain this discrepancy.

The inverted shear wave velocity is lower than the dipole shear velocity. The core samples indicate a high permeability (1 to 10 darcies) zone in this section. So our isotropic solid borehole model is not correct. The question then becomes: can the high permeability account for this difference in the shear wave velocities? This leads to our next model.

5.3.2 Porous borehole model

Propagation of the Stoneley wave in a fluid-filled borehole surrounded by a porous formation becomes more complicated but more interesting. Biot(1956 a,b) proposed a theory of wave propagation in fluid-filled porous media. Rosenbaum (1974) applied the Biot model to the borehole geometry. The permeable borehole formation causes the Stoneley wave phase velocity to decrease and attenuation to increase, especially at low frequencies. This seems a good model to solve the shear wave velocity discrepancy for the second data set.

We consider a model of the borehole surrounded by a porous medium. We use the Stoneley wave phase velocity and attenuation at 530 Hz as the input data for the inversion and permeability as the inversion parameter. In the inversion we assume the open borehole wall condition. The inversion results of permeability from the Biot-Rosenbaum model are plotted against the core measurements in Figure 5-5. There is

a good agreement between the two permeabilities. The inverted permeabilities clearly show the low and the high permeable zones. Inverted permeabilities also show the trend of the core measurements.

Once the formation permeability is obtained, we can use the Biot-Rosenbaum borehole model to reinvert formation shear wave velocity. The same 1.5 kHz to 3.0 kHz Stoneley wave velocity data are used as input. In Figure 5-6 we plotted the inverted V_s from the porous and elastic models as a function of depth, as well as the V_s from the dipole tool. The plot shows that there is little effect of permeability on the inversion of formation shear wave velocity. This is because the permeability effect is restricted in the low frequency range and has little effect in our V_s inversion frequency range (1.5 kHz to 3 kHz). Also the shear wave velocity discrepancy zone is not completely aligned with the high permeability zone. So the permeability is not the cause of the disagreement of the inverted V_s and shear wave log V_s.

5.3.3 Anisotropic borehole model

A possible interpretation of the difference in the shear wave velocities from the two tools is formation anisotropy. In the permeable sand section, the problem is complicated. Here we have the dipole shear wave velocity higher than the inverted shear wave velocity, and the difference cannot be explained by the formation permeability. Our interpretation of this result is that the permeable formation is fractured (Gibson and Toksöz 1990). This fact was noted in the core description. Unfortunately no further description for the fractures was given. We are assuming that the fractures are subvertical, creating a situation where there is azimuthal anisotropy.

There is one check on the assumption of azimuthal anisotropy. In the array monopole data in the permeable zone (3700 ft to 3780 ft), there appears to be a "shear-pseudo-Rayleigh" wave arrival in front of the Stoneley wave (see Figure 5-1). Given the Stoneley wave velocity and the inverted shear wave velocity based on an isotropic elastic model, the formation is "slow" and there should not be a "shear-

pseudo-Rayleigh" arrival. From Chapter 4, we know that "shear-pseudo-Rayleigh" arrival can appear in slow formation due to shear wave anisotropy. So we estimated the phase velocity of this arrival using the semblance cross-correlation (Kimball and Marzetta, 1984; Block et al., 1991). The results are plotted in Figure 5-7 together with the dipole shear wave velocity and the inverted shear wave velocity from the Stoneley wave.

There are a couple of observations we can draw from Figure 5-7. If our hypothesis of azimuthal anisotropy is correct, then it appears that the observed arrival in the array sonic data does travel with the velocity of the fast shear wave velocity. Moreover, it gives the fastest shear wave velocity all along the fractured sandstone section. This is understandable since its frequency is around 6 kHz as opposed to the 2 kHz flexural wave generated by the dipole tool. Furthermore, this arrival travels with a velocity greater than the 1500 m/s, thus supporting the idea that this is some sort of a "refracted shear-pseudo-Rayleigh" arrival.

A second observation is that the dipole shear wave tool does not always measure the fastest shear wave velocity. It is evident that above 3710 ft the dipole is tracking the "slow" shear wave velocity while the "refracted shear" arrival in the array sonic is actually tracking the "fast" shear wave velocity in this fractured sandstone formation. Below 3710 ft the dipole shear wave log starts to track the "fast" arrival, although for the most part it is still a little slower than that from the array sonic, probably because of the lower frequency content. This also points out the importance of a combined integrated interpretation of both the array monopole sonic and the dipole log. Using only one or the other could lead to an erroneous interpretation.

Finally we support the assumption by using the 3D finite difference simulations developed in the previous chapters. The field array data from depth 3730 ft is plotted in Figure 5-8. The "refracted shear-pseudo-Rayleigh" is clearly shown in the last three traces between leaky P and low frequency Stoneley waves. In order to do the finite difference simulations we assume $c_{11} = c_{22} = c_{33}$, $c_{12} = c_{13} = c_{23} = c_{11} - 2c_{66}$ and

$c_{44} = c_{55}$. This is similar to transverse isotropy. The formation P wave velocity and the shear wave velocities from the shear wave log and Stoneley wave inversion are used to estimated these elastic constants. They are listed in Table 5.1. The borehole with radius 0.12 m is drilled along the Y axis. A Kelly source of center frequency 8.5 kHz is used. A $70 \times 530 \times 70$ grid is used in the calculation.

The finite difference synthetics are shown in Figure 5-9. The three phases on the synthetics are matched very well with the field data. The amplitude differences are due to the fact that there are no attenuations included in the finite difference calculations. The logging tool effect is also not considered. The synthetics are clearly demonstrated "refracted shear-pseudo-Rayleigh" arrivals. One of the shear wave velocities used in the simulation is greater than the borehole fluid velocity. This confirms that the "refracted shear-pseudo-Rayleigh" arrivals are due to the fastest shear wave velocity. So the shear wave discrepancy from the shear wave log and the Stoneley wave inversion is caused by the anisotropy. The symmetry axis of the anisotropy is perpendicular to the borehole axis instead of parallel to it. The shear wave anisotropy is about 10% to 20%.

5.4 Conclusions

Borehole Stoneley wave phase velocity and attenuation obtained from processing array monopole log data and shear wave velocity from the dipole log can be used together to estimate formation parameters. In an isotropic elastic borehole the inverted V_s from Stoneley wave phase velocity is in excellent agreement with the shear wave log result. Estimated formation permeabilities from low frequency Stoneley wave velocity and attenuation data are in good agreement with the core measurements. The shear wave velocity from the inverted Stoneley wave velocity can be used in combination with the dipole shear wave velocity and "refracted shear-pseudo-Rayleigh" wave arrival in the array sonic data to indicate formation shear wave anisotropy. These field

data examples also demonstrate that the 3D finite difference simulation can provide valuable information about field data interpretation in a complicated formation.

Quantity	Value
c_{11}	22.7 GPa
c_{12}	11.7 GPa
c_{13}	11.7 GPa
c_{22}	22.7 GPa
c_{23}	11.7 GPa
c_{33}	22.7 GPa
c_{44}	3.36 GPa
c_{55}	3.36 GPa
c_{66}	5.5 GPa
ρ	2150 kg/m^3

Table 5.1: Elastic properties used in the simulation of field logging data

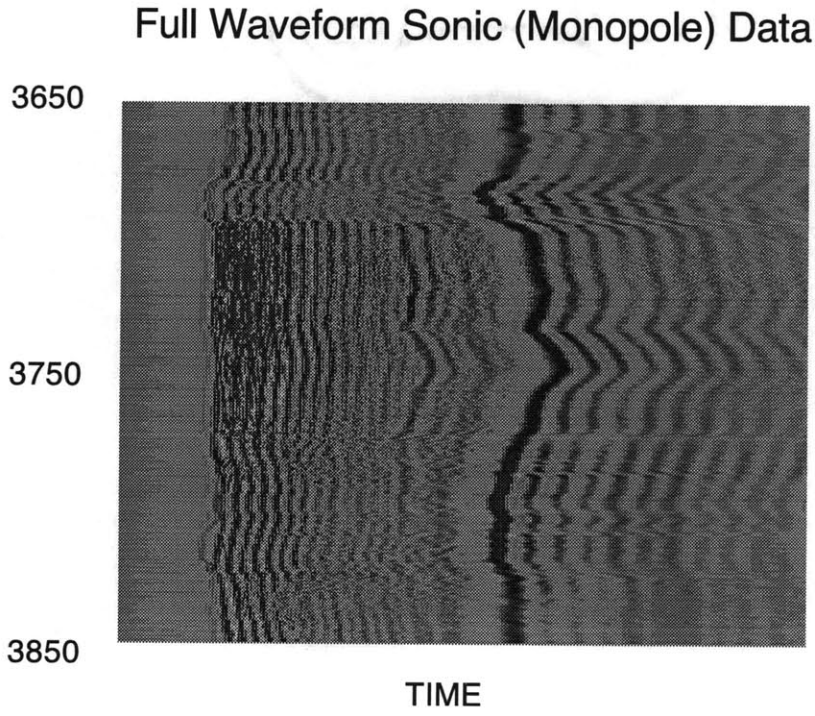

Figure 5-1: Iso-offset section of the array monopole sonic logging data from a section of the data set used in this study.

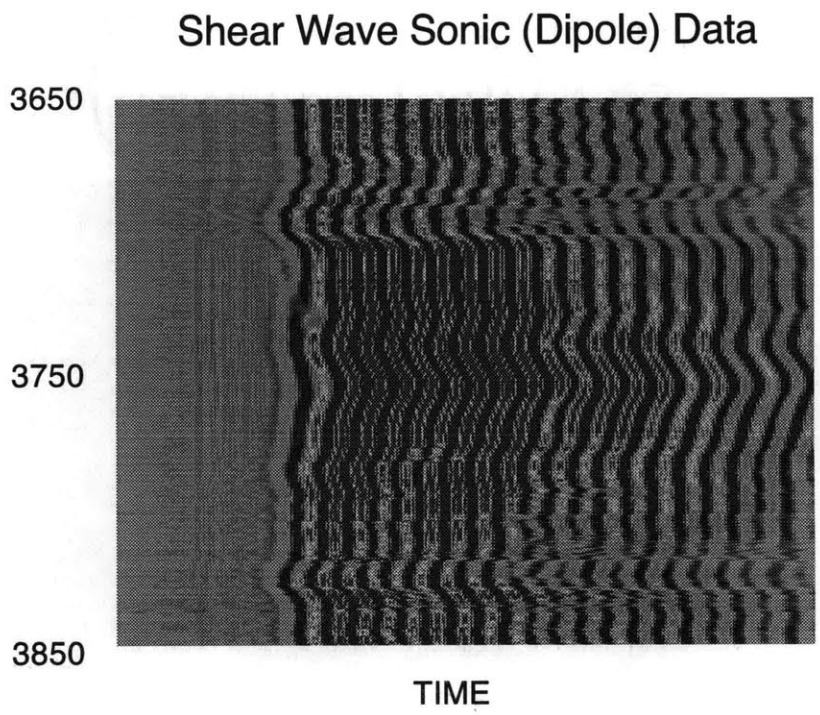

Figure 5-2: Iso-offset section of the shear wave logging data.

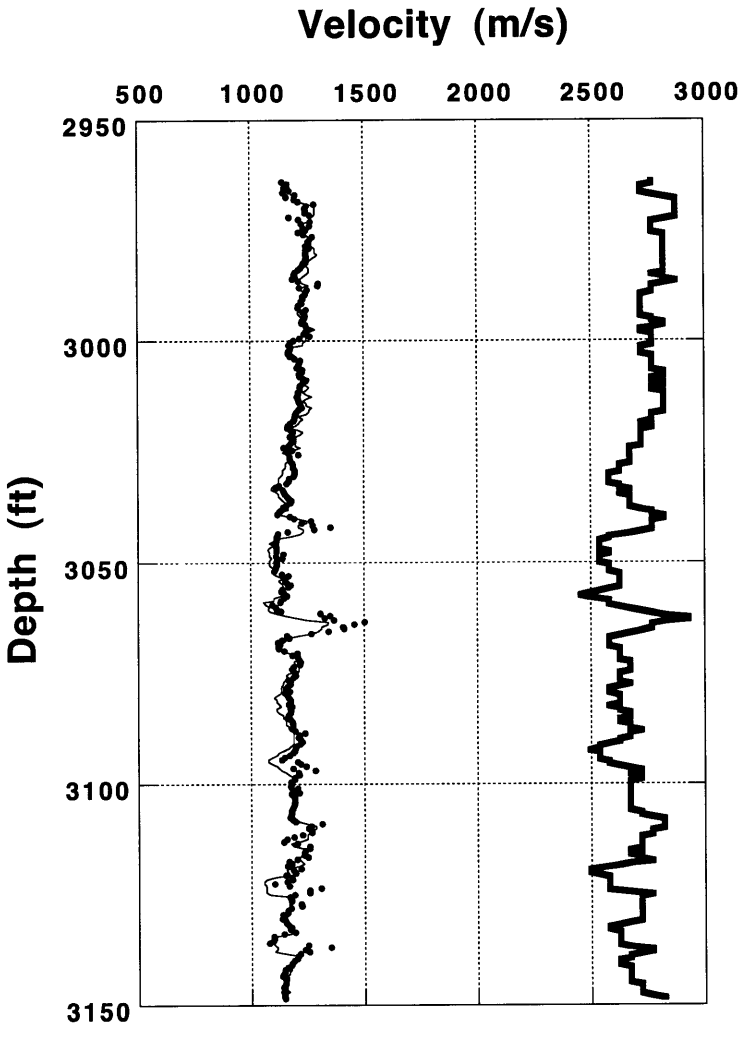

Figure 5-3: Inversion results for the upper portion of the borehole. The formation V_s from inverted Stoneley wave velocity (solid circles) is shown with the shear wave log V_s(thin line). The formation V_p (thick line) is also shown.

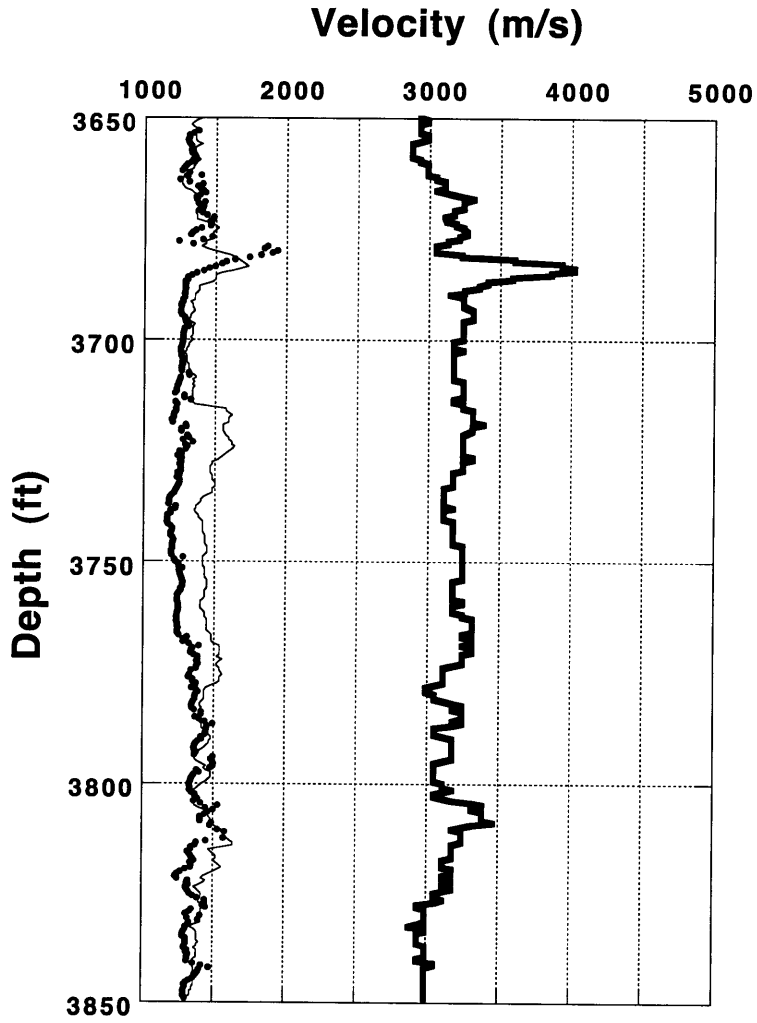

Figure 5-4: Inversion results for the lower portion of the borehole. The formation V_s from inverted Stoneley wave velocity (solid circle) is shown with the shear wave log V_s(thin line). The formation V_p (thick line) is also shown.

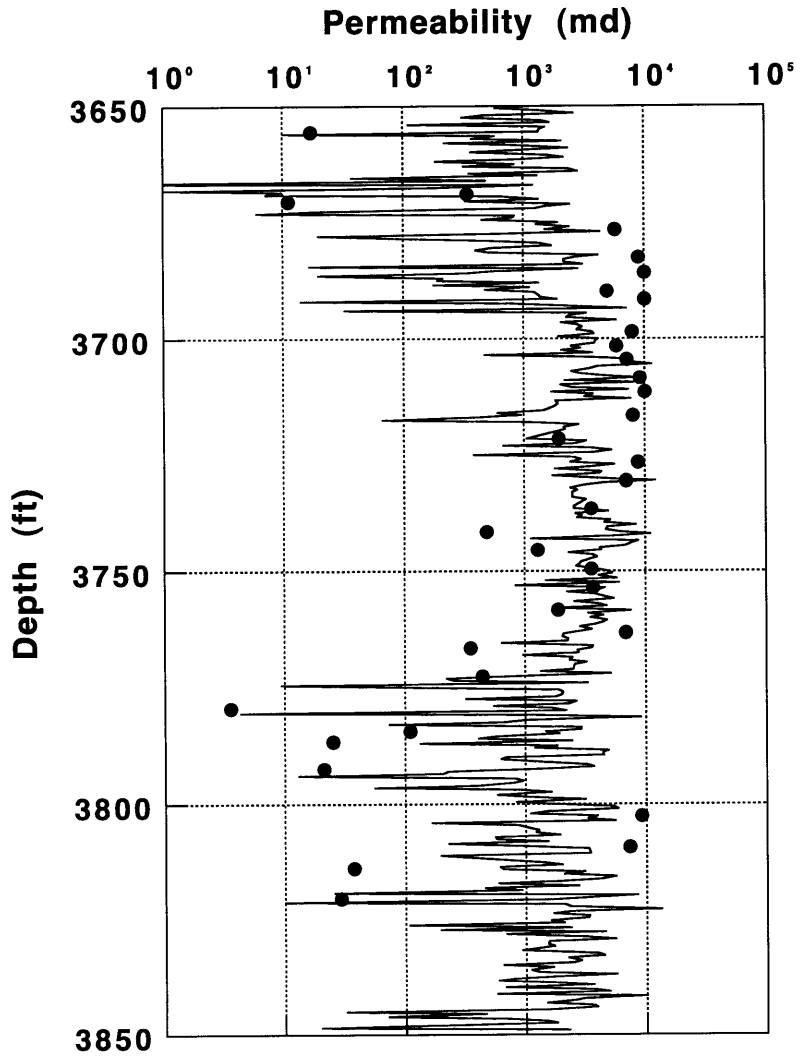

Figure 5-5: Inverted permeability using the Biot-Rosenbaum model (solid line) versus core measurements (open circles).

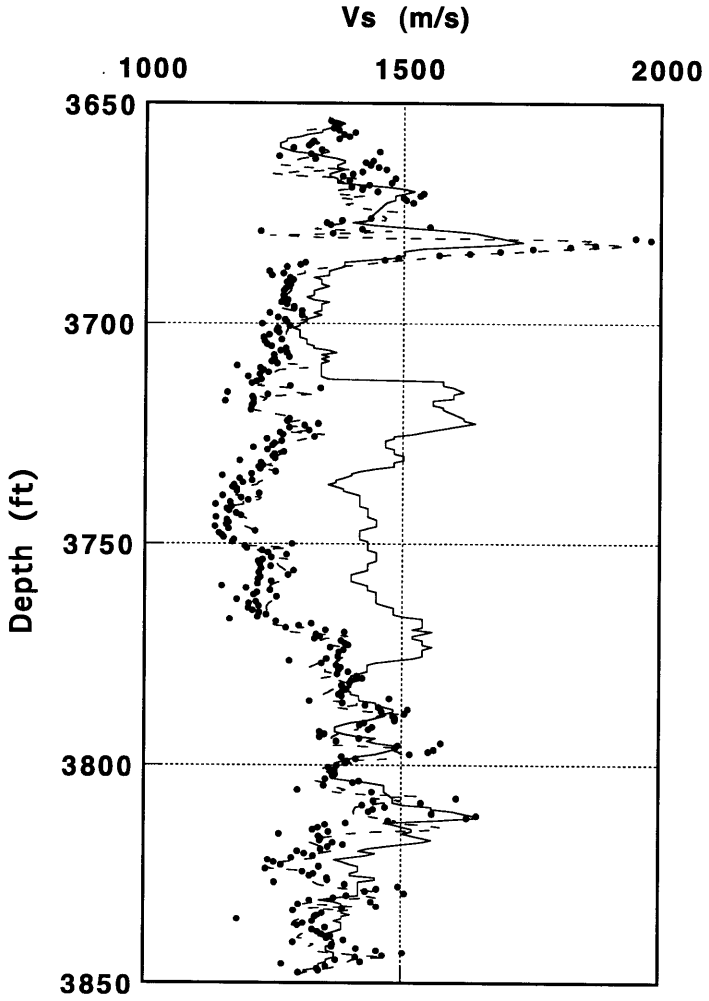

Figure 5-6: Inversion results for the formation V_s from the porous formation model (solid circles) and the elastic model compared with shear wave log V_s (solid line). The formation V_s inverted from elastic borehole model (dash line) is also shown.

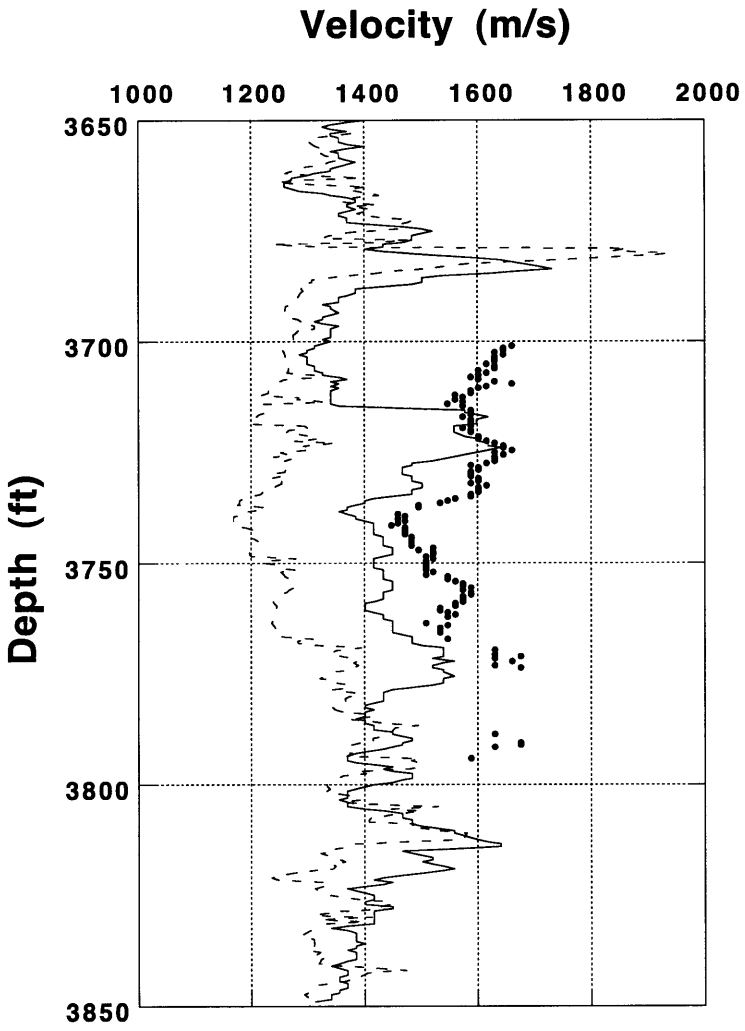

Figure 5-7: Shear wave velocity determined from inverted Stoneley wave velocity as compared with V_s from the dipole tool and the velocity from the "refracted shear/pseudo-Rayleigh" arrival in the array sonic data.

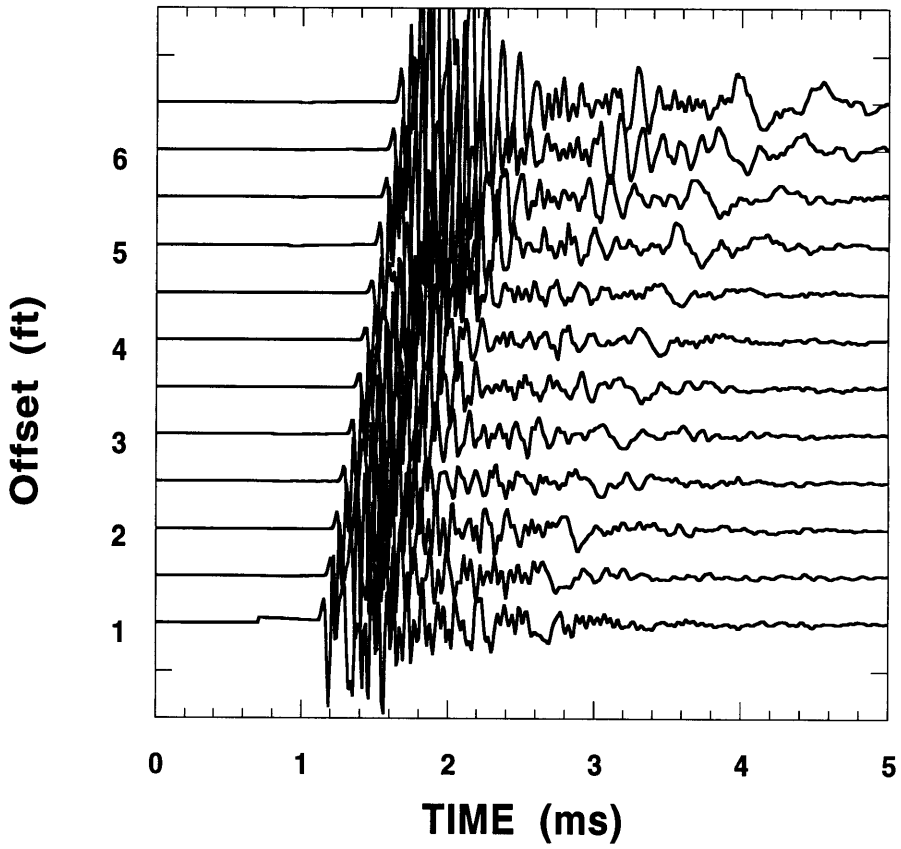

Figure 5-8: Field array sonic tool data from depth 3730 ft. There are 12 traces.

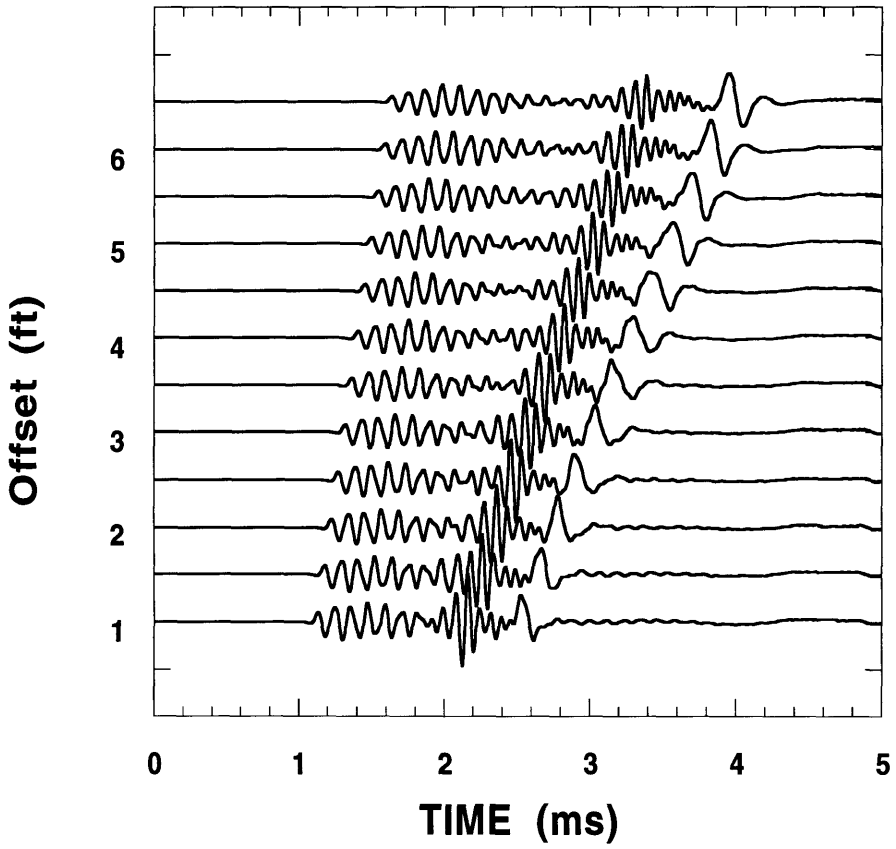

Figure 5-9: 3D finite difference synthetics for array sonic logging at depth 3730 ft. The source center frequency is 8.5 kHz.

Chapter 6

Summary and Conclusions

In this thesis we developed a three-dimensional finite difference method to simulate wave propagation in isotropic as well as anisotropic media. The 3-D finite difference scheme is second order accuracy in time and fourth order accuracy in space. The finite difference is performed on a staggered grid. The sharp interior boundaries are treated automatically. The grid dispersion and the grid anisotropy are analyzed and the stable condition is obtained. As a rule of thumb five samples per wavelength are needed to control the grid dispersions. The Higdon's absorbing boundary condition is discussed and generalized. It works well in isotropic as well as anisotropic media. It can absorb the body waves and the guided waves. The scheme can model realistic 3-D wave propagation problems by utilizing a parallel computer.

For wave propagations in the homogeneous media, the finite difference results agree excellently with the analytic solutions of the point source in acoustic, elastic, and transversely isotropic elastic media. The finite difference method accurately model not only the far field P and S waves but also the near field term in the elastic case.

The 3-D finite difference method applies to the fluid-filled borehole wave propagation in the isotropic formation. We reach the following conclusions:

1. The finite difference synthetics of monopole and dipole logs in the fluid-filled

borehole embedded in a homogeneous formation agree well with the discrete wavenumber results. Both hard and soft formation are tested.

2. The off-centered dipole sources generate almost the same waveforms as the centered dipole source. The off-centered monopole generates larger Stoneley waves than the centered monopole source.

3. In the elliptic borehole, the dipole source, which is in line with the minor axis of ellipse, generates similar waveforms to the dipole in the circular borehole with a radius same as the minor radius of the ellipse. The odd flexural mode is insensitive to the major radius. The dipole source, which is in line with the major axis of the ellipse, generates the lower frequency, dispersive waveforms. The waveforms are dominated by the even flexural mode.

4. For the borehole near the horizontal bed, the refracted P waves from the bed boundary can be used to detect it, but this refracted P wave is affected by the tool positions in the borehole and the distance between the borehole and the bed. Because the dipole is a directional source, when it is parallel to the bed, there is little effect from the bed on the waveforms. But when the dipole is perpendicular to the bed, there are strong flexural wave interferences. The amplitudes vary strongly with the offsets.

5. For the borehole that penetrates a 45 degree tilted layer boundary, the monopole log has less reflection and transmission than the horizontal boundary. The dipole log also transmits less flexural waves across the boundary than the horizontal one. In the horizontal layered formation the seismograms clearly show the two flexural modes in the two layers. There are no clear flexural wave reflections from the titled and horizontal interfaces.

The 3-D finite difference method is applied to the fluid-filled borehole wave propagation in the anisotropic formation. We reach the following conclusions:

1. In the borehole drilled along the Z axis in a phenolite formation, the monopole log shows the P wave traveling with velocity v_{zz}. There are no shear-pseudo-Rayleigh wave arrivals. The dipole log is dominated by the single flexural mode.

2. In the borehole drilled along the Y axis in a phenolite formation, the monopole log shows the P wave traveling with velocity v_{yy}. There are shear-pseudo-Rayleigh wave arrivals shown on the monopole seismograms between P and Stoneley wave arrivals due to shear wave anisotropy. The anisotropy also causes the shear wave splitting in the dipole log. There are two shear wave arrivals corresponding to the fast and slow flexural modes.

3. In the borehole drilled along the X axis in a phenolite formation, the monopole log shows the P wave traveling with velocity v_{xx}. There are shear-pseudo-Rayleigh wave arrivals on the monopole seismograms. The dipole log shows the shear wave splitting. The monopole and the dipole finite difference synthetics agree well with the ultrasonic lab measurements from the scaled borehole model.

After the applications of the 3-D finite difference method to synthetic borehole wave propagation problems, the field data sets collected by ARCO's array monopole acoustic logging tool and shear wave logging tool are processed and interpreted. The P- and S-wave velocities of the formation are determined by threshold detection with cross-correlation correction from the full waveform and the shear wave log, respectively. The array monopole acoustic logging data are also processed by using the Extended Prony's method to estimate the borehole Stoneley wave phase velocity and attenuation as a function of frequency. we reach the following conclusions for the field data sets:

1. The first data set was is collected between depths of 2950 and 3150 ft. The inverted V_s from the Stoneley wave phase velocity is in excellent agreement with the shear wave log results. This section of the well can be described as a fluid filled borehole surrounded by an isotropic elastic formation.

2. The second data set was collected between the depth of 3650 ft and 3850 ft. There is a major shear wave velocity discrepancy zone between 3715 and 3780 ft. The shear wave velocity from the Stoneley wave inversion is lower than the direct shear wave log velocity. Estimated permeabilities from low frequency Stoneley wave velocity and attenuation data are in good agreement with the core measurements. Also it is proven that the formation permeability is not the cause of the discrepancy. From the estimated "shear/pseudo-Rayleigh" phase velocities in the array monopole log and 3D finite difference synthetics in anisotropic formation, the discrepancy can be explained as shear wave anisotropy. The well between depths of 3715 ft and 3780 ft can be described as a fluid filled borehole surrounded by porous formation, with shear wave velocity anisotropy about 10 to 20% and a symmetry axis perpendicular to the borehole axis.

It has been emphasized in this thesis how to simulate the three-dimensional effects of borehole geometry, such as elliptic borehole and tilted layering, and the effects of formation anisotropy on borehole wave propagation. Full waveform acoustic log can be obtained for complex borehole environment by using 3-D finite difference method on a parallel computer. The method is very simple in concept and execution. However, it is remarkably robust.

6.1 Future Work

The synthetic logs from 3-D borehole environments and anisotropic formations can help design new acoustic logging tools, for example a dipole logging tool to effectively detect the formation shear wave anisotropy and the orientations of its direction. It can be also used to test new logging data processing methods and software. In this thesis we only applied the 3-D finite difference method to the borehole wave propagation problem. But the method developed here is not restricted to the borehole problems. The seismic wave propagation problems can be directly applied to, for example, to

the effects of 3-D structures near the earthquake sources and the observation stations and to the seismic wave scattering problems. This thesis was the first step towards simulating wave propagation in isotropic and anisotropic media in three-dimensional space. There are a lot of research areas that can be pursued in this direction.

A frequency dependent finite difference method is in one direction. The finite difference method developed here is restricted to perfect elasticity. The intrinsic attenuation of wave energy is neglected. In frequency domain methods, such as the discrete wavenumber method, it is no problem to incorporate attenuation into the calculations. It is done simply by making the elastic moduli complex functions of frequency. On the other hand in time domain methods, such as the finite difference method, it is almost impossible to incorporate general attenuation laws because in the time domain the anelastic stress-strain relation has the form of a convolution integral. It is intractable in a numerical computation. Another related problem is wave propagation in porous media. Biot's theory (1956a,b) is developed for macroscopic dynamic behavior. In that theory, the wave equation coefficients are frequency dependent. The rational function approximation has been used to incorporate attenuation into the time domain method (Day and Minster 1984; Emmerich and Korn 1987). A systematic approach and efficient numerical scheme are needed for solving realistic problems

Another interesting area is the multigrid algorithm. This scheme allows for some regions of interest (such as a strong heterogeneity area) to be finely gridded while other regions are coarsely gridded. The fine grids are connected to the coarse grids. This will make the computation of large models very efficient. It will open doors for simulations such as the wave propagation near a fracture zones and cross borehole type experiments. A related problem is to investigate a better treatment for the smooth curved surfaces than through the use of "stair-stepped" orthogonal approximations. There are two approaches to solving the problem. The first one is to preserve the basic Cartesian grid at all space cells except those adjacent to the structure surface. Space

cells adjacent to the surface are deformed to conform with the structure. The other is to construct non-Cartesian grids which are continuously and globally stretched to conform with smoothly shaped structure. These approaches need to be closely examined, especially in the three-dimensional structure case.

Appendix A

Source Time Function

The source time function used in this thesis is based on a Gaussian curve (Kelly et al., 1976; Stephen et al., 1985).

$$f(t) = -2\xi T e^{-\xi T^2} \tag{A.1}$$

where ξ is a pulse width parameter and $T = t - t_s$. t_s is a time shift parameter.

It is straight forward to obtain the first and the second order derivatives of $f(t)$, which is given below:

$$f'(t) = -2\xi(1 - 2\xi T^2)e^{-\xi T^2} \tag{A.2}$$

$$f''(t) = 4\xi^2(3T - 2\xi T^3)e^{-\xi T^2} \tag{A.3}$$

For a pulse at center frequency F_0 we chose pulse width parameter $\xi = \frac{F_0^2}{0.1512}$. t_s is selected such that $f(0) \simeq 0$. Here we chose $t_s = \frac{1.5}{F_0}$.

In the finite difference calculation when the source time function is fed into the stress $f'(t)$ is used to simulate a point explosion and when the source time function is fed into the velocity $f''(t)$ is used to simulate a point force.

Appendix B

A Point Force Solution in a Homogeneous Elastic Medium

This appendix presents the solution of a point force in a homogeneous elastic medium (Aki and Richard 1980). In Cartesian coordinates $x_i (i = 1, 2, 3)$, a point force $X_0(t)$ is applied in the x_j direction at the origin, the displacement u_i can be written as

$$\begin{aligned} u_i(x,t) &= \frac{1}{4\pi\rho}(3\gamma_i\gamma_j - \delta_{ij})\frac{1}{r^3}\int_{r/\alpha}^{r/\beta} \tau X_0(t-\tau)d\tau \\ &+ \frac{1}{4\pi\rho\alpha^2}\gamma_i\gamma_j\frac{1}{r}X_0(t-\frac{r}{\alpha}) \\ &- \frac{1}{4\pi\rho\beta^2}(\gamma_i\gamma_j - \delta_{ij})\frac{1}{r}X_0(t-\frac{r}{\beta}) \end{aligned} \tag{B.1}$$

where direction cosines γ_i for vector $\vec{x} = (x_1, x_2, x_3)$ is $\gamma_i = \frac{x_i}{r}$, r is the distance from source to receiver $r = \sqrt{x_1^2 + x_2^2 + x_3^2}$.

In the above equation the first term is called the near-field term. It behaves like $\frac{1}{r^2}$ for sources in which X_0 is nonzero from times that are short compared to $\frac{r}{\beta} - \frac{r}{\alpha}$. It dominates in the equation as $r \to 0$. It consists of both P-wave and S-wave motions. For a force time function, nonzero from 0 to T, the near-field term arrives at P wave arrival time $\frac{r}{\alpha}$ and remains active until the time $\frac{r}{\beta} + T$.

The second term is called the far-field P wave term. It behaves like $\frac{1}{r}$. The particle motion is the same as the direction of propagation. The third term is called the far-field S wave term. It also behaves like $\frac{1}{r}$. Its particle motion is normal to the direction of propagation. The far-field terms dominate as $r \rightarrow \infty$.

Appendix C

A Point Force Solution in a Transversely Isotropic Solid

We consider the solution along the symmetry axis of a transversely isotropic solid. This analytic solution is given by Payton (1983). Define the following dimensionless parameters:

$$\begin{aligned} a &= \frac{c_{33}}{c_{44}} \\ b &= \frac{c_{11}}{c_{44}} \\ d &= \frac{1}{2}(b - \frac{c_{12}}{c_{44}}) \\ e &= 1 + ab - (\frac{c_{13}}{c_{44}} + 1)^2 \\ v_s &= \sqrt{\frac{c_{44}}{\rho}} \\ \bar{z} &= \frac{z}{v_s t} \end{aligned} \tag{C.1}$$

where $c_{11}, c_{12}, c_{13}, c_{33}$ and c_{44} are elastic constants. ρ is density. z is the distance from the source along the symmetry Z axis.

The response to the vertical force:

$$\vec{f} = (0, 0, 1)\delta(x)\delta(y)\delta(z)H(t) \tag{C.2}$$

where H(t) is the step function, is given by:

$$
\begin{aligned}
u_x &= 0 \\
u_y &= 0 \\
u_z &= \frac{1}{4\pi z v_s^2} \begin{cases} 0, & 0 < t \leq t_p \\ h(\bar{z}), & t_p < t \leq t_s \\ 2h(\bar{z}), & t_s < t \leq t_1 \\ 1, & t > t_1 \end{cases}
\end{aligned} \tag{C.3}
$$

where

$$
h(\bar{z}) = \frac{1}{2} - \frac{2(1-\bar{z}^2) - e + (b+1)\bar{z}^2}{2\sqrt{D}} \tag{C.4}
$$

with

$$
\begin{aligned}
t_s &= \frac{z}{v_s} \\
t_p &= \frac{z}{\sqrt{c_{33}/\rho}} \\
t_1 &= \frac{t_s}{\bar{z}_1}
\end{aligned} \tag{C.5}
$$

The quantity D and $\bar{z}_1$ is given by:

$$
D(\bar{z}) = [e - (b+1)\bar{z}^2]^2 - 4b(a - \bar{z}^2)(1 - \bar{z}^2) \tag{C.6}
$$

and

$$
\bar{z}_1 = [e(b+1) - 2b(a+1) + 2\sqrt{b(1+ab-e)(a+b-e)}]^{\frac{1}{2}}/(b-1) \tag{C.7}
$$

The above solution is valid for the solid satisfying the inequalities ($e < 1 + b$) and ($e^2 - 4ab < 0$). In our application the time step function is removed in the frequency domain and the source time function described in Appendix A is convolved.

Appendix D

Plane Wave Solutions of an Orthorhombic Solid

The plane wave solution of an orthorhombic solid is given by Auld (1973). In the XY plane there is a pure shear wave polarized along the Z axis,

$$v_s^2 = \frac{c_{44}cos^2\phi + c_{55}sin^2\phi}{\rho} \tag{D.1}$$

the quasi-S wave is,

$$v_{qs}^2 = \frac{c_{66} + c_{11}cos^2\phi + c_{22}sin^2\phi - \sqrt{(c_{66} + c_{11}cos^2\phi + c_{22}sin^2\phi)^2 - 4C}}{2\rho} \tag{D.2}$$

and the quasi-P wave is,

$$v_{qp}^2 = \frac{c_{66} + c_{11}cos^2\phi + c_{22}sin^2\phi + \sqrt{(c_{66} + c_{11}cos^2\phi + c_{22}sin^2\phi)^2 - 4C}}{2\rho} \tag{D.3}$$

where

$$C = (c_{11}cos^2\phi + c_{66}sin^2\phi)(c_{66}cos^2\phi + c_{22}sin^2\phi) - (c_{12} + c_{66})^2cos^2\phi sin^2\phi \tag{D.4}$$

where ϕ is the angle between propagation direction and X axis.

For propagation in the XZ plane the pure shear wave is polarized along the Y axis,

$$v_s^2 = \frac{c_{44}cos^2\theta + c_{66}sin^2\theta}{\rho} \tag{D.5}$$

the quasi-S wave is

$$v_{qs}^2 = \frac{c_{55} + c_{33}cos^2\theta + c_{11}sin^2\theta - \sqrt{(c_{55} + c_{33}cos^2\theta + c_{11}sin^2\theta)^2 - 4D}}{2\rho} \tag{D.6}$$

and the quasi-P wave is,

$$v_{qp}^2 = \frac{c_{55} + c_{33}cos^2\theta + c_{11}sin^2\theta + \sqrt{(c_{55} + c_{33}cos^2\theta + c_{11}sin^2\theta)^2 - 4D}}{2\rho} \tag{D.7}$$

where

$$D = (c_{55}cos^2\theta + c_{11}sin^2\theta)(c_{33}cos^2\theta + c_{55}sin^2\theta) - (c_{13} + c_{55})^2cos^2\theta sin^2\theta \tag{D.8}$$

In the YZ plane the pure shear wave is polarized along the X axis,

$$v_s^2 = \frac{c_{55}cos^2\theta + c_{66}sin^2\theta}{\rho} \tag{D.9}$$

the quasi-S wave is

$$v_{qs}^2 = \frac{c_{44} + c_{33}cos^2\theta + c_{22}sin^2\theta - \sqrt{(c_{44} + c_{33}cos^2\theta + c_{22}sin^2\theta)^2 - 4E}}{2\rho} \tag{D.10}$$

and the quasi-P wave is,

$$v_{qp}^2 = \frac{c_{44} + c_{33}cos^2\theta + c_{22}sin^2\theta + \sqrt{(c_{44} + c_{33}cos^2\theta + c_{22}sin^2\theta)^2 - 4E}}{2\rho} \tag{D.11}$$

where

$$E = (c_{44}cos^2\theta + c_{22}sin^2\theta)(c_{33}cos^2\theta + c_{44}sin^2\theta) - (c_{23} + c_{44})^2cos^2\theta sin^2\theta \tag{D.12}$$

where θ is the angle between propagation direction and X axis.

References

Aki, K. and Richards, P.G. (1980). *Quantitative Seismology,* W. H. Freeman and Company.

Alford, R. M., Kelley, K. R., and Boore, D. M., 1974. Accuracy of finite difference modelling of the acoustic wave equations. *Geophysics, 39,* 834-842.

Alterman, Z. and Karal, F.C., 1968. Propagation of elastic waves in layered media by finite difference methods. *Bull. Seis. Soc. Am., 58,* 367-398.

Auld, B.A., 1973. *Acoustic Fields and Waves in Solids, Vol.1.* John Wiley & Sons, Inc.

Baker, L. J., 1984. The effect of the invaded zone on full wave train acoustic logging. *Geophysics, 49,* 796-809.

Bhashvanija, K., 1983, A finite difference model of an acoustic logging tool: the borehole in a horizontal layer geologic medium. *PhD Thesis,* Colorado School of Mines, Golden, CO.

Biot, M.A., 1952. Propagation of elastic waves in a cylindrical bore containing a fluid. *J. Appl. Phys. 23,* 977-1005.

Biot, M.A., 1956a. Theory of propagation of elastic waves in a fluid saturated porous rock: I. Low frequency range. *J. Acoust. Soc. Am., 28,* 168–178.

Biot, M.A., 1956b. Theory of propagation of elastic waves in a fluid saturated porous rock: II. Higher frequency range. *J. Acoust. Soc. Am., 28,* 179–191.

Block, L.V., Cheng, C.H. and Duckworth, G.L., 1991. Velocity analysis of multi-receiver full waveform acoustic logging data in open and cased holes. *The Log Analyst, 32,* 188–200.

Boore, D. M., 1972. Finite difference methods for seismic waves, Methods in computational physics, V. 11, Bolt, B. A., Ed., Academic Press Inc. 1-37.

Bouchon, M., 1993. A numerical simulation of the acoustic and elsatic wavefileds radiated by a source on a fluid-filled borehole embedded in a layered medium. *Geophysics, 58,* 475-481.

Bouchon, M. and Schmitt, D.P., 1989. Full-wave acoustic logging in an irregular borehole. *Geophysics, 54,* 758-765.

Burns, D.R., 1992. Acoustic and elastic scattering from seamounts in three dimensions - a numerical modeling study. *J. Acoust. Soc. Am., 92,* 2784-2791.

Burns, D.R., Cheng, C.H., Schmitt, D.P. and Toksöz, M.N., 1988. Permeability estimation from full waveform acoustic logging data. *The Log Analyst, 29,* 112–122.

Burns, D.R. and Stephen, R. A., 1990. Three-dimensional numerical modeling of geoacoustc scattering from seafloor topography. *J. Acoust. Soc. Am., 88,* 2338-2345.

Broeze, J. and Daalen, E.V., 1992. Radiation boundary conditions for the two-dimensional wave equation from a variational principle. *Math. Comp., 58,* 73-82.

Carcione, J. M., Kosloff, D., Behle, A. and Seriani, G., 1992. A spectral scheme for wave propagation simulation in 3-D elastic anisotropic media. *Geophysics, 57,* 1593-1607.

Chan, A. K. and Tsang, L., 1983. Propagation of acoustic waves in a fluid-filled borehole surrounded by a concentrically layered transversely isotropic formation. *J. Acoust. Soc. Am., 74,* 1605-1616.

Cheadle, S.P., Brown, R.J. and Lawton, D.C., 1991. Orthorhombic anisotropy: A physical seismic modelling study. *Geophysics, 56,* 1603-1613.

Cheng, C. H. and Toksöz, M. N., 1981. Elastic wave propagation in a fluid-filled borehole and synthetic acoustic logs. *Geophysics, 46,* 1042-1053.

Cheng, C.H., and Toksöz, M.N., 1983. Determination of shear wave velocities in "slow" formation. *Trans. SPWLA 24th Ann. Logging Symp.,* Calgary, Canada, Paper V.

Cheng, C. H., Zhang, J. and Burn, D. R., 1987. Effects of in-situ permeability on the propagation of Stoneley waves in a borehole. *Geophysics, 52,* 1279-1289.

Clayton, R. and Engquist, B., 1977. Absorbing boundary conditions for acoustic and elastic wave equations. *Bull. Seis. Soc. Am., 67,* 1529-1540.

Daalen, E.V., Broeze, J. and Groesen, E.V., 1992. Variational principles and conservation laws in the derivation for radiation boundary conditions for wave equations. *Math. Comp., 58,* 55-71.

Day, S.M. and Minster, J.B., 1984. Numerical simulation of attenuated wavefields using a Pade approximant method. *Geophys. J. R. astr. Soc., 78,* 105-118.

Ellefsen, K. J., 1990. Elastic wave propagation along a borehole in an anisotropic medium. *PhD Thesis*, Massachusetts Institute of Technology, Cambridge, MA.

Ellefsen, K.L., Cheng, C.H. and Toksöz, M.N., 1991. Effects of anisotropy upon the normal modes in a borehole. *J. Acoust. Soc. Am., 89,* 2597–2616.

Ellefsen, K.L., Cheng, C.H. and Tubman, K.M., 1989. Estimating phase velocity and attenuation of guided waves in acoustic logging data. *Geophysics, 54,* 1054–1059.

Emermen, S.H. and Stephen, R.A., 1983. Comment on, "Absorbing boundary conditions for acoustic and elastic wave equations," by R. Clayton and B. Engquist. *Bull. Seis. Soc. Am. 73,* 661-665.

Emmerich, H. and Korn, M., 1987. Incorporation of attenuation into time domain computations of seismic wave fields. *Geophysics, 52,* 1252-1264.

Frankel, A. and Vidale, J., 1992. A three-dimensional simulation of seismic waves in the Santa Clara Valley, California, from a Loma Prieta aftershock. *Bull. Seis. Soc. Am., 82,* 2045-2074.

Fuyuki, M. and Matsumoto, Y., 1980. Finite difference analysis of Rayleigh wave scattering at a trench. *Bull. Seis. Soc. Am. 67,* 2051-1067.

Gibson, R.L., and Toksöz, M.N., 1990. Permeability estimation from velocity anisotropy in fractured rock. *J. Geophys. Res., 95,* 15643-15655.

Higdon, R.L., 1986. Absorbing boundary conditions for difference approximations to the multi-dimensional wave equation. *Mathematics of Computation, 47,* 437-459.

Higdon, R.L., 1987. Numerical absorbing boundary conditions for the wave equation. *Mathematics of Computation, 49,* 65-90.

Higdon, R.L., 1990. Radiation boundary conditions for elastic wave propagation. *SIAM J. Numer. Anal., 27,* 831-870.

Igel, H, Mora, P. and Rodrigues, D., 1991. 3-D wave propagation using finite differences. *61st S.E.G Annual Meeting Expanded Abstracts,* Houston.

Igel, H, Riollet, B. and Mora, P., 1992. Accuracy of staggered 3-D finite difference grids for anisotropic wave propagation. *62nd S.E.G Annual Meeting Expanded Abstracts* New Orleans.

Israeli,M., and Orszag, S.A., 1981. Approximation of radiation boundary conditions. *J. Comput. Phys., 41,* 115-135.

Kelly, K.R., Ward, R.W., Treitel, S., and Alford, R.M., 1976. Synthetic seismograms: A finite-difference approach. *Geophysics, 41,* 2-27.

Kimball, C.V., and Marzetta, T.L., 1984. Semblance processing of borehole acoustic array data. *Geophysics, 49,* 274–281.

Kosloff, R. and Kosloff, D. 1986. Absorbing boundaries for wave propagation problems. *J. Comput. Phys., 63,* 363-376

Kostek, S., 1991. Modelling of elastic wave propagation in a fluid-filled borehole excited by a piezoelectric transducer. *Master Thesis,* Massachusetts Institute of Technology, Cambridge, MA.

Kurkjian, A. L. and Chang, S. K., 1986. Acoustic multipole sources in fluid-filled boreholes. *Geophysics, 51,* 1334-1342.

Lang, S.W., Kurkjian, A.L., McClellan, J.H., Morris, C.F. and Parks, T.W., 1987. Estimating slowness dispersion from arrays of sonic logging data. *Geophysics, 52,* 530–544.

Leslie, H. D. and Randall, C. T., 1992. Multipole sources in boreholes penetrating anisotropic formations: Numerical and experimental results. *J. Acoust. Soc. Am., 91,* 12-27.

Levander, A.R., 1988. Fourth-order finite difference P-SV seismograms. *Geophysics, 53,* 1425-1436.

Leveille, J. P. and Seriff, A. J., 1989. Borehole wave particle motion in anisotropic formations. *J. Geophys. Res., 94,* 7183-7188.

Liao, Z. P., Wong, H. L., Yang, B. and Yuan, Y., 1984 A transmitting boundary for transient wave analyses. *Scientia Sinica (series A), XXVII,* 1063-1076

Lindman, E.L., 1975. Free-Space boundary conditions for the time dependent wave equation. *J. Comput. Phys., 18,* 66-78.

Liu, H. and Randall, C. T. 1991. Synthetic waveforms in noncircular boreholes using a boundary integral equation method. *61st Ann. Internat. Mtg., Soc. Expl. Geophys., Expanded Abstracts.*

Luo, Y. and Schuster, G., 1990. Parsimonious staggered grid finite-difference of the wave equation. *Geophys. Res. Lett., 17,* 155-158.

Lysmer,J. and Kuhlemeyer, R.L., 1969. Finite dynamic model for infinite media. *J. Eng. Mech. Div., ASCE 95 EM4,* 859-877.

Madariaga, R., 1976. Dynamics of an expanding circular fault. *Bull. Seism. Soc. Am., 65,* 163-182.

Madden, T., 1990. Inversion of low-frequency electromagnetic data. *Oceanographic and Geophysical Tomography,* Desaubies, Y., Tarantola, A. and Zinn-Justin, J. eds., *Elsevier Science Publishers*

Nicoletis, L. M., Bamberger, J. A., Quiblier, P. J. and Kern, K., 1990. Hole geometry and anisotropic effects on tube-wave propagation: a quasi-static study. *Geophysics, 55,* 167-175.

Norris, A. N. and Sinha, B. K., 1993. Weak elastic anisotropy and the tube wave. *Geophysics, 58,* 1091-1098.

Paillet, F. L., and White, J. E., 1982. Acoustic modes of propagation in the borehole and their relationship to rock properties. *Geophysics, 47,* 1215-1228.

Payton, R. G., 1983. Elastic wave propagation in transversely isotropic media. *Martinus Nijhoff Publ.*

Peng, C., 1994. Borehole effects on downhole seismic measurements. *PhD Thesis,* Massachusetts Institute of Technology, Cambridge, MA.

Peterson, E.W., 1974. Acoustic wave propagation along a fluid-filled cylinder. *J. Appl. Phys., 45,* 3340-3350.

Randall, C.J., 1988. Absorbing boundary conditions for the elastic wave equation. *Geophysics, 53,* 611-624.

Randall, C.J., 1989. Absorbing boundary conditions for the elastic wave equation: velocity-stress formulation. *Geophysics, 54,* 1141-1152.

Randall, C. T., 1991. Modes of noncircular fluid-filled boreholes in elastic formation. *J. Acoust. Soc. Am., 89,* 1002-1016.

Randall, C. T., 1991. Multipole acoustic waveforms in nonaxisymmetric boreholes and formations. *J. Acoust. Soc. Am., 90,* 1620-1631.

Randall, C. T., Scheibner, D. J. and Wu, P. T., 1991. Multipole borehole acoustic waveforms: synthetic logs with beds and borehole washouts. *Geophysics, 56,* 1757-1769.

Renaut, R.A. and Petersen, J., 1989. Stability of wide-angle absorbing boundary conditions for the wave equation. *Geophysics, 54,* 1153-1163.

Renlie, L. and Raaen, A., 1993. Acoustic wave propagation in a fluid-filled borehole surrounded by a formation with stress-relief-induced anisotropy. *Geophysics, 58,* 1257-1269.

Reynolds, A.C., 1978. Boundary conditions for the numerical solution of wave propagation problems. *Geophysics, 43,* 1099-1110.

Rodrigues, D. and Mora, P., 1992. Analysis of a finite difference solution to 3-D elastic wave propagation. *62nd S.E.G Annual Meeting Expanded Abstracts.* New Orleans.

Rosenbaum, J. H., 1974. Synthetic microseismograms: logging in porous formations. *Geophysics, 39,* 14-32.

Schmitt, D. P., 1988. Shear wave logging in elastic formations. *J. Acoust. Soc. Am., 84,* 2215-2229.

Schmitt, D. P., 1989. Acoustic multipole logging in transversely isotropic poroelastic formations. *J. Acoust. Soc. Am., 86,* 2397-2421.

Schmitt, D. P., 1993. Dipole loggin in cased borehole. *J. Acoust. Soc. Am., 93,* 640-657.

Schmitt, D. P. and Bouchon, M., 1985. Full wave acoustic logging: synthetic microseismograms and frequency wavenumber analysis. *Geophysics, 50,* 1756-1778.

Schmitt, D.P., Bouchon, M. and Bonnet, G., 1988. Full-wave synthetic acoustic logs in radially semi-infinite saturated porous media. *Geophysics, 53,* 807–823.

Schoenberger, M., Marzetta, T., Aron, J., and Porter, R., 1981. Space-time dependence of acoustic waves in a borehole. *J. Acoust. Soc. Am., 70,* 1496-1507.

Sinha, B. K., Norris, A. N. and Chang, S. K., 1991. Borehole flexural modes in anisotropic formations. *61st S.E.G Annual Meeting Expanded Abstracts.* Houston.

Smith, W.D., 1974. A nonreflecting plane boundary for wave propagation problems. *J. Comput. Phys., 15,* 492-503.

Stacey, R., 1988. Improved transparent boundary formulations for the elastic-wave equation. *Bull. Seis. Soc. Am., 78,* 2089-2097.

Stephen, R.A., Cardo-Casas, F. and Cheng, C.H. 1985. Finite-difference synthetic acoustic logs. *Geophysics, 50,* 1588-1609.

Stevens, J.L., and Day, S.M., 1986. Shear velocity logging in slow formations using the Stoneley wave. *Geophysics, 51*, 137–147.

Tadeu, A. J. B., 1992. Modelling and seismic imaging of buried structures. *PhD Thesis*, Massachusetts Institute of Technology, Cambridge, MA.

Tang, X.M., Cheng, C.H. and Toksöz, M.N., 1991. Dynamic permeability and borehole Stoneley waves: A simplified Biot-Rosenbaum model. *J. Acoust. Soc. Am., 90,* 1632–1646.

Thomsen, L., 1986. Weak elastic anisotropy. *Geophysics, 51,* 1954-1966.

Tsang, L. and Rader, D., 1979. Numerical evaluation of the transient acoustic waveform due to a point source in a fluid-filled borehole. *Geophysics, 44,* 1706-1720.

Tubman, K. M., Cheng, C. H. and Toksöz, M. N., 1984. Synthetic full-waveform acoustic logs in cased boreholes. *Geophysics, 49,* 1051-1059.

Virieux, J. 1984. SH-wave propagation in heterogeneous media: velocity-stress finite-difference method. *Geophysics, 49,* 1933-1957.

Virieux, J. 1986. P-SV wave propagation in heterogeneous media: velocity-stress finite-difference method. *Geophysics, 51,* 889-901.

White, J. E. and Tongtaow, C., 1981. Cylindrical waves in transversely isotropic media. *J. Acoust. Soc. Am. 70,* 1147-1155.

White, J. E. and Zechman, R. E., 1968. Computed response of an acoustic logging tool. *Geophysics, 33,* 302-310.

Williams, D.M., Zemanek, J., Angona, F.A., Dennis, C.L. and Caldwell, R.L., 1984. The long space acoustic logging tool. *Trans. SPWLA 25th Ann. Logging Symp.,* Paper T.

Winbow, G. A., 1988. A theoretical study of acoustic S-wave and P wave velocity logging with conventional and dipole sources in soft formations. *Geophysics, 53,* 1334-1342.

Winkler, K.W., Liu, H.L. and Johnson, D.L., 1989. Permeability and borehole Stoneley waves: comparison between experiment and theory. *Geophysics, 54,* 66–75.

Yoon, K.H. and McMechan, G.A., 1992. 3-D finite-difference modelling of elastic waves in borehole environments. *Geophysics, 57,* 793-804.

Zemanek, J., Angona, F.A., Williams, D.M. and Caldwell, R.L., 1984. Continuous acoustic shear wave logging. *Trans. SPWLA 25th Ann. Logging Symp.,*

Zhu, Z., Cheng, C.H. and Toksöz, M.N., 1993. Propagation of flexural waves in an azimuthally anisotropic borehole model. submitted to *Geophysics*